Challenge Journal of

STRUCTURAL MECHANICS

Vol.12 No.1 (2026)

auxetic buckling load building codes
compressive strength dynamic analysis
earthquake finite element method
girder bridge Jaya algorithm metaheuristic
algorithms modal analysis optimization
prestresing pushover analysis reinforced
concrete seismic design shallow foundations
smart concrete stability static analysis
steel structures structural dynamics
temperature effects thick plate wind

TULPAR
ACADEMIC PUBLISHING

ISSN 2149-8024

Challenge Journal of STRUCTURAL MECHANICS

E-mail: *cjsmec@challengejournal.com*

Web page: *cjsmec.challengejournal.com*

Tulpar Academic Publishing
www.tulparpublishing.com

Challenge Journal of STRUCTURAL MECHANICS

CONTENTS

Research Articles

TULPAR ACADEMIC PUBLISHING

Challenge Journal of STRUCTURAL MECHANICS

Research Article

Seismic hazard and risk analyses of historical masonry structures in Kocaeli, Türkiye

Yusuf Kahraman [a], Ferit Cakir [a,*], Abdullah Can Zulfikar [b], Methiye Gundogdu Gok [c]

[a] *Department of Civil Engineering, Gebze Technical University, 41700 Kocaeli, Türkiye*
[b] *Disaster Management Institute, İstanbul Technical University, 34000 İstanbul, Türkiye*
[c] *Department of Earthquake Engineering, İstanbul Technical University, 34000 İstanbul, Türkiye*

ABSTRACT

Protection of masonry structures is among the most important building groups around the world. Generally constructed of heavy materials such as stone and brick, these structures are highly seismically vulnerable. In large earthquakes, masonry structures that have not received adequate engineering services are usually heavily damaged or destroyed. To prevent damage to these structures, seismic hazard and risk analyses must first be conducted correctly. This study investigates the seismic hazards and risk distributions of historical masonry structures in Kocaeli, Türkiye. As a preliminary step, information and document collection studies on historical masonry structures were conducted in Kocaeli, Türkiye. Then, a detailed building inventory data set was prepared. Following that, a probabilistic seismic hazard assessment for the investigation area was conducted considering the different attenuation relationships. In the seismic hazard analyses, the hazard maps, hazard curves and response spectra were prepared based on the inventory data set at select reference points. After that, the seismic risk analyses were conducted to determine the structure distribution based on damage levels for the structures in the data set considering different fragility curves. Accordingly, historical masonry structures in Kocaeli province close to the North Anatolian Fault (NAF) Line have high hazard curves and spectrum values, whereas structures on the Black Sea coast have low values. According to the hazard maps obtained as a result of the analyses, Kartepe, Darica, Gölcük, and Başiskele districts have a high estimated hazard distribution, while Kandira has a lower estimated hazard distribution. Further, when the risk assessment is carried out by looking at the distribution of building groups based on damage levels, it was determined that towers, aqueducts, residential structures, and dome structures are the highest priority risk structures, respectively.

ARTICLE INFO

Article history:
Received – April 8, 2025
Revision requested – May 12, 2025
Revision received – May 31, 2025
Accepted – June 10, 2025

Keywords:
Seismic hazard and risk analysis
Immovable cultural heritage
Attenuation relations
Fragility curves
Hazard maps and spectra
Damage distributions

Citation: Kahraman Y, Cakir F, Zulfikar AC, Gundogdu Gok M (2026). Seismic hazard and risk analyses of historical masonry structures in Kocaeli, Türkiye. *Challenge Journal of Structural Mechanics*, 12(1), 1–21.

1. Introduction

Historical masonry buildings are universal values that carry the traces of past civilizations to the present, thanks to their architecture, construction techniques, construction dates, types of use and building materials. When the destructive earthquakes occurring around the world have been examined, it is understood that historical masonry structures have been damaged to a great extent by the earthquakes (VGM 2017.) However their performance under horizontal dynamic loads such as earthquakes is often poor, which makes reliable seismic performance evaluation and strengthening needs critical (Akın and Alagöz 2024). Accordingly, the preservation of cultural heritage has become increasingly important in the face of conflicts and natural disasters that threaten

* *Corresponding author*. E-mail address: cakirf@gtu.edu.tr (F. Cakir)
ISSN: 2149-8024 / DOI: https://doi.org/10.20528/cjsmec.2026.01.001

historical sites worldwide (Arzomand et al. 2024). In addition, the structural performance of materials used in historical buildings may deteriorate over time due to natural events or human induced interventions, which can further increase their vulnerability under seismic actions (Zardari et al. 2024).

In order to protect historical masonry structures from earthquake hazards and ensure their safe transfer to future generations, it is important to understand their structural behavior and conduct hazard and risk analyses. It is very important to predict earthquake losses, to take the necessary precautions before the earthquake and to determine the seismic risk levels of masonry structures in order to minimize earthquake damage. Thus, hazard and risk assessment studies estimate damages and identify possible risks before an earthquake occurs. Hazard analysis today is based on both deterministic and probabilistic methods. Risk analysis studies can provide damage and loss estimations in addition to hazard curves and hazard maps. Earthquake risk management includes preventing the effects of earthquakes and reducing their damages, realizing the necessary planning and coordination to be prepared for earthquakes, intervention and recovery activities after the earthquake (Oktay et al. 2020). When the studies in the literature are examined, there are risk analyses based on different building groups, especially historical buildings and masonry structures, together with regional or more comprehensive hazard analyses carried out throughout the world. For example, Biglari et al. (2022) conducted a numerical evaluation of the seismic vulnerability of historical buildings in Kermanshah city, which is known as the center of prehistoric and historical cultures in the Zagros seismotectonic region of Iran, using numerical modeling. The study has indicated the seismic vulnerability of the examined mosques and the need to provide parameters such as slab type and aggregate configuration in order to evaluate Iranian historical buildings more effectively. Fazzi et al. (2021) proposed a methodology for seismic vulnerability assessment of a series of historic churches characterized by a specific building typology. This methodology allows the coordination and interprets seemingly distant data on the seismic behavior of historic buildings, obtained by different research scales and analysis tools. Within the scope of the study, a multi-disciplinary evaluation covering historical, environmental, geometric, technological and mechanical issues was conducted for a number of basilica churches affected by the 2009 L'Aquila earthquake in the central region of Italy to reveal the weaknesses related to the associated building typology. Zulfikar et al. (2021) conducted an earthquake hazard analysis for a typical power generation facility in the Marmara region, Türkiye. With the study, loss curves have been obtained in order to determine the risks that the relevant facility will be exposed to as a result of a possible earthquake ground motion that may occur in the Marmara region and to develop the activities that can be done to reduce these risks.

Pirchio et al. (2021) emphasized the importance of cultural heritage, they proposed a method to determine the seismic risk assessment for a historic masonry church in a fast, measurable and comprehensive approach. Within the scope of the study, 72 existing reinforced masonry medieval churches across Italy were examined in the field. For each risk component (hazard, vulnerability, exposure and consequence), 13 different indices were developed. Ademović et al. (2021) prepared old-generation probabilistic seismic hazard maps for Bosnia and Herzegovina. In the study, in which areal and linear faults were taken into account, an earthquake catalog was prepared with the filtering of fore and aftershocks and two seismotectonic models were created. The greatest ground acceleration parameter was taken as a basis while creating the hazard maps. Hoveidae et al. (2021) investigated the earthquake damage of the historical Arge-Tabriz structure using ground motion records simulated specific to the region where the structure is located. Within the scope of the study, it was aimed to estimate the damage level of the Arge-Tabriz monument against a possible earthquake. In order to evaluate the seismic damage of the Arge-Tabriz structure, possible earthquake scenarios of different magnitudes were simulated. Gundogdu Gok (2020) conducted a probabilistic earthquake hazard analysis based on the Monte Carlo method by using the 1999 Kocaeli Earthquake. In the study, the open-source OpenQuake program was used for analysis and the earthquake hazard of the Eastern Marmara Region was determined. Govsulu (2020) conducted a seismic hazard analysis for the region located in a circle with a radius of 150 km, centered on the Urla-Çeşme-Karaburun districts of İzmir province, Türkiye. Different new generation attenuation relationships were used in the study, in which the CRISIS 2015 software was used within the scope of the analysis. Within the scope of the analysis, seismic hazard maps and acceleration spectrum curves were obtained. Hofer et al. (2018) carried out a damage survey on a large church stock in Central Italy, which was affected by the Amatrice earthquake on August 24, 2016. Within the scope of the study, damage assessments were made for 196 churches in the relevant region. In this study, which aims to determine the damage mechanisms, empirical fragility functions were derived for certain structural types. Lourenço et al. (2013) developed a method that provides lower bound formulas for different simplified geometric indices and simplifies the seismic evaluation of large-span masonry structures applied to a data set of 44 monuments in Italy, Portugal and Spain. Cuadra et al. (2008) performed a seismic risk analysis of the cultural structures in Machu Picchu. In the study, the dynamic properties of Inca stone structures were investigated, and this approach was proposed to assess seismic vulnerability.

When the studies in the literature are examined, it is seen that seismic hazard and risk studies related to structural groups such as reinforced concrete and steel are mostly carried out. On the other hand, studies in the literature for structures that are more difficult to evaluate according to inventory information, construction years, construction techniques and usage purposes compared to new-generation building groups such as masonry structures are in the minority. However, studies have shown that the fragility curves suitable for these structures are also insufficient, and it is thought that this is an important issue that needs to be developed in terms of the correct evaluation of these building groups. In this study, masonry structures registered as buildings within

the scope of immovable cultural assets were evaluated. It is thought that the study will make an important contribution to the literature, as the study area, Kocaeli, is located on the Alpine-Himalayan fold belt, one of the most important active earthquake zones in the world, and hosts many historically qualified structures.

2. Building Inventory Data Set

As stated earlier, there are two basic approaches for performing seismic hazard analyzes: deterministic and probabilistic. In this study, a probabilistic approach was used within the scope of hazard analysis. Compared to the deterministic approach, the probabilistic approach is preferred, considering that it can provide more effective results because it assumes many scenarios, considers all magnitudes associated with all seismic sources and considers all possible distances between the source and the site. Within the scope of the analysis, firstly, the investigation area (Fig. 1) was divided into grids in the QGIS program to determine the study area, and the locations of the structures in the region were also added to the grids (Fig. 2).

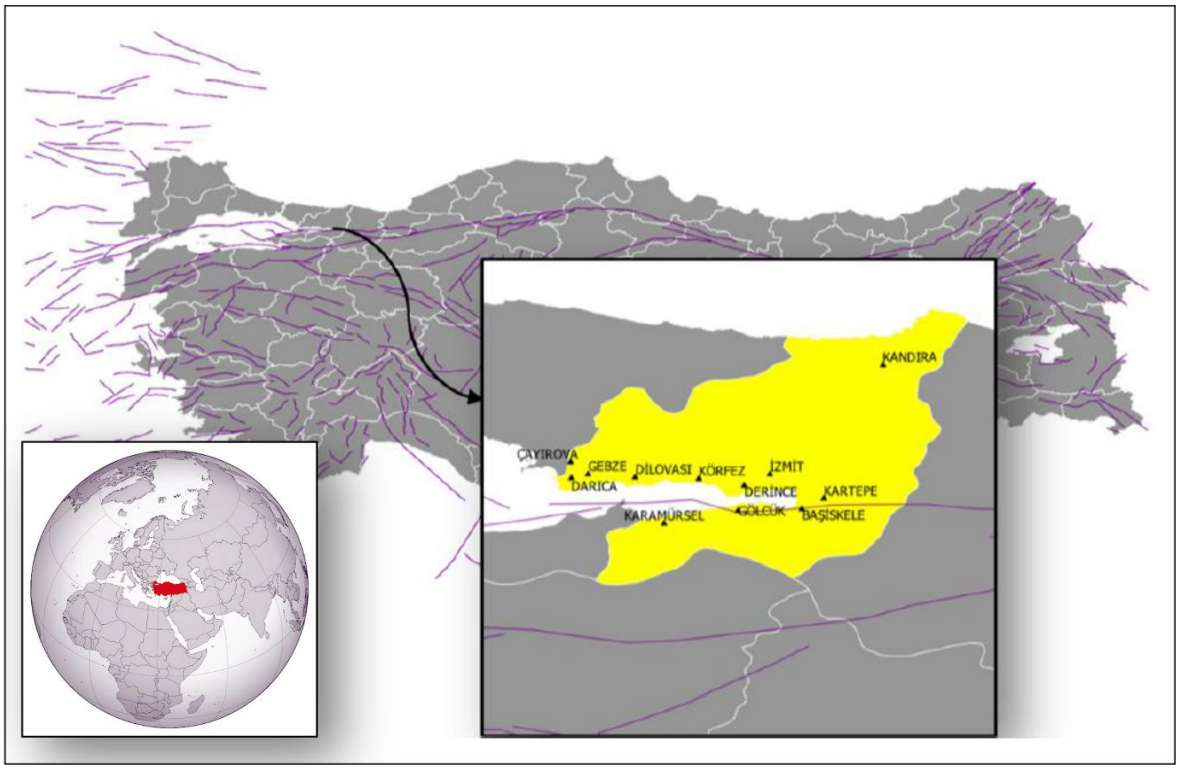

Fig. 1. The Investigation area and fault sources from the SHARE Project.

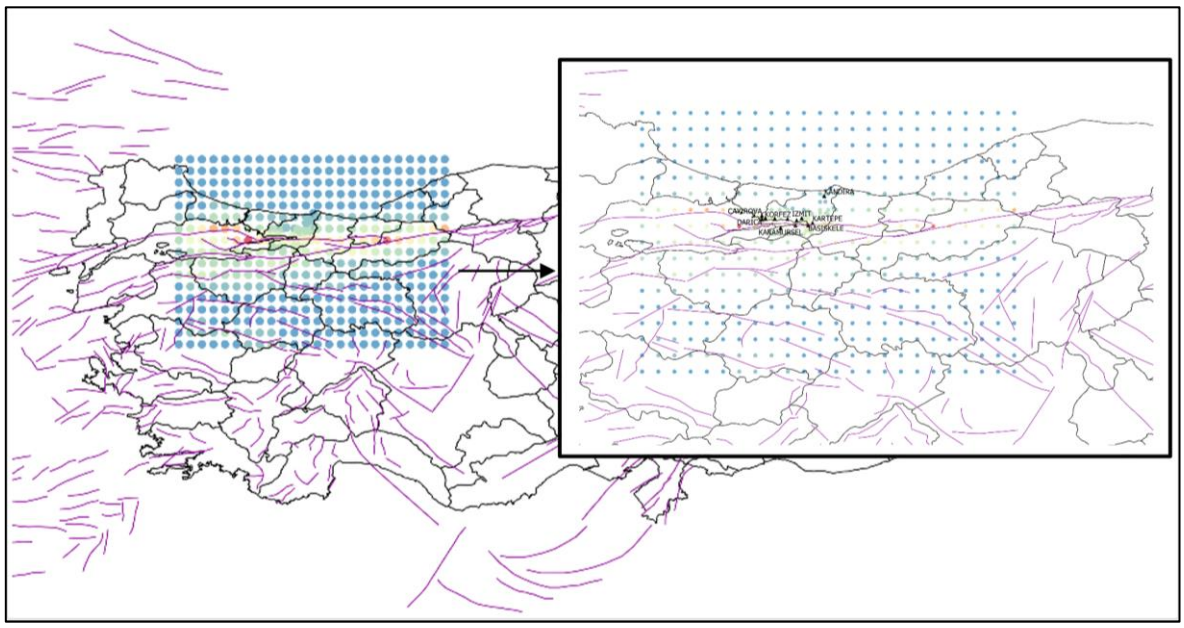

Fig. 2. The investigation area divided into grids.

Within the scope of the study, firstly, information and document collection studies were carried out on the masonry structures in Kocaeli province and detailed building inventory data was prepared considering each district of Kocaeli. In the study, only registered historical masonry structures were taken into account and Kocaeli Cultural Inventory Book Aksoy (2011) was used as a source for the identification of the historical masonry structures. This inventory data contains parameters such as stories, construction materials and quality of construction as well as structural types and occupancy types. An example of the inventory data was given in Table 1.

Table 1. Detailed building inventory data form.

IDENTIFICATION

Property Name (If any): İzmit Clock Tower

Address or Street Location: Kemalpaşa District of İzmit

City: Kocaeli

District: İzmit

Owner: Kocaeli Metropolitan Municipality

Address:

Original use: Clock Tower

Current use: Clock Tower

Architect/Builder (if known): Architect Vedat

Date of construction (if known): 1901

DESCRIPTION

Materials – please check those materials that are visible

Exterior Walls:	☐ wood	☐ wood	☐ vertical boards	☐ plywood
	☒ clipboard	☐ shingle	☐ poured	☐ concrete
	☐ stone	☐ brick	☐ concrete	☐ block
Roof:	☐ shingle	☐ rool	☐ wood	☒ metal ☐ slate
Foundation:	☒ stone	☐ brick	☐ poured concrete	☐ concrete block

Other materials and their location: There are marble columns on the sides of the 1st floor

Alterations, if known: **Date**:

Condition: ☐ excellent ☒ good ☐ fair ☐ deteriorated

PHOTOS

MAPS

In addition to the inventory classification, a typological categorization was introduced based on architectural function, material usage, and geometric features such as arches and domes (Fig. 3). This classification was supported by expert evaluations from structural engineers experienced in historical architecture. Reference was also made to typologies defined in international seismic risk literature to ensure consistency with widely adopted structural taxonomies. Therefore, first of all, registered historical masonry buildings were separated according to districts and it was determined which buildings were located in which district (Figs. 4 and 5). Then, buildings were classified into eight structural classes according to their structural types and intended uses after determining the registered structures (Table 2).

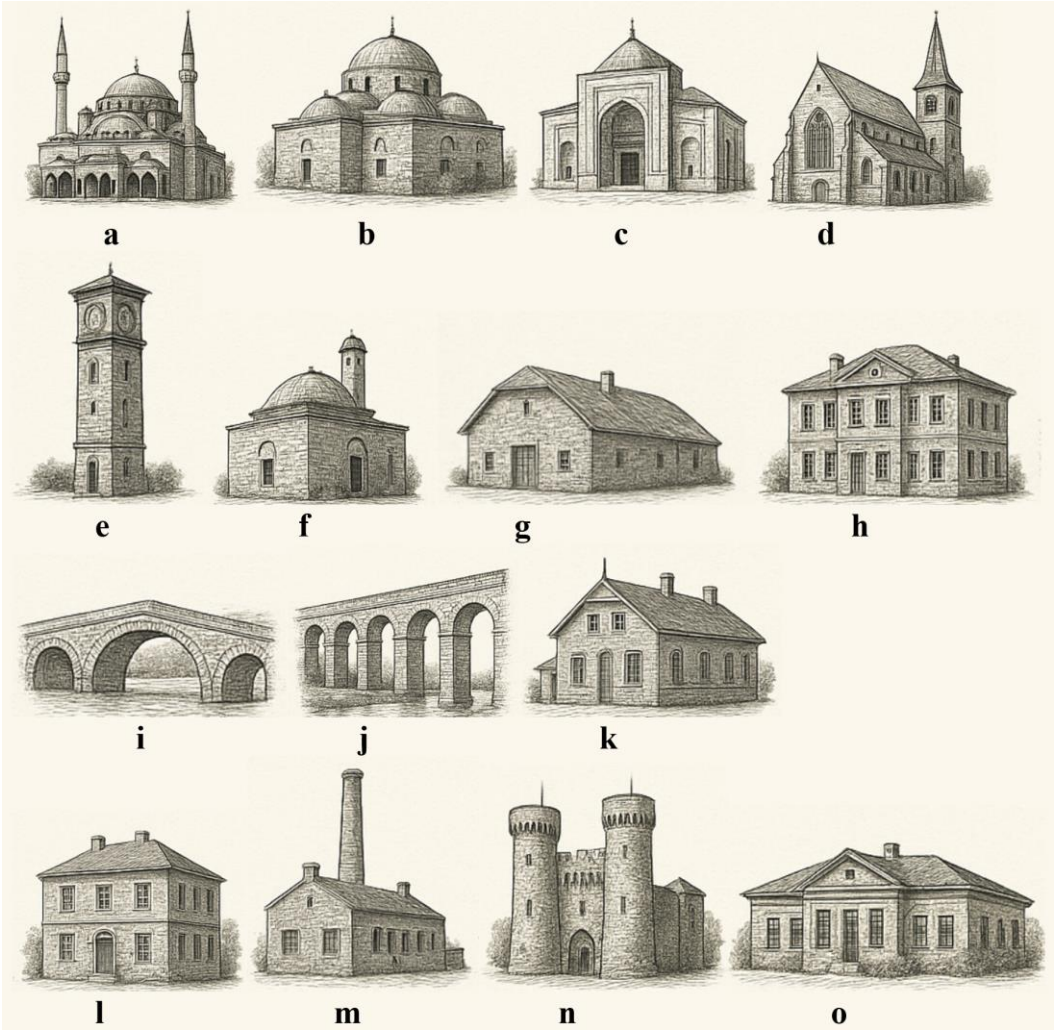

Fig. 3. The classification of the masonry structures: (a) Mosques; (b) Masjids; (c) Madrasahs; (d) Churches; (e) Clock towers; (f) Baths; (g) Barns; (h) Administrative structures; (i) Bridges; (j) Aqueducts; (k) Train stations; (l) Schools; (m) Factories; (n) Castles; (o) Townhouse (AI-generated).

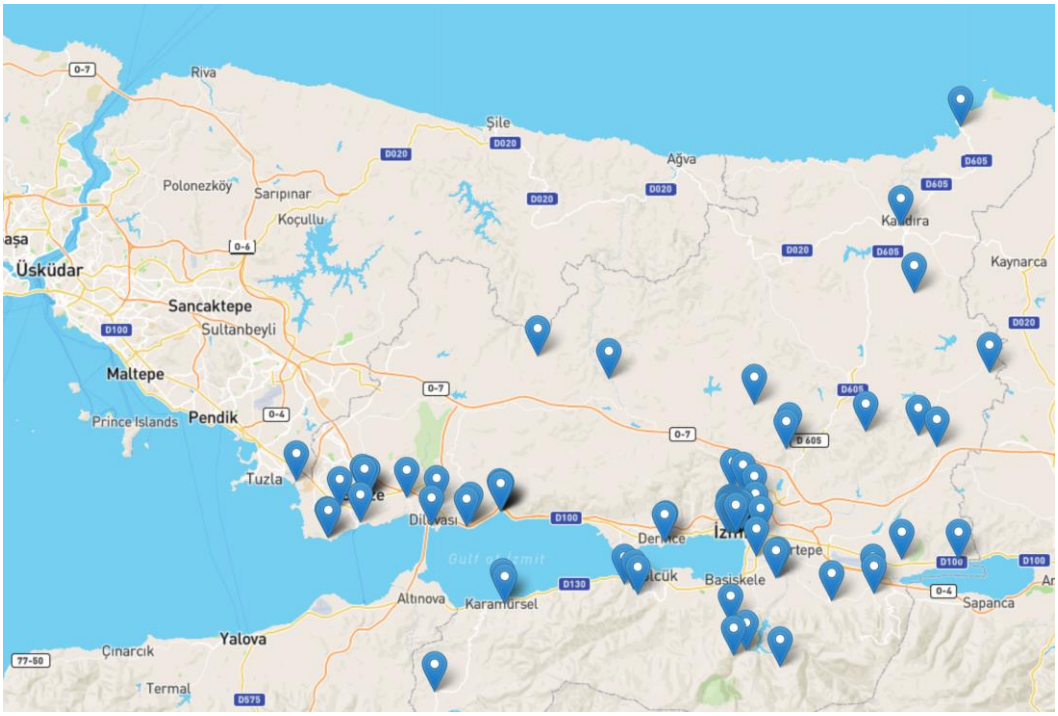

Fig. 4. The historical masonry structures in the investigation area.

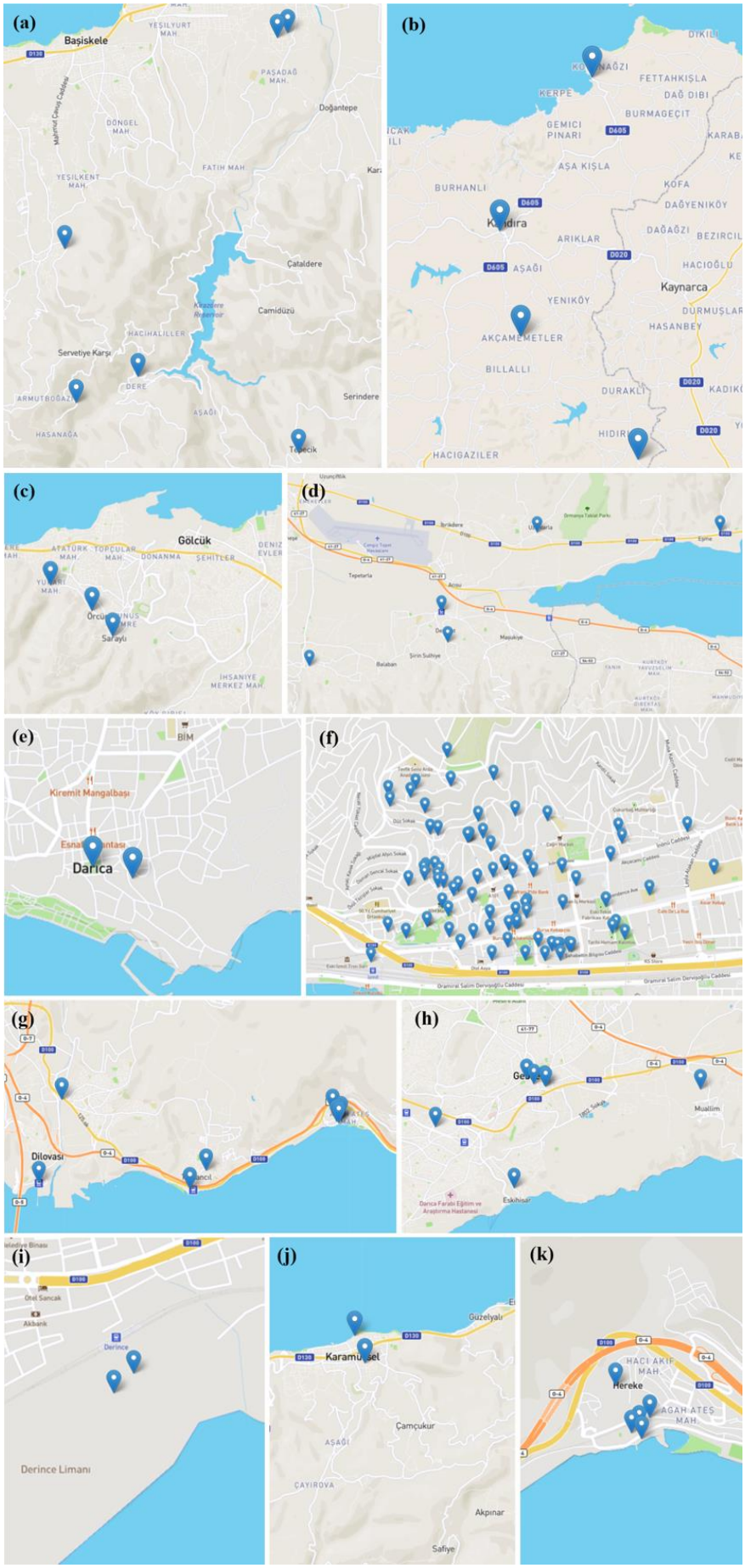

Fig. 5. Distribution of the historical masonry structures by districts; (a) Başiskele; (b) Kandıra; (c) Gölcük; (d) Kartepe; (e) Darıca; (f) İzmit; (g) Dilovası; (h) Gebze; (i) Derince; (j) Karamürsel; (k) Körfez.

Table 2. The distribution of the buildings.

		İzmit	Kartepe	Başiskele	Gölcük	Karamürsel	Derince	Körfez	Dilovası	Gebze	Darıca	Kandıra	Total
Religious Buildings	Mosques	12	3	2	2	1	–	1	1	3	–	4	29
	Masjids	5	–	–	–	–	–	–	–	–	–	–	5
	Madrasahs	–	–	–	–	–	–	–	–	–	–	–	0
	Churches	2	–	–	–	–	–	–	–	–	1	–	3
Social and Cultural Structures	Clock Towers	1	–	–	–	–	–	–	–	–	–	–	1
	Baths	6	–	–	1	–	–	–	–	2	–	–	9
	Barns	–	–	1	–	–	–	–	–	–	–	–	1
	Administrative Structures	–	–	–	–	1	–	–	–	–	–	–	1
Transportation Structures	Bridges	1	–	2	–	1	–	1	1	1	–	–	7
	Aqueducts	5	–	–	–	–	–	–	–	–	–	–	5
	Train Stations	1	1	–	–	–	1	1	2	1	–	–	7
Educational Structures	Schools	6	–	1	–	–	–	–	–	–	–	–	7
Industrial Structures	Factories	4	–	1	–	–	1	2	–	2	–	–	10
Defense Structures	Castles	2	–	–	–	–	–	–	–	–	1	–	3
Mansions	Townhouse	9	1	–	–	–	–	1	–	–	–	–	11
Other Residences		39	–	–	–	–	–	–	–	–	–	–	39
	Total	93	5	7	3	3	2	6	4	9	2	4	138

3. Seismic Hazard Analysis

The time, location, magnitude, and other characteristics of future earthquakes in seismically active regions cannot be predicted in advance. One of the most challenging aspects of earthquake engineering is to estimate the maximum effects of earthquakes that may occur in a given time period on construction sites, especially for parameters related to ground motion. As ground motion parameters, acceleration, velocity, displacement, and spectral acceleration, which reflect the characteristics of ground vibrations in the studied region, are expressed. A probabilistic and statistical approach is required to determine the parameters to be considered in designing earthquake-resistant structures due to the variability and uncertainty associated with earthquakes in terms of time, location, and intensity (Yücemen 2011). A seismic hazard analysis determines the ground shaking hazard in a particular area numerically. There are two types of seismic hazards analysis: the deterministic method, where the assumption of a special scenario earthquake is assumed, and the probabilistic method, which takes into account the uncertainties associated with earthquake magnitude, location, and time (Kramer 1996).

During earthquake-resistant building design, it is important to simulate the ground motions caused by the decisive earthquake so that the design can be adapted to reality as much as possible. Because earthquake motions based on the design are defined by ground motion characteristics, it is necessary to develop methods for calculating ground motion parameters. Attenuation relations are used to calculate ground motion parameters by expressing them in terms of the most strongly affecting magnitudes. Based on conditions such as magnitude, fault mechanism, propagation direction, and local ground effects, attenuation relationships predict strong ground motion parameters.

In the developed attenuation relations, spectral accelerations are defined depending on the moment magnitude of the earthquake, distance, earthquake mechanism and local soil conditions. Care should be taken to use the same earthquake magnitude scale in attenuation relationships, in compiling the magnitude-frequency data, and in determining the maximum magnitude. The distance parameter used for attenuation relations can be expressed as the distance from the focal center, the epicenter, the energy discharge center, the fault surface and the fault extension. Attenuation relations usually describe ground motion parameters as a function of magnitude, distance, and in some cases, other variables. The reduction relationship is expressed by the function $Y=f(M, R, Pi)$. In the function, Y is the desired ground motion parameter, M is the magnitude of the earthquake, R is the distance between the source and the project site, and Pi is used to characterize the earthquake source, wave propagation or local ground conditions. Attenuation relationships are developed by regression analysis methods using the data of recorded strong ground motions. This data set changes as more ground motions occur over time. The attenuation relationships in the literature are generally updated every 3 to 5 years or after major earthquakes occur in locations with a good measuring grid (Kramer 1996).

Seismic hazard analyses were conducted using an open-source program, OpenQuake. A total of eleven attenuation relations, which were suitable for the investigation area, were considered along with seismic characteristics and ground conditions (Table 3). After that, the seismic hazard analysis of the investigation area was conducted based on each attenuation relation. In comparison with the TEC (2018), Campbell and Bozorgnia (2014) was determined to have the most favorable attenuation relation for the investigation area. The results obtained for the three critical reference locations (İzmit, Kartepe, Kandıra) against the earthquake ground motion level of DD-2 (10% probability of exceeding in 50 years, recurrence period of 475 years) are listed below (Figs. 6-8).

After the determination of the most appropriate attenuation relationship, seismic hazard analyzes were carried out considering the 50 years in the analysis. The analysis was carried out assuming bedrock ground ($(Vs)_{30}$ = 760 m/sec). Within the scope of the seismic hazard analyses, hazard curves corresponding to PGA (with/without $(Vs)_{30}$) and the spectral periods for 11 selected reference locations (İzmit, Kartepe, Başiskele, Gölcük, Karamürsel, Derince, Körfez, Dilovası, Gebze, Darıca, Kandıra) were prepared (Figs. 9, 10, 13, and 15). The PGA, $Sa(0.2)$ and $Sa(1.0)$ spectral periods corresponding to DD-2 earthquake ground motion levels were prepared as colored maps (Figs. 11, 12, 14, and 16). In addition, the response spectrums obtained for DD-2 earthquake ground motion levels at the reference locations were prepared in the seismic hazard analyses for reference points (Figs. 17–27).

Table 3. The attenuation relationships used in the study.

Attenuation Relationships in the Study	OpenQuake Hazard Library Name
AS08: Abrahamson and Silva (2008)	AbrahamsonSilva2008
BA08: Boore and Atkinson (2008)	BooreAtkinson2008
CB08: Campbell and Bozorgnia (2008)	CampbellBozorgnia2008
CY08: Chiou and Youngs (2008)	ChiouYoungs2008
ASK14: Abrahamson et al. (2014)	AbrahamsonEtAl2014
BSSA14: Boore et al. (2014)	BooreEtAl2014
CB14: Campbell and Bozorgnia (2014)	CampbellBozorgnia2014
CY14: Chiou and Youngs (2014)	ChiouYoungs2014
ASB14: Akkar et al. (2014)	AkkarEtAlRepi2014
AC10: Akkar and Cagnan (2010)	AkkarCagnan2010
Z06: Zhao et al. (2006)	ZhaoEtAl2006Asc

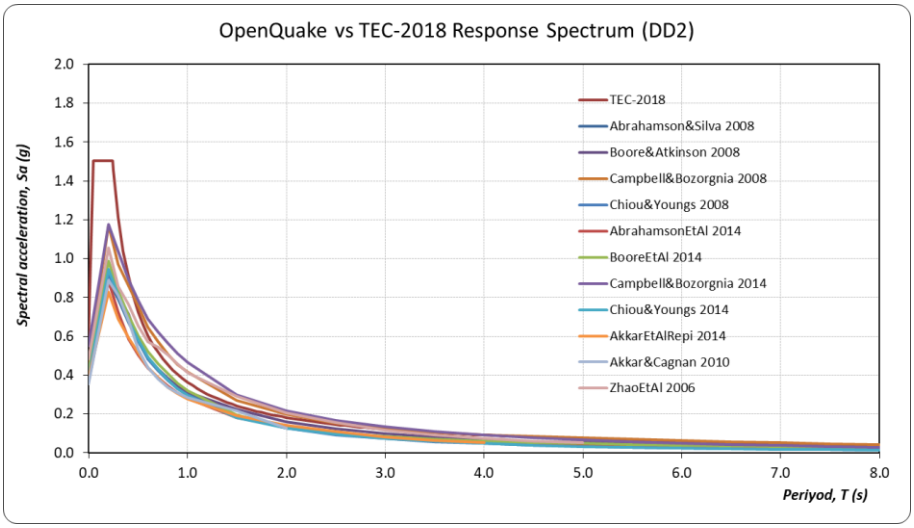

Fig. 6. Comparison of the results obtained from OpenQuake with the TEC-2018 spectrum using the relevant attenuation relations for the DD-2 earthquake ground motion level at the İzmit district.

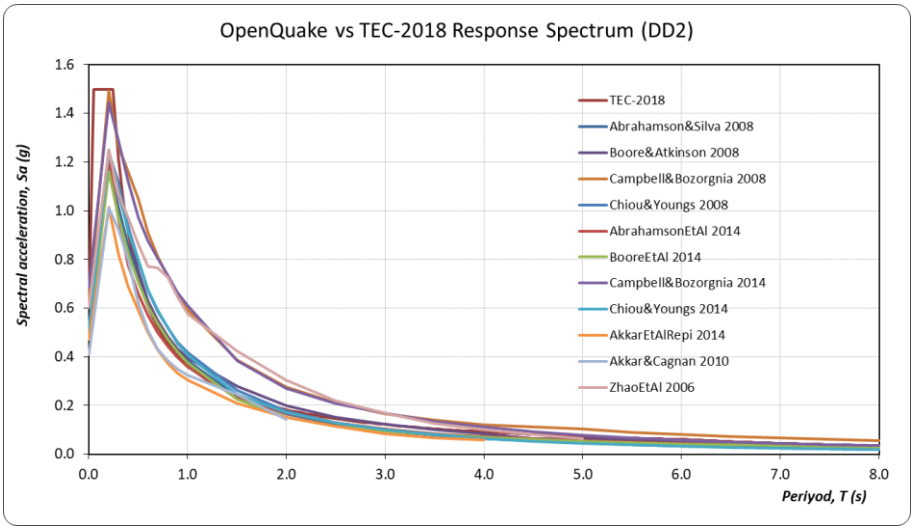

Fig. 7. Comparison of the results obtained from OpenQuake with the TEC-2018 spectrum using the relevant attenuation relations for the DD-2 earthquake ground motion level at the Kartepe district.

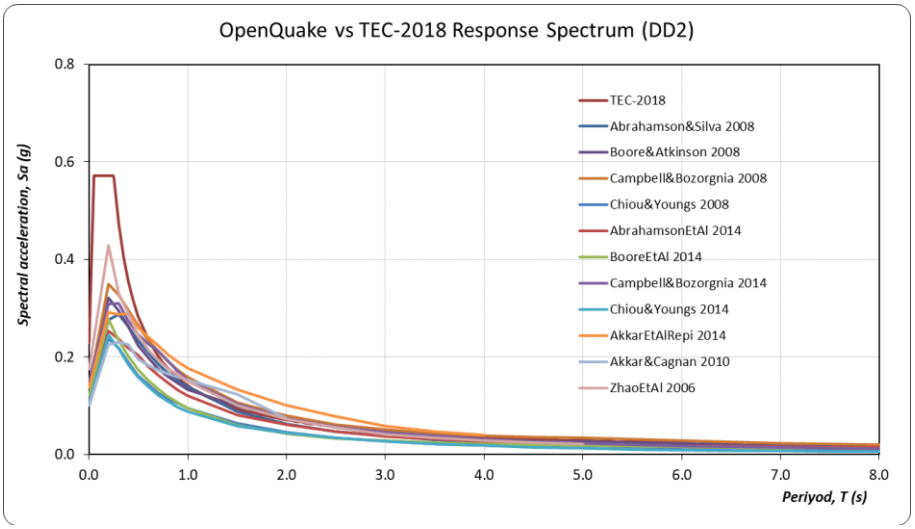

Fig. 8. Comparison of the results obtained from OpenQuake with the TEC-2018 spectrum using the relevant attenuation relations for the DD-2 earthquake ground motion level at the Kandıra district.

4. Seismic Risk Analyses

If the losses that may occur as a result of earthquakes can be reliably estimated, more rational decisions can be made for disaster preparedness, response and mitigation, and efficient use of the country's resources in line with development goals can be achieved. Seismic risk assessment studies provide important information about what needs to be done before and after an earthquake. From raising public awareness to conducting exercises, planners use the estimation of losses that may occur from earthquakes to prepare for disasters. Contributes to the development of national building design and reinforcement regulations, earthquake insurance and reinsurance models, cost-benefit analyses, and risk reduction plans (Çetin and Erberik 2017).

Using earthquake hazard and data related to the region together, earthquake risk analysis evaluates probabilities considering the earthquake risk, earthquake hazard, land use, demographic structure and economic structure. The outputs of the earthquake risk analysis include the estimations of the material losses that will occur in case of damage to the structures such as roads, industrial facilities, bridges, and dams, especially the loss of life caused by the earthquake (Tutar et al. 2017).

During the seismic risk analyses, the fragility curves used for the examined building group are important in terms of performing the analysis correctly. Fragility functions (curves) expressed as analytical functions are widely used to evaluate seismic risk or to make loss estimations. The fragility functions define the exceedance probabilities for different damage limit situations (Destroyed-Heavy-Medium-Low-Damaged) at a given ground shaking level (Çetin and Erberik 2017). The fragility curves used for loss and damage estimations in seismic risk assessments are created for building types with similar characteristics in a particular country or region. Due to the difficulties in creating fragility curves that take into account regional characteristics, existing fragility curves, which are mostly obtained as a result of international studies, are used to make damage and loss estimations (Çetin and Erberik 2017).

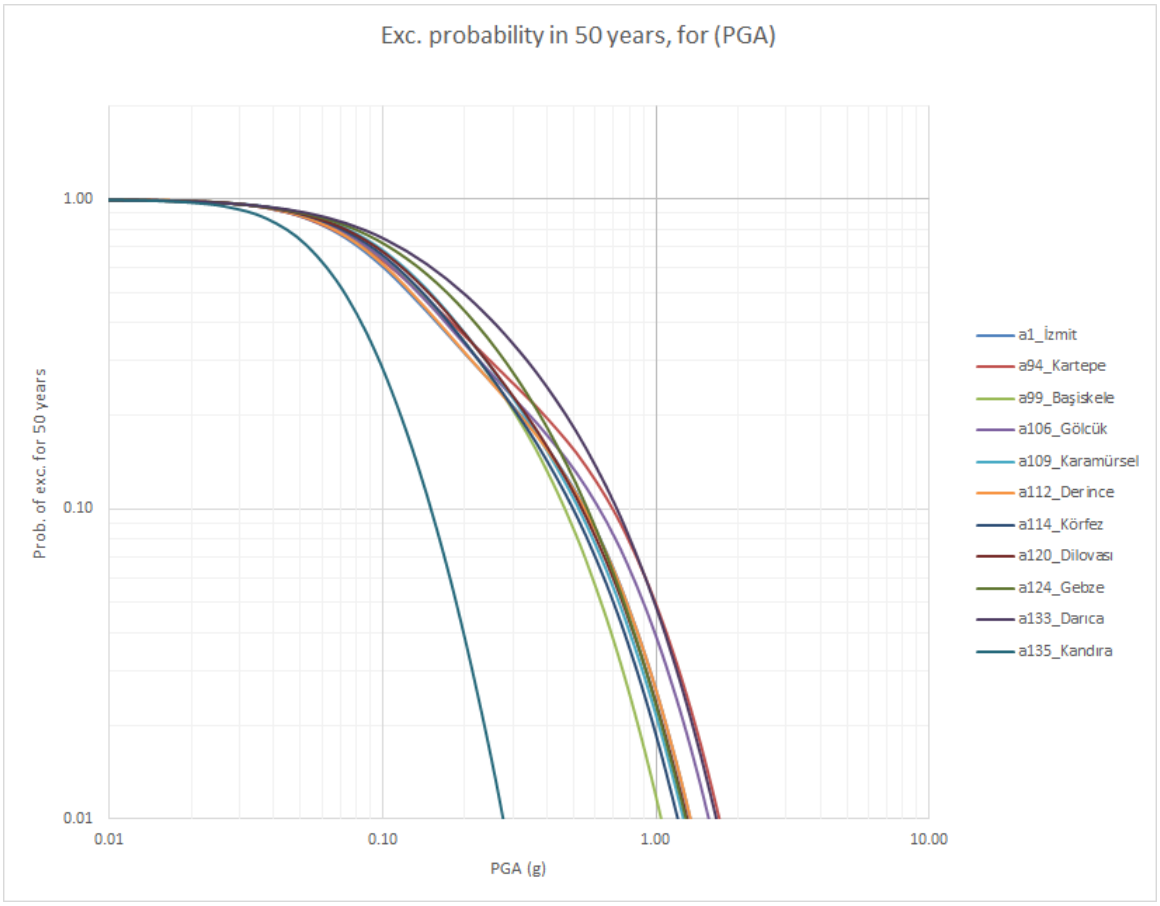

Fig. 9. Hazard curves obtained for PGA(g) at selected locations with $(Vs)_{30}$.

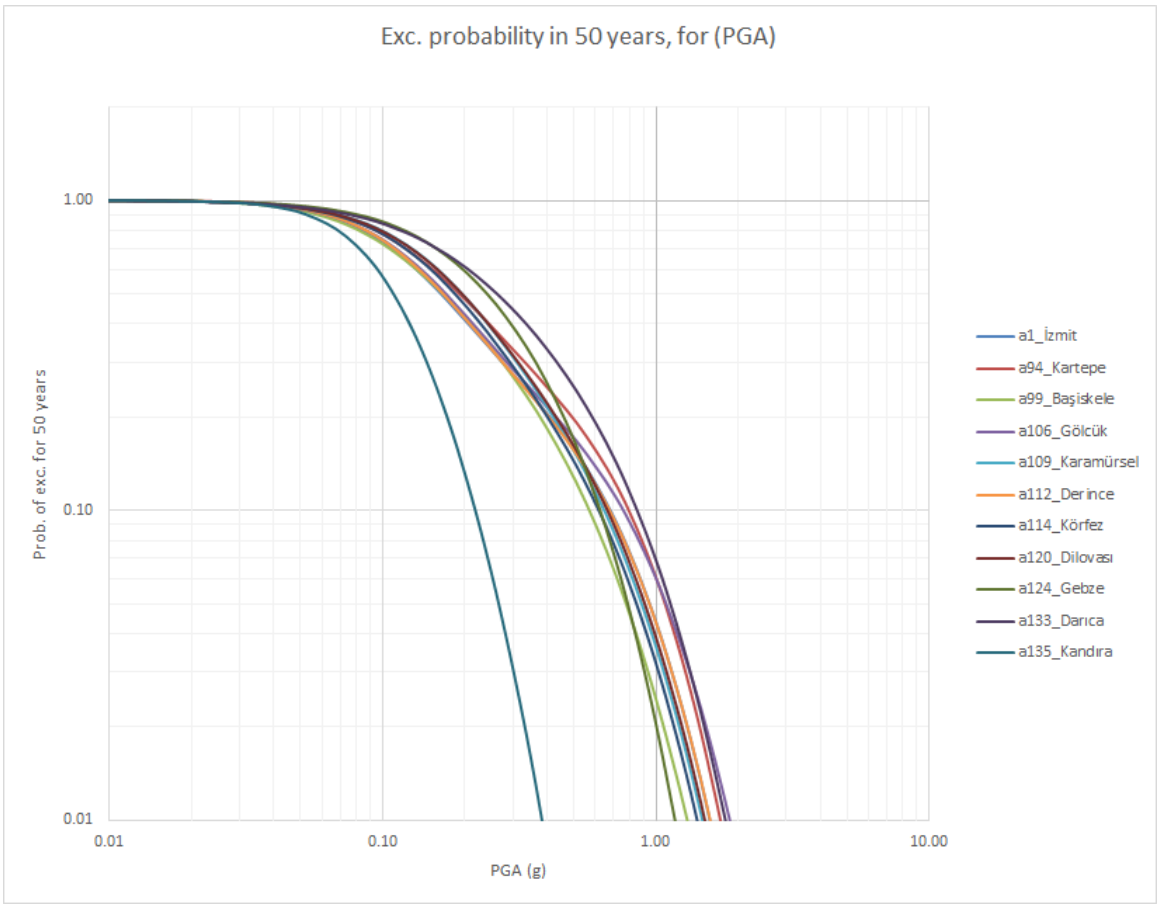

Fig. 10. Hazard curves obtained for PGA(g) at selected locations without with $(Vs)_{30}$.

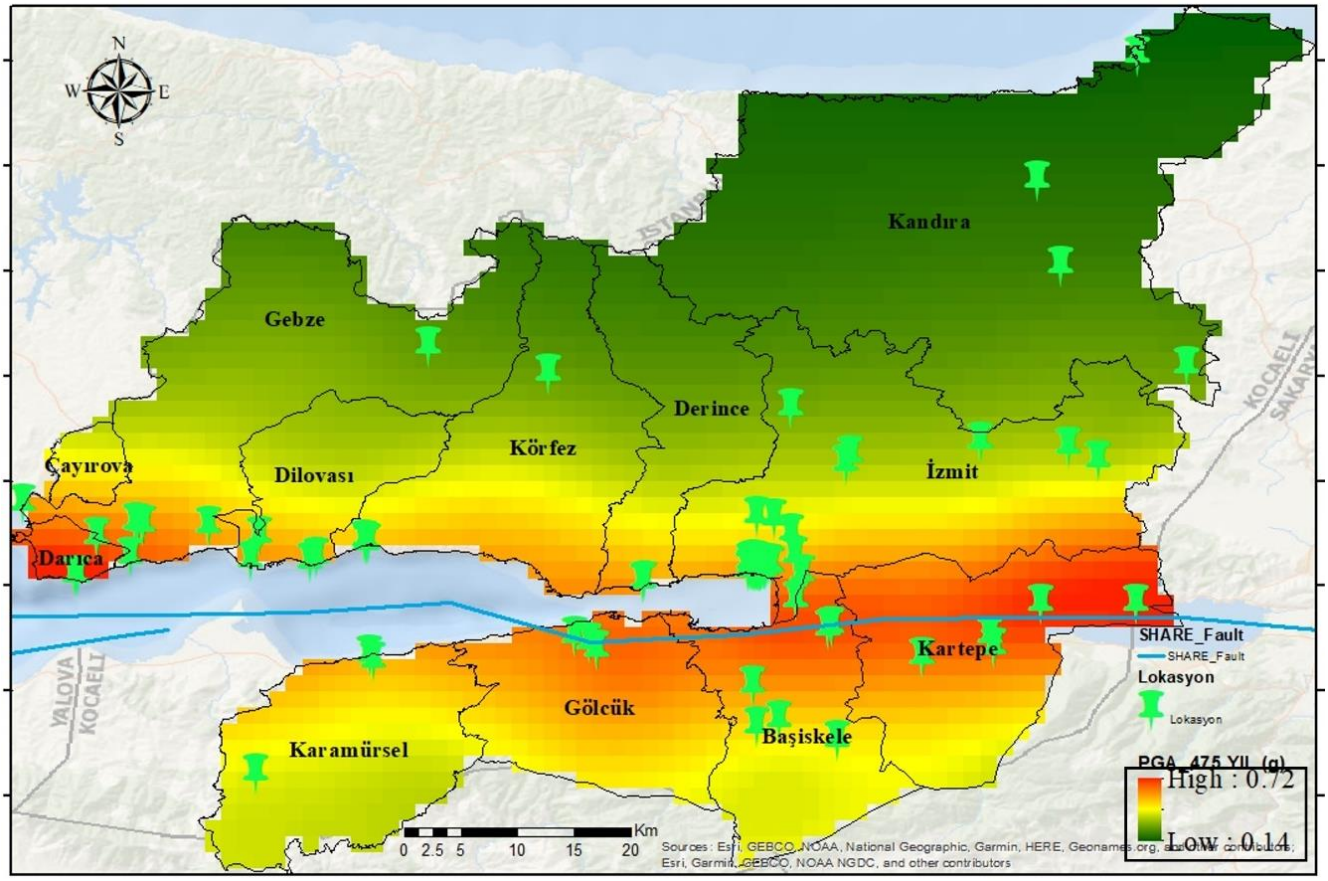

Fig. 11. PGA(g) level distribution for DD-2 earthquake ground motion level without $(Vs)_{30}$.

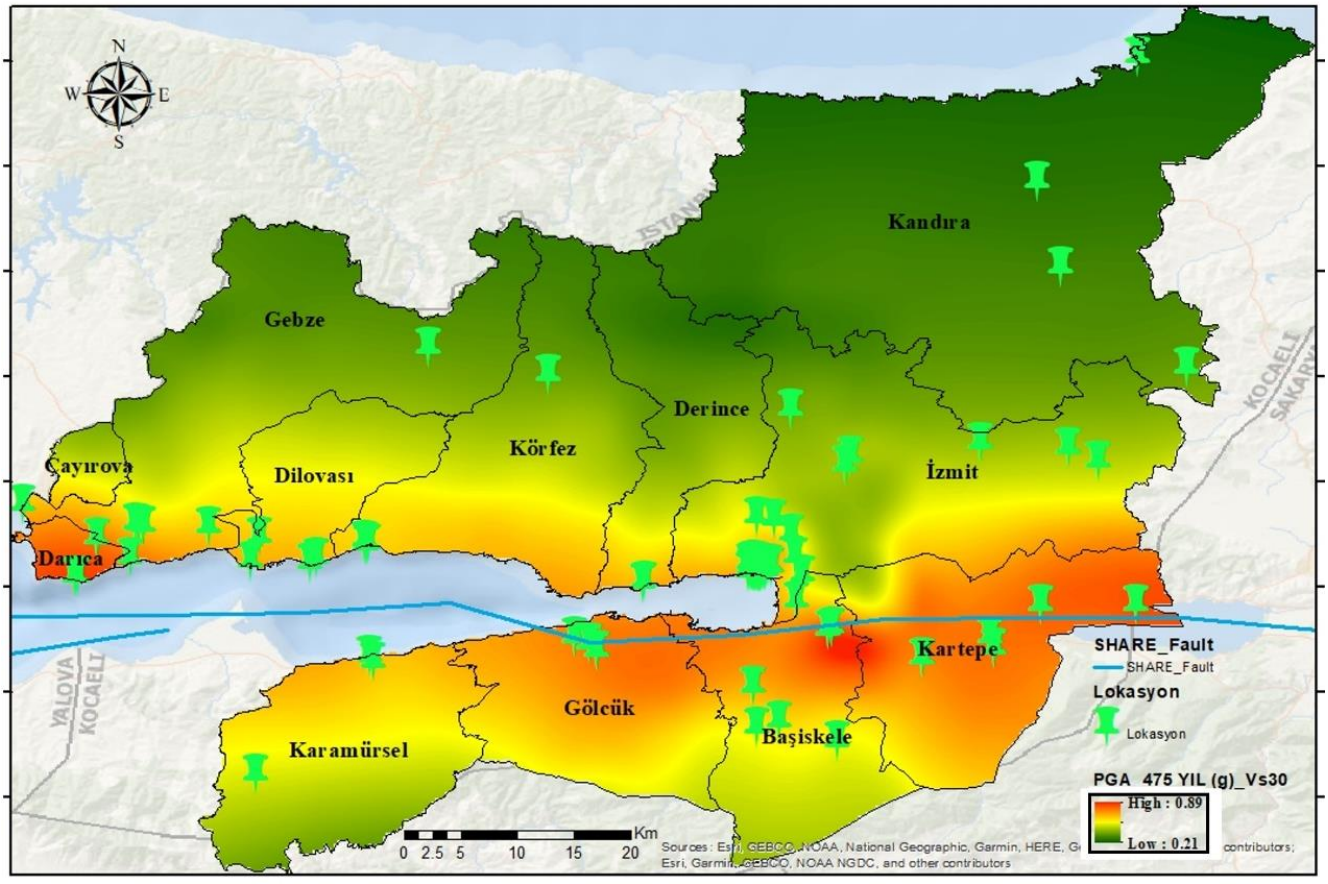

Fig. 12. PGA(g) level distribution for DD-2 earthquake ground motion level with $(Vs)_{30}$.

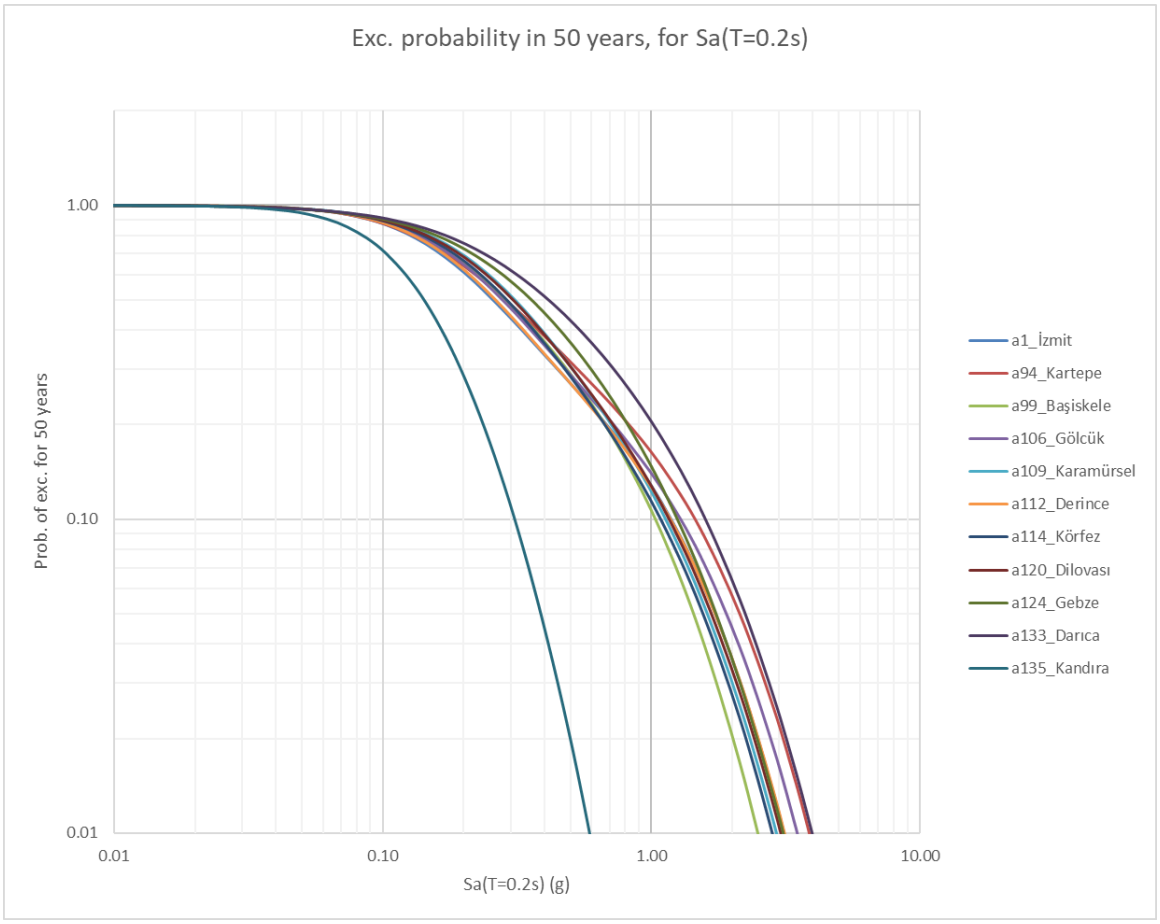

Fig. 13. Hazard curves obtained for $Sa(0.2)(g)$ at selected locations with $(Vs)_{30}$.

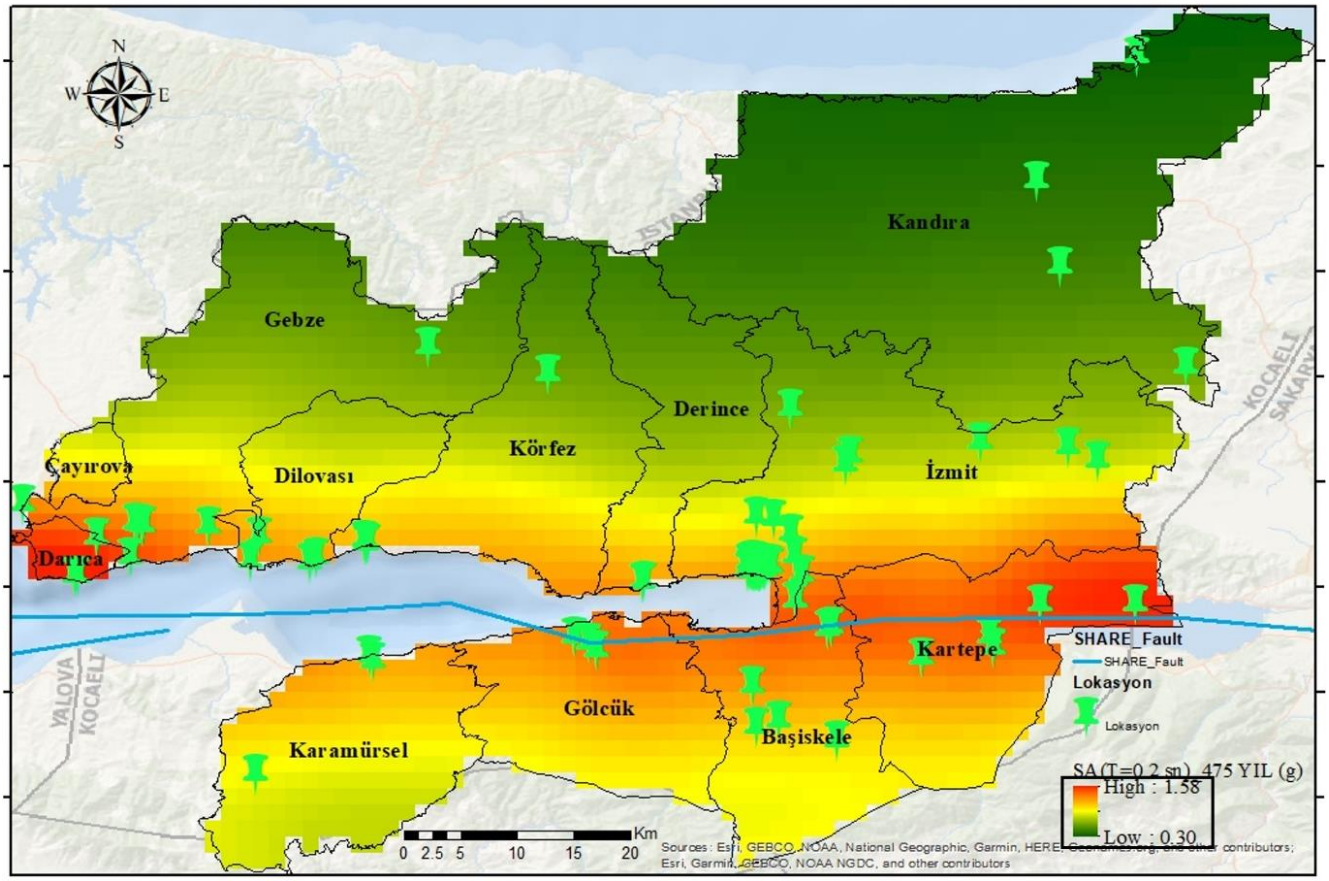

Fig. 14. $Sa(0.2)(g)$ level distribution for DD-2 earthquake ground motion level without $(Vs)_{30}$.

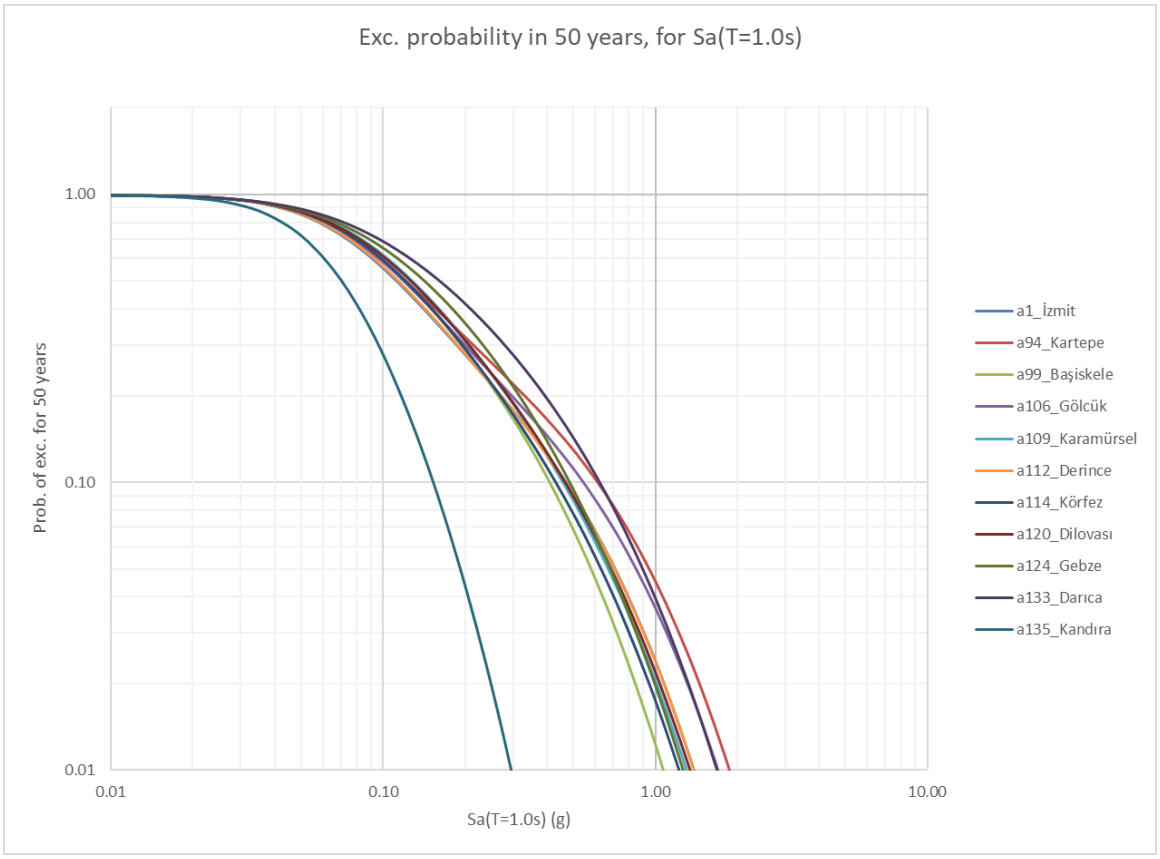

Fig. 15. *Sa*(1.0)(g) level distribution for DD-2 earthquake ground motion level without $(Vs)_{30}$.

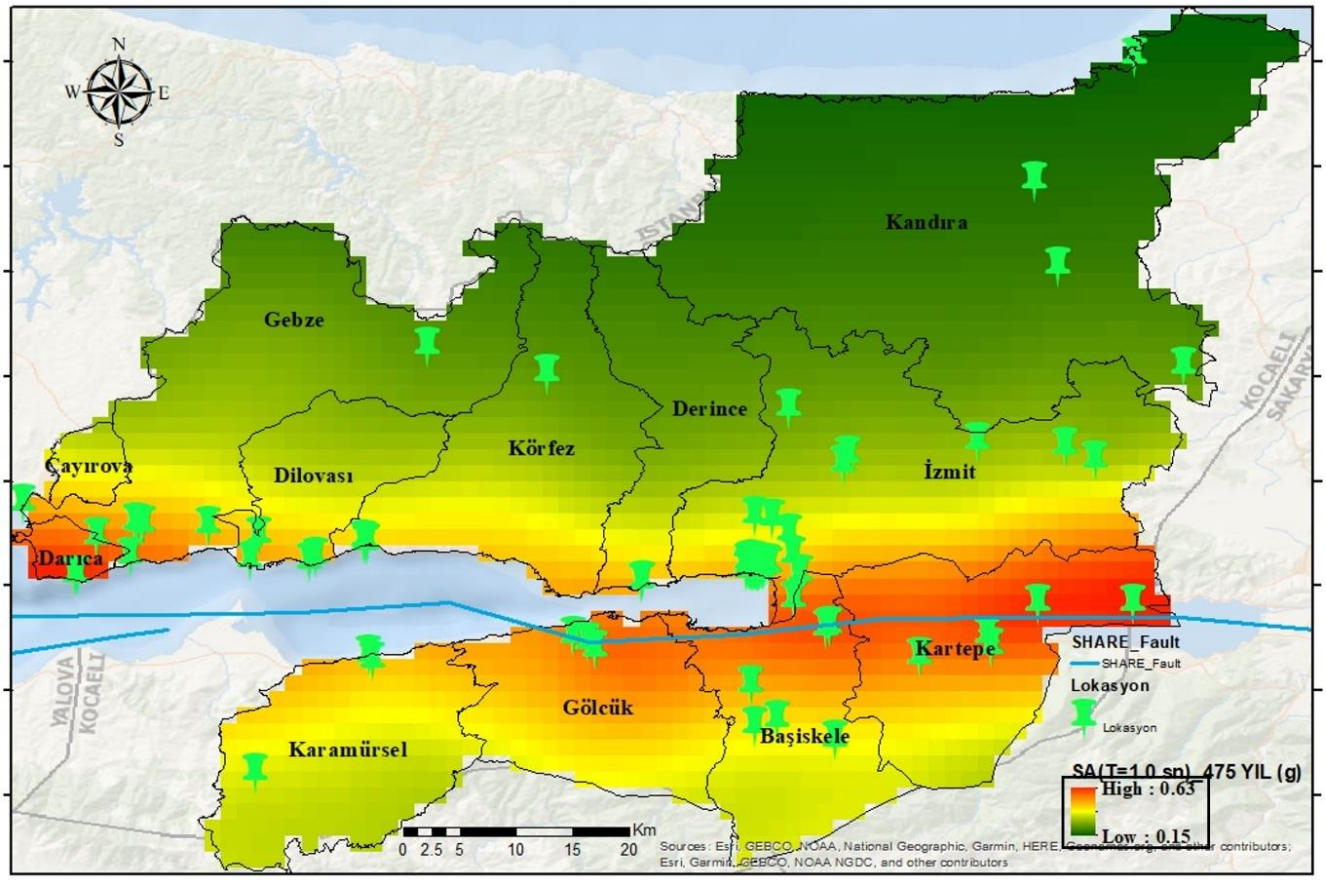

Fig. 16. *Sa*(1.0)(g) level distribution for DD-2 earthquake ground motion level without $(Vs)_{30}$.

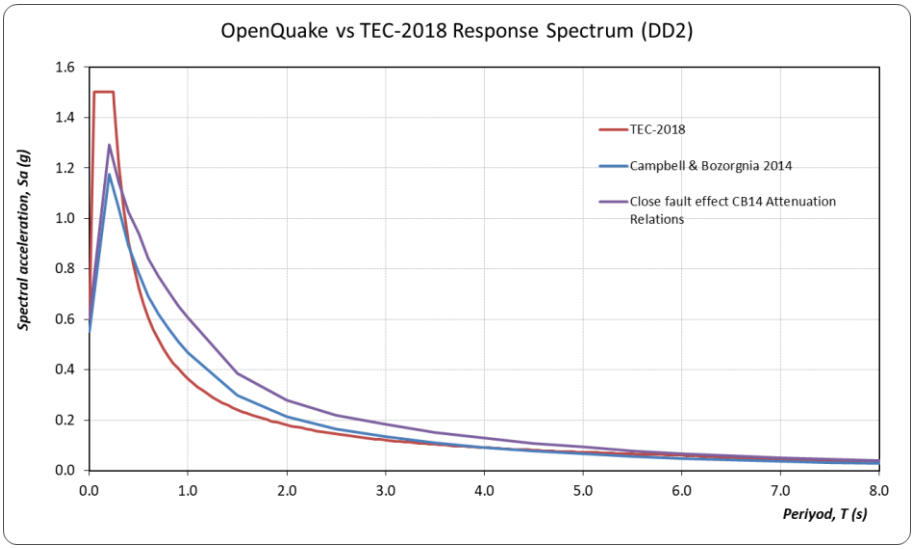

Fig. 17. Comparison of TEC-2018 spectrum with Campbell and Bozorgnia (2014) attenuation relationship and near-fault effect spectra obtained from OpenQuake for DD-2 earthquake ground motion level at İzmit location.

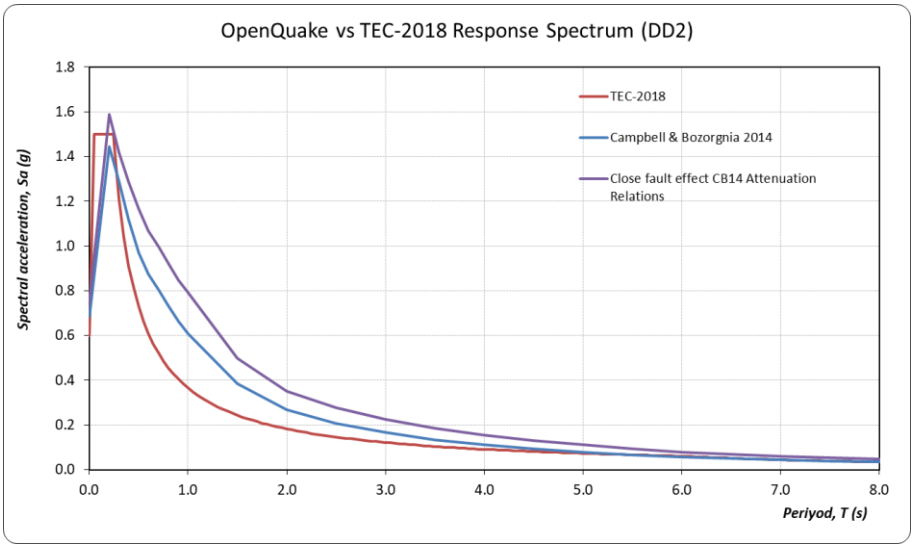

Fig. 18. Comparison of TEC-2018 spectrum with Campbell and Bozorgnia (2014) attenuation relationship and near-fault effect spectra obtained from OpenQuake for DD-2 earthquake ground motion level at Kartepe location.

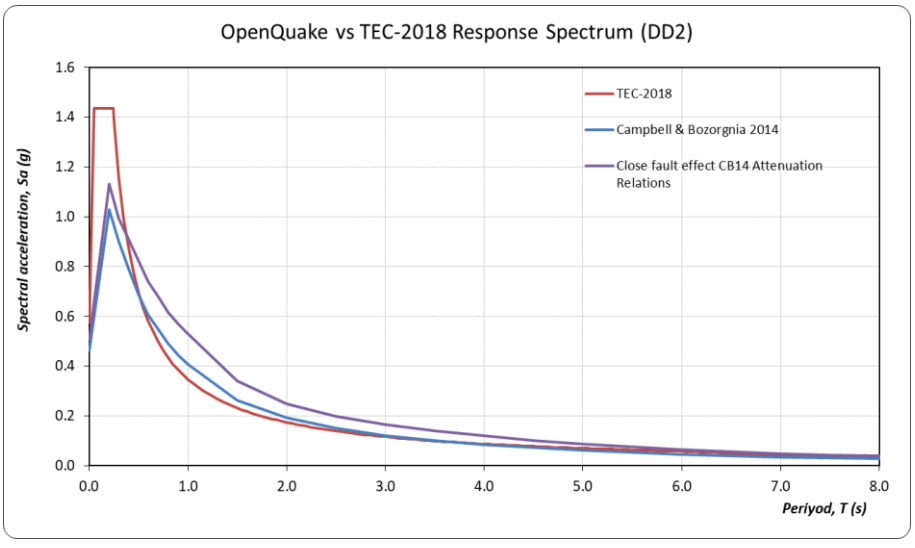

Fig. 19. Comparison of TEC-2018 spectrum with Campbell and Bozorgnia (2014) attenuation relationship and near-fault effect spectra obtained from OpenQuake for DD-2 earthquake ground motion level at Başiskele location.

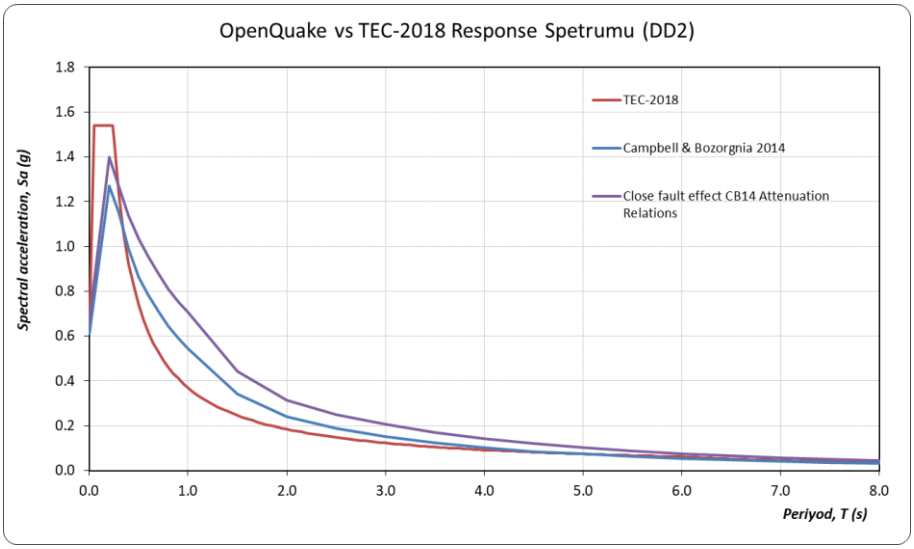

Fig. 20. Comparison of TEC-2018 spectrum with Campbell and Bozorgnia (2014) attenuation relationship and near-fault effect spectra obtained from OpenQuake for DD-2 earthquake ground motion level at Gölcük location.

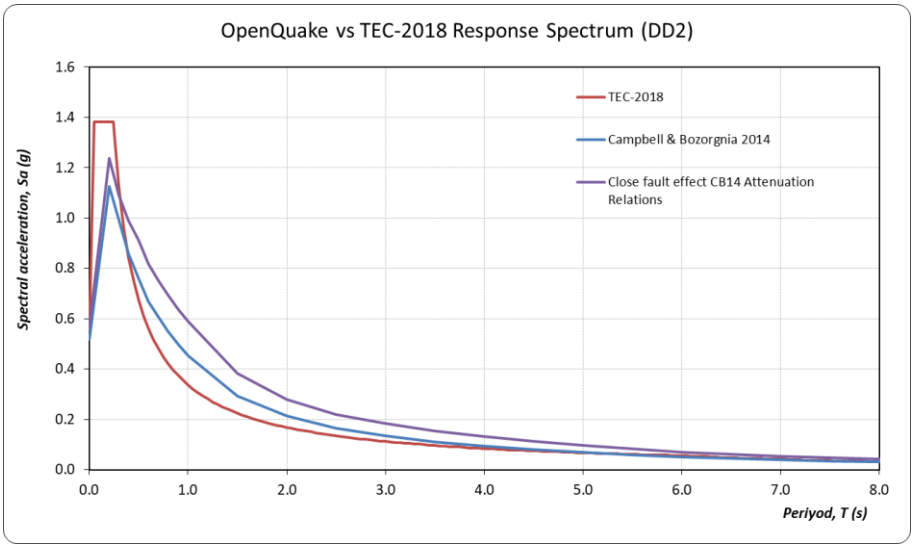

Fig. 21. Comparison of TEC-2018 spectrum with Campbell and Bozorgnia (2014) attenuation relationship and near-fault effect spectra obtained from OpenQuake for DD-2 earthquake ground motion level at Karamürsel location.

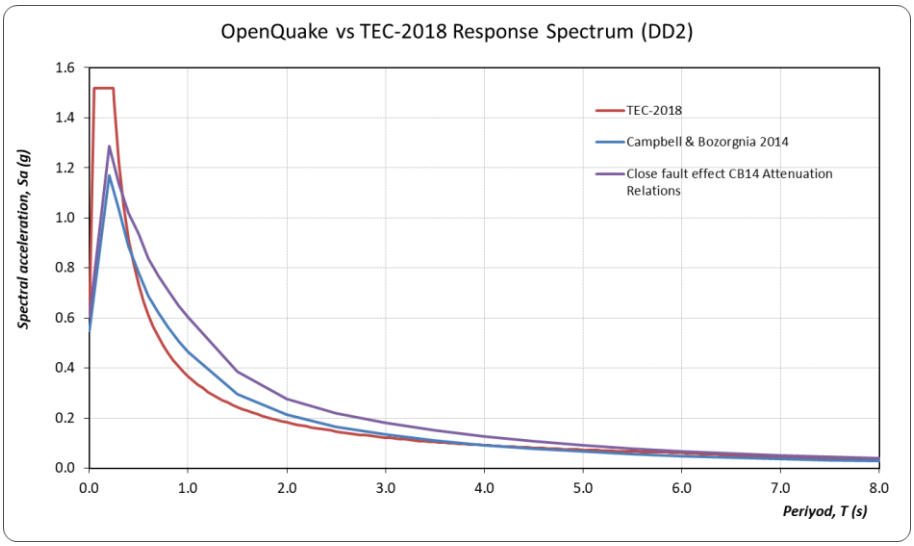

Fig. 22. Comparison of TEC-2018 spectrum with Campbell and Bozorgnia (2014) attenuation relationship and near-fault effect spectra obtained from OpenQuake for DD-2 earthquake ground motion level at Derince location.

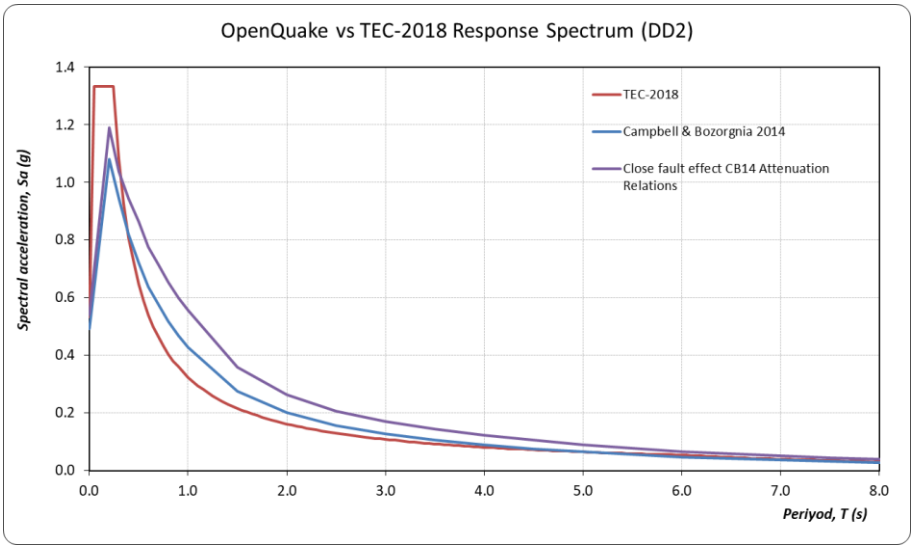

Fig. 23. Comparison of TEC-2018 spectrum with Campbell and Bozorgnia (2014) attenuation relationship and near-fault effect spectra obtained from OpenQuake for DD-2 earthquake ground motion level at Körfez location.

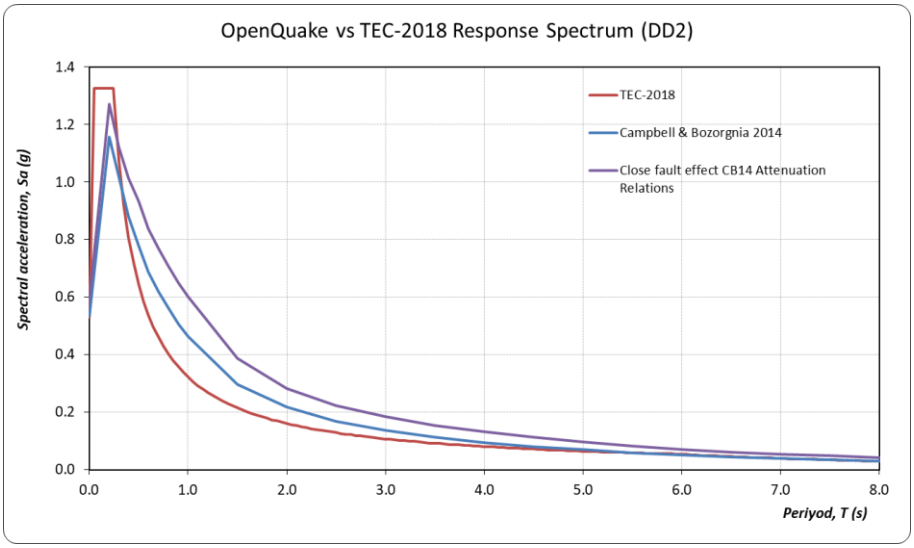

Fig. 24. Comparison of TEC-2018 spectrum with Campbell and Bozorgnia (2014) attenuation relationship and near-fault effect spectra obtained from OpenQuake for DD-2 earthquake ground motion level at Dilovası location.

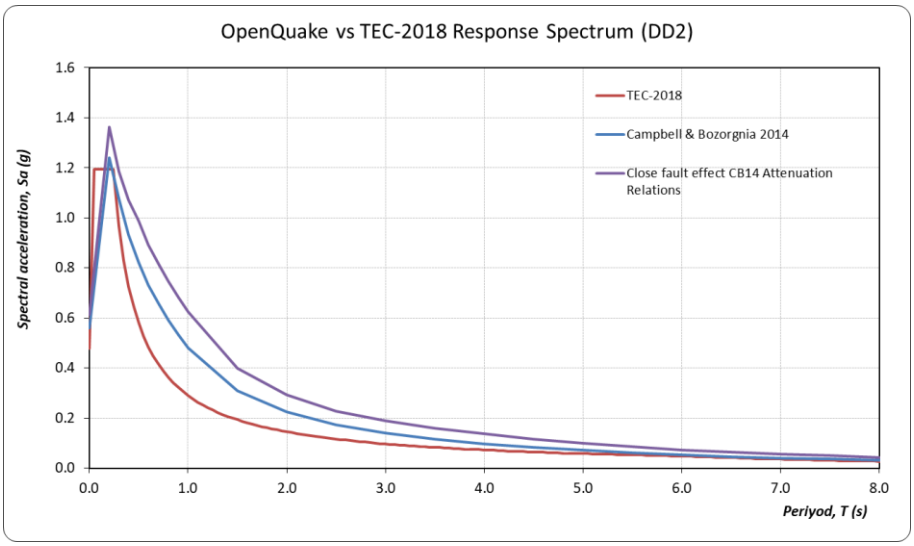

Fig. 26. Comparison of TEC-2018 spectrum with Campbell and Bozorgnia (2014) attenuation relationship and near-fault effect spectra obtained from OpenQuake for DD-2 earthquake ground motion level at Gebze location.

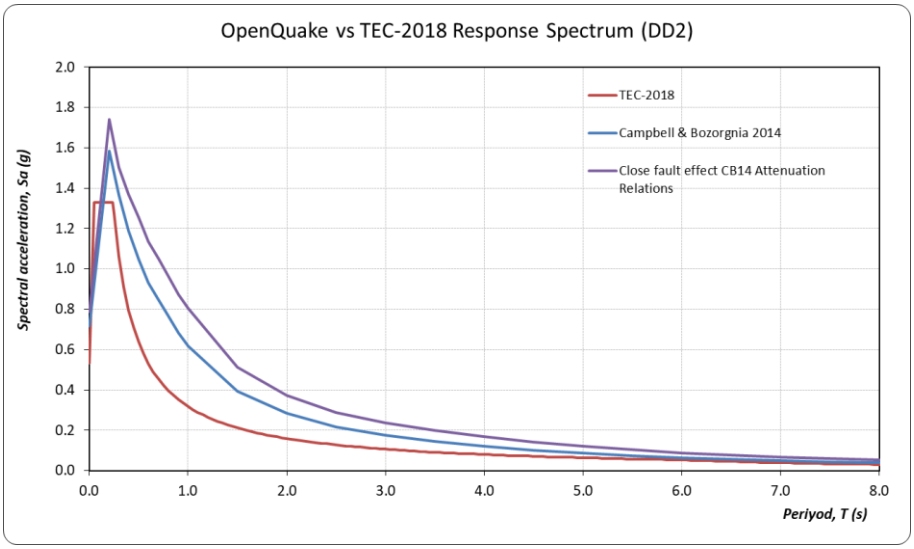

Fig. 26. Comparison of TEC-2018 spectrum with Campbell and Bozorgnia (2014) attenuation relationship and near-fault effect spectra obtained from OpenQuake for DD-2 earthquake ground motion level at Darıca location.

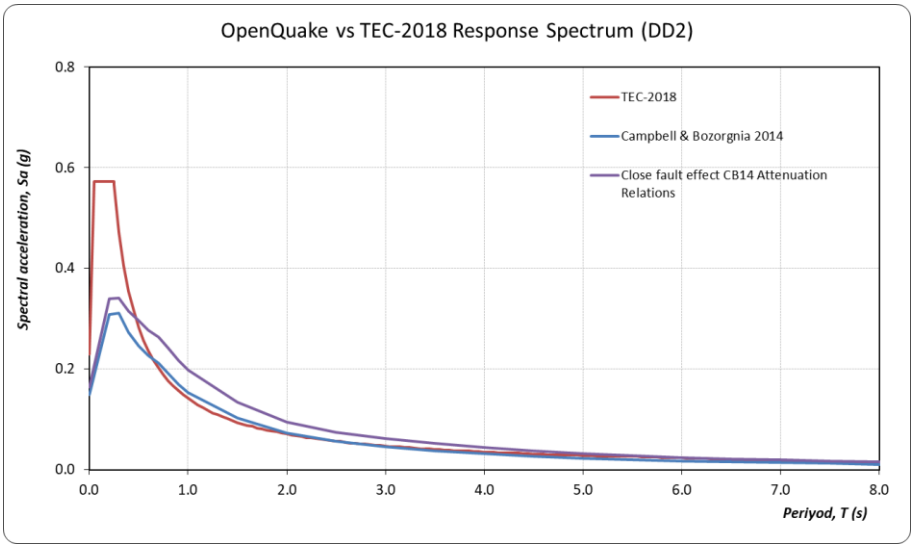

Fig. 27. Comparison of TEC-2018 spectrum with Campbell and Bozorgnia (2014) attenuation relationship and near-fault effect spectra obtained from OpenQuake for DD-2 earthquake ground motion level at Kandıra location.

In this study, there are 138 structures evaluated in this study, and these structures are categorized according to their types. Appropriate fragility curves for this building group, which consists entirely of masonry structures, have been investigated considering geographical applicability and structural features. Fragility curves determined according to the structures after the OpenQuake program library and literature research are given in Table 4.

Seismic risk estimations inherently involve various sources of uncertainty, particularly when applied to historical masonry structures with limited empirical data. In this study, two major sources of uncertainty were identified: (1) the use of international fragility curves, and (2) potential limitations within the building inventory data.

Due to the lack of region-specific empirical damage data for Turkish historical masonry buildings, fragility curves developed in different geographical and construction contexts were utilized. While these curves represent best available proxies, they may not fully capture the unique structural characteristics, material behavior, and construction practices of local heritage structures. As such, their application introduces uncertainty into the predicted damage distributions and associated risk levels.

When the results are examined, it is predicted that most of the structures will be damaged. At the same time, it was predicted that relatively few buildings would suffer mild to moderate damage and, as expected, a smaller number of building groups would suffer severe damage. Due to the relatively small number of structures examined in terms of a risk study, it is more meaningful to make the risk assessment proportionally within the scope of this study. In this context, when the building groups are interpreted by evaluating their ratio to all buildings, it has been determined that the risk values are tower-type structures, aqueduct-bridges, residential-type structures and domed structures, respectively, from high to low. At this point, the reason why domed structures are in the last place among the examined

building types is thought to be due to the selection of the ones that can be used most closely, since the appropriate fragility curves for some different structures included in this study (such as mosques, some masjids) cannot be found in the literature. It should be noted that the assumptions made due to the limited number of the analyzed building stock, the relatively small number of some building groups compared to the others, the distribution of the structures and their distance from the fault sources, and the lack of sufficient number of fragility curves specific to different structures in the literature affect the results.

Table 4. Fragility curves used in the study.

Building Type	Number of Floors	Reference	Taxonomy	Number of Buildings
Building (Housing, Mansion, etc.)	1	Erberik (2008)	MUR+CBH+MOL/LWAL/HEX:1/IRIR+IRPP: TOR+IRPS:IRN (GEM)	7
Building (Housing, Mansion, etc.)	2	Erberik (2008)	MUR+CBH+MOL/LWAL/HEX:2/IRIR+IRPP: TOR+IRPS:IRN (GEM)	55
Building (Housing, Mansion, etc.)	3	Erberik (2008)	MUR+CBH+MOL/LWAL/HEX:3/IRIR+IRPP: TOR+IRPS:IRN (GEM)	18
Building (Housing, Mansion, etc.)	4	Erberik (2008)	MUR+CBH+MOL/LWAL/HEX:4/IRIR+IRPP: TOR+IRPS:IRN (GEM)	3
Domed Structures (Mosque, Church, Some Masjids and Baths)	-	Hofer et al. (2018)	M99/LWAL/RSH7	42
Aqueduct and Bridges	-	Tecchio et al. (2016)	M99/COM+COM6/RSH7	12
Clock Tower	-	Durgut et al. (2021)	M99/LWAL/COM/PLFSQ	1

Table 5. Distribution of damage levels by building types.

Building Type	No Damage	Slight-Moderate	Extreme-Compete	Number of Buildings
Building Structures	49.531	10.898	22.570	83
Domed Structures	32.461	3.899	5.640	42
Aqueduct and Bridges	6.816	1.870	3.314	12
Clock Tower	0.090	0.232	0.680	1
Total	88.899	16.899	32.204	138

While seismic risk assessment provides a quantitative basis for identifying structurally vulnerable buildings, effective conservation planning must also consider the cultural and historical significance of these assets. Structures such as towers and aqueducts, although assessed as high-risk in terms of seismic vulnerability, may vary in their heritage value depending on historical context, architectural uniqueness, and community relevance. Therefore, conservation prioritization should be based on a balanced approach that combines structural fragility with cultural importance. This dual-criteria framework can help authorities ensure that limited restoration and retrofitting resources are directed not only toward the most physically endangered structures, but also those with the highest historical and symbolic value to society.

5. Conclusions

Türkiye is prone to earthquakes due to its location, so it is considered necessary to conduct regional or comprehensive hazard and risk analyses for a broad range of building types to determine which buildings are at risk. In this context, fragility curves, which are critical data in risk analysis, are not found in sufficient numbers, especially in Türkiye, which hosts a wide range of building types. Consequently, it would be beneficial to develop structure-specific fragility curves to improve the efficiency of risk analysis.

In this part of the study, the results of seismic hazard and risk analyzes were examined and the results were discussed. Based on the hazard curves generated by OpenQuake hazard analysis, the following conclusions can be drawn. The majority of the 11 reference locations in the investigation area are located near faults. From these locations, it is seen that the values in locations such as Darıca, Gölcük, Kartepe, which are relatively close to the faults, give higher values compared to other points. However, the values obtained in Kandıra district, which is farther from the faults compared to other regions, were lower.

In the three different hazard curves obtained against the spectral periods of PGA, $Sa(0.2)$ and $Sa(1.0)$, the values of Kandıra district yielded lower results compared to other locations. DD-2 earthquake ground motion level from these three different graphs indicate that the hazard values of Kandıra district vary between 0.15-0.30 (g), while in other locations, it was between 0.40-1.00 (g) and in the curves obtained for $Sa(0.2)$. It was observed that these values reached 1.50 (g) levels at points such as Darıca and Kartepe, which were relatively close to the faults.

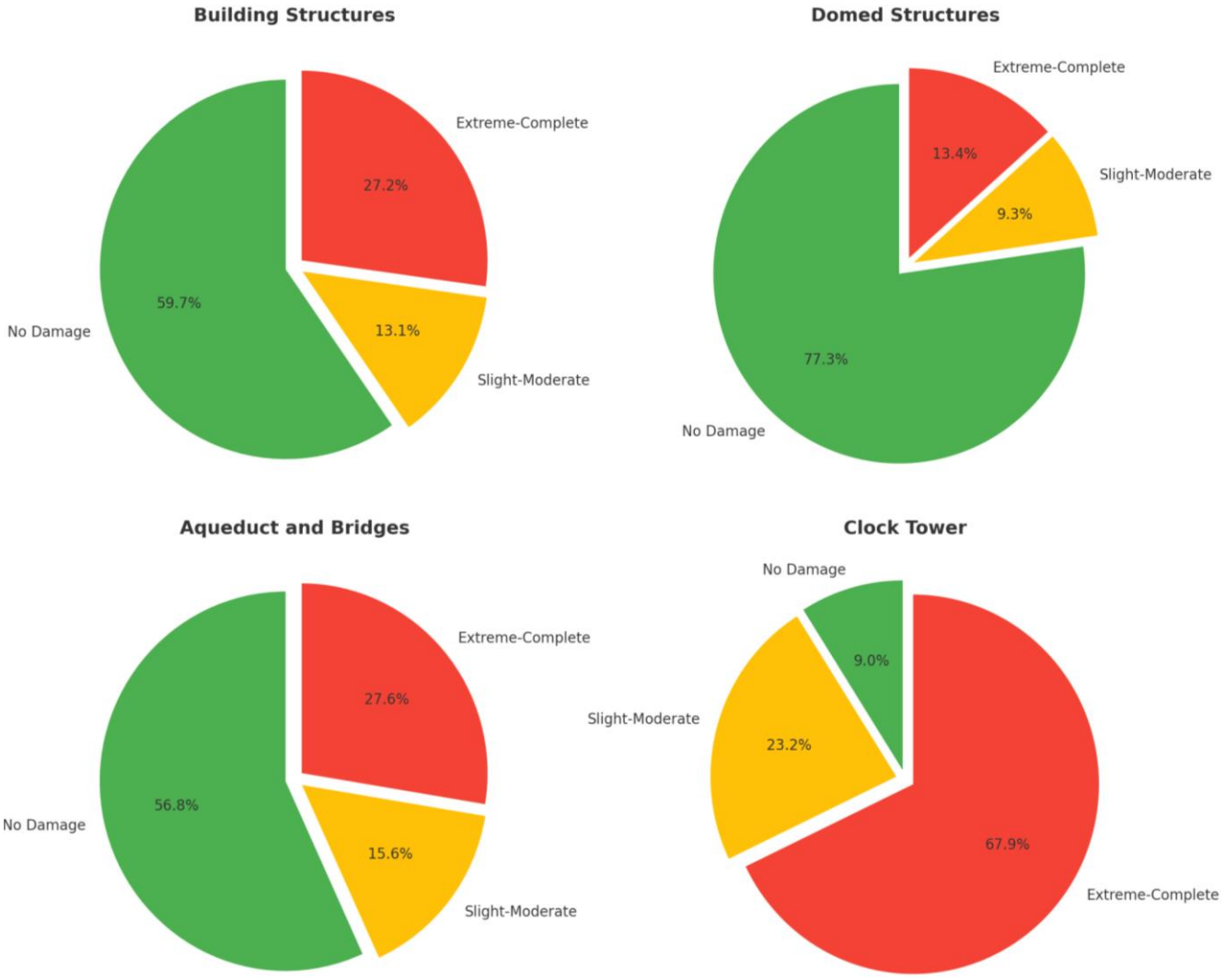

Fig. 28. Distribution percentage of damage levels by building groups.

When looking at the general earthquake hazard maps obtained in response to the DD-2 earthquake ground motion level and PGA, *Sa*(0.2) and *Sa*(1.0) spectral periods, a certain level of detection is detected in the middle section covering the northern parts of Karamürsel, Gölcük, Başiskele districts from the southern part of Kandıra district. The intensity distributions obtained increased on a point basis depending on their proximity to the fault but remained in an average range. In addition, decreases in values are observed in the northern parts of Kandıra district and in the southern borders of Karamürsel and Başiskele districts, which are far from the faults compared to other locations. It is possible to interpret the maps in detail as follows.

When the results obtained for the PGA were examined, the values obtained for the DD-2 earthquake ground motion level were in the range of 0.28-0.76 (g), while this value increases to 0.88 (g) in locations close to the fault and decreases to 0.16 (g) in the northern borders of Kandıra district and the southern end of the investigation area. When the results obtained for *Sa*(0.2) are examined, the values obtained for the DD-2 earthquake ground motion level are in the range of 0.62-1.46 (g), while this value is at the level of 0.35 (g) in the northern borders of Kandıra district and the southern end of the target area. When the results obtained for *Sa*(1.0) are examined, the values obtained for the DD-2 earthquake ground motion level are in the range of 0.26-0.68 (g), while this value increases to 0.68-0.79 (g) levels in locations close to the fault, and decreases to 0.15 (g) in the northern borders of Kandıra district and the southern parts of the target area.

Risk studies of different building groups, regional and more comprehensive hazard studies, and hazard analyses using deterministic approaches have been published in the literature. Nevertheless, this study is at a critical point in terms of earthquake activity, as explained in the previous sections. The probabilistic approach covers evaluating a wide range of parameters within the possibilities rather than the deterministic approach. Therefore, it is considered to be a study that includes many features, including the necessity of protection. It presents information about the material used, the building type, and the period when it was built, among others.

Although domed structures were ranked as having the lowest seismic risk among the structural typologies analyzed, this result should be interpreted with caution. The absence of typology-specific fragility curves for domed heritage structures, such as mosques and some churches, likely results in an underestimation of their ac-

tual vulnerability. This limitation stems from the necessity to adopt proxy fragility curves that may not adequately reflect the dynamic behavior of such geometrically complex and historically unique structures. Therefore, the risk categorization presented in this study does not fully capture the seismic fragility of domed buildings and highlights the need for future empirical calibration based on field testing and structural monitoring.

In future studies, the development of fragility curves specifically calibrated for Turkish historical masonry structures is strongly recommended. These curves should be based on empirical damage data and structural monitoring from local case studies to more accurately reflect the behavior of region-specific building typologies under seismic loading. Additionally, integrating seismic risk outputs into regional early warning systems and conservation prioritization frameworks can significantly enhance proactive risk mitigation for cultural heritage assets. Such integration would allow authorities to make data-driven decisions for emergency preparedness, resource allocation, and long-term resilience planning. Moreover, on-site dynamic testing and modal analyses of representative structures are suggested to support numerical model calibration and further reduce uncertainties in both hazard and risk assessments.

Acknowledgements

None declared.

Funding

The authors received no financial support for the research, authorship, and/or publication of this manuscript.

Conflict of Interest

The authors declare no potential conflicts of interest with respect to the research, authorship, and/or publication of this manuscript.

Data Availability

The datasets generated and/or analyzed during the current study are not publicly available but are available from the corresponding author upon reasonable request.

AI Assistance

During the preparation of this manuscript, ChatGPT-5 (OpenAI) was used exclusively for image creation, language editing and stylistic refinement. The authors take full responsibility for the content, interpretation, and conclusions of the published article.

Author Contributions

All authors made substantial contributions to the conception and design of the study, acquisition of data, analysis and interpretation of data; drafted or critically revised the manuscript for important intellectual content; and approved the final version to be published.

REFERENCES

Abrahamson N, Silva W (2008). Summary of the Abrahamson & Silva Nga Ground-motion relations. *Earthquake Spectra*, 24, 67–97.

Abrahamson NA, Silva WJ, Kamai R (2014). Summary of the ASK14 ground motion relation for active crustal regions. *Earthquake Spectra*, 30, 1025–1055.

Ademović N, Demir V, Cvijić-Amulić S, Málek J, Prachař I, Vackář J (2021). Compilation of the seismic hazard maps in Bosnia and Herzegovina. *Soil Dynamics and Earthquake Engineering*, 141.

Akın S, Alagöz A (2024). Structural behavior of historical Obruk Inn under different earthquakes. *Challenge Journal of Structural Mechanics*, 10(1), 21-33.

Akkar S, Cagnan Z (2010). A local ground-motion predictive model for Turkey, and its comparison with other regional and global ground-motion models. *Bulletin of the Seismological Society of America*, 100, 2978–2995.

Akkar S, Sandıkkaya MA, Bommer JJ (2013). Empirical ground-motion models for point and extended-source crustal earthquake scenarios in Europe and the Middle East. *Bulletin of Earthquake Engineering*, 12, 359–387.

Aksoy T (2011). Kocaeli Cultural Inventory. Kocaeli Metropolitan Municipality Department of Culture and Social Affairs Culture Publishing, Kocaeli, Türkiye.

Arzomand K, Rustell M, Kalganova T (2024). From ruins to reconstruction: Harnessing text-to-image AI for restoring historical architectures. *Challenge Journal of Structural Mechanics*, 10(2), 69-85.

Biglari M, Formisano A, Davino A (2022). Seismic vulnerability assessment and fragility analysis of Iranian historical mosques in Kermanshah City. *Journal of Building Engineering*, 45.

Boore DM, Atkinson GM (2008). Ground-motion prediction equations for the average horizontal component of PGA, PGV, and 5%-damped PSA at spectral periods between 0.01*s*and 10.0*s*. *Earthquake Spectra*, 24, 99–138.

Boore DM, Stewart JP, Seyhan E, Atkinson GM (2014). NGA-WEST2 equations for predicting PGA, PGV, and 5% damped PSA for shallow crustal earthquakes. *Earthquake Spectra*, 30, 1057–1085.

Campbell KW, Bozorgnia Y (2008). NGA ground motion model for the geometric mean horizontal component of PGA, PGV, PGD and 5% damped linear elastic response spectra for periods ranging from 0.01 to 10 s. *Earthquake Spectra*, 24, 139–171.

Campbell KW, Bozorgnia Y (2014). Nga-West2 ground motion model for the average horizontal components of PGA, PGV, and 5% damped linear acceleration response spectra. *Earthquake Spectra*. 30, 1087–1115.

Çetin C, Erberik MA (2017). Kırılganlık eğrileri kullanılarak elde edilen tahmini hasar dağılımının hasar tespit verileriyle karşılaştırılması. *Fourth International Conference on Earthquake Engineering and Seismology*, Eskişehir, Türkiye. (in Turkish)

Chiou BSJ, Youngs RR (2008). An NGA model for the average horizontal component of peak ground motion and Response Spectra. *Earthquake Spectra*, 24(1), 173–215.

Chiou BSJ, Youngs RR (2014). Update of the Chiou and Youngs Nga model for the average horizontal component of peak ground motion and Response Spectra. *Earthquake Spectra*, 30, 1117–1153.

Cuadra C, Karkee MB, Tokeshi K (2008). Earthquake risk to Inca's historical constructions in Machupicchu. *Advances in Engineering Software*, 39, 336–345.

Durgut E, Kuran F, Ispir M, Demir C, Turan ÖT, İlki A (2021). Bursa ilindeki tarihi minarelerin kırılganlık eğrilerinin elde edilmesi. *Bursa Historical Mosque Minarets Earthquake Behavior Workshop*, İstanbul, Türkiye. (in Turkish)

Erberik MA (2008). Generation of fragility curves for Turkish masonry buildings considering in-plane failure modes. *Earthquake Engineering & Structural Dynamics*, 37, 387–405.

Fazzi E, Galassi S, Misseri G, Rovero L (2021). Seismic vulnerability assessment of the Benedictine basilica typology in Central Italy. *Journal of Building Engineering*, 43.

Gövsulu G (2020). CRISIS (2015) Programı Kullanılarak İzmir İli Urla-Çeşme-Karaburun Çevresi Sismik Tehlike Analizi. *M.Sc. thesis*, Dokuz Eylül University, İzmir, Türkiye. (in Turkish)

Gündoğdu Gök M (2020). Monte Carlo Yöntemi İle Kocaeli İli ve Çevresi İçin Olasılıksal Deprem Tehlike Analizi. *M.Sc. thesis*, Gebze Technical University, Kocaeli, Türkiye. (in Turkish)

Hofer L, Zampieri P, Zanini MA, Faleschini F, Pellegrino C (2018). Seismic damage survey and empirical fragility curves for churches after the August 24, 2016 Central Italy earthquake. *Soil Dynamics and Earthquake Engineering*, 111, 98–109.

Hoveidae N, Fathi A, Karimzadeh S (2021). Seismic damage assessment of a historic masonry building under simulated scenario earthquakes: A case study for Arge-Tabriz. *Soil Dynamics and Earthquake Engineering*, 147, 106732.

Kramer S (1996). Geotechnical Earthquake Engineering. First ed. Prentice Hall, New Jersey, USA.

Lourenço PB, Oliveira DV, Leite JC, Ingham JM, Modena C, da Porto F (2013). Simplified indexes for the seismic assessment of masonry buildings: International database and validation. *Engineering Failure Analysis*, 34, 585–605.

Merdan Tutar Z, Zülfikar AC, Demircioğlu MB, Kariptaş Ç (2017). 1999 Kocaeli Depremi'nin Deprem Tehlikesi ve Riski Açısından Kocaeli İlindeki Etkisi. *Fourth International Conference on Earthquake Engineering and Seismology*, Eskişehir, Türkiye. (in Turkish)

Oktay S, Taş N, Taş M (2020). Kültürel Miras Alanlarının Korunması ve Afet Yönetimi İlişkisi. *Resilience*, 2, 305-321. (in Turkish)

Pirchio D, Walsh KQ, Kerr E, Giongo I, Giaretton M, Weldon BD (2021). Seismic risk assessment and intervention prioritization for Italian medieval churches. *Journal of Building Engineering*, 43, 103061.

TEC (2018). Turkish Earthquake Code. Republic of Türkiye Ministry of Interior, Disaster and Emergency Management Authority (AFAD), Ankara, Türkiye.

Tecchio G, Donà M, da Porto F (2016). Seismic fragility curves of as-built single-span Masonry Arch Bridges, *Bulletin of Earthquake Engineering*, 14, 3099–3124.

VGM (2017). Guide to the International Symposium of Earthquake Risk Management of Historical Structures. https://www.vgm.gov.tr/organizasyonlar/tarihi-yapilarda-deprem-risklerinin-yonetimi-uluslararasi-sempozyumu/kilavuz/ [accessed 02 February 2022].

Yücemen M (2011). Olasılıksal sismik tehlike analizi: Genel bakış ve istatiksel modellemede dikkat edilmesi gerekli hususlar. *1st Turkey Earthquake Engineering and Seismology Conference*, Ankara, Türkiye. (in Turkish)

Zardari S, Kutlu İ, Nayeb A (2024). Investigation of structural performances of historical building elements made with local materials using the finite element method. *Challenge Journal of Concrete Research Letters*, 15(3), 101-111.

Zhao JX (2006). Attenuation relations of strong ground motion in Japan using site classification based on predominant period. *Bulletin of the Seismological Society of America*, 96, 898–913.

Zülfikar AC, Okuyan Akcan S, Yeşilyurt A, Eröz M, Cimilli T (2021). Kritik enerji tesislerinin deprem risk değerlendirmesinde farklı hasargörebilirlik fonksiyonlarının incelenmesi. *Çukurova University Faculty of Engineering Journal*, 36(4), 1019-1032. (in Turkish)

Challenge Journal of STRUCTURAL MECHANICS

Research Article

Development of a sustainable geopolymer structural element with waste glass powder: Mechanical characteristics

Serdal Ünal [a], Mehmet Canbaz [a,*]

[a] *Department of Civil Engineering, Eskişehir Osmangazi University, 26480 Eskişehir, Türkiye*

ABSTRACT

In this study, the potential of converting waste glass powder, sourced from glass manufacturing processes in Turkey, into sustainable and environmentally friendly construction materials was explored. A novel approach was adopted by producing geopolymeric building elements using only waste glass powder, water, and varying concentrations of sodium hydroxide (2%, 4%, and 6%) in a completely cement-free system. This distinguishes the study from previous works, as it focuses solely on waste glass powder as the primary aluminosilicate source without incorporating additional binders such as fly ash or slag. The physical and mechanical properties of the produced samples were evaluated through unit weight, ultrasonic pulse velocity, compressive strength, flexural strength, and tensile strength tests. The results indicated that the mixture containing 4% sodium hydroxide provided optimal performance, demonstrating superior mechanical strength, structural integrity, and durability. Notably, the specimens produced with 4% NaOH exhibited higher durability than aerated concrete and achieved strength and density values close to conventional bricks, suggesting their potential applicability in non-load-bearing structural elements. Furthermore, this study addresses a significant gap in the literature regarding the standalone use of waste glass powder in geopolymer systems and contributes valuable data on its performance in solid form. The findings also highlight the material's potential to reduce reliance on Portland cement, thereby lowering carbon emissions and promoting the circular economy through effective waste utilization. Overall, the study offers an innovative and practical solution for sustainable construction by demonstrating the feasibility of producing high-performance geopolymer elements entirely from waste-derived materials.

ARTICLE INFO

Article history:
Received – May 1, 2025
Revision requested – June 2, 2025
Revision received – June 10, 2025
Accepted – June 20, 2025

Keywords:
Waste glass powder
Geopolymer
Sustainable construction materials
Carbon footprint

Citation: Ünal S, Canbaz M (2026). Development of a sustainable geopolymer structural element with waste glass powder: Mechanical characteristics. *Challenge Journal of Structural Mechanics*, 12(1), 22–29.

1. Introduction

In recent years, sustainability, environmental impact reduction, and the adoption of circular economy principles have become increasingly critical in the construction industry (Charef et al. 2022). In this context, the high carbon emissions and energy consumption associated with the production of traditional Portland cement have driven research into alternative binder systems. Geopolymers, produced through the alkali activation of aluminosilicate-rich industrial by-products such as fly ash, blast furnace slag, and metakaolin, have emerged as environmentally friendly and low-carbon alternatives to conventional cementitious materials (Davidovits 2015; Ślosarczyk et al. 2023; Nasir et al. 2024). These materials not only offer comparable or superior mechanical performance and durability but also significantly reduce the environmental footprint of construction materials (Sbahieh et al. 2023; Imbabi et al. 2012). Additionally, the flexibility of geopolymer technology allows for the incur-

* *Corresponding author*. E-mail address: mcanbaz@ogu.edu.tr (M. Canbaz)
ISSN: 2149-8024 / DOI: https://doi.org/10.20528/cjsmec.2026.01.002

poration of various locally available waste materials, such as waste glass powder, further enhancing its sustainability potential and applicability across different regions. Furthermore, the utilization of waste materials in geopolymer production contributes to waste valorization and offers economic and ecological advantages, supporting broader goals of sustainable development in the built environment (Kriven et al. 2024; Hegyi et al. 2023; Gao et al. 2023). Accordingly, recycling waste streams such as expired cement and aged roof tile powders as alternative binders can reduce industrial waste while lowering natural resource consumption and supporting more environmentally friendly mortar and concrete production (Ünal and Canbaz 2025). Moreover, the rapid growth of electronic waste and end of life rubber products has created pressing environmental and public health concerns, prompting their evaluation as secondary raw materials in cementitious and alternative binder systems (Bulut 2024). Similarly, the reuse of waste fiber reinforced polymer composite laminates originally produced for structural strengthening can support circular economy targets by reducing composite waste (Çelik et al. 2024).

Waste glass powder, due to its high silica content and amorphous structure, has attracted considerable attention as a potential precursor for geopolymer synthesis (Luhar et al. 2019; Siddika et al. 2021). Recycled materials such as waste glass powder are widely used, especially in lightweight building elements, geopolymers, fillers, and briquette production. These types of materials are often preferred in non-structural or semi-structural applications such as interior wall blocks, insulation elements, and decorative coatings. When finely ground, waste glass becomes highly reactive, enabling the formation of binding gels such as sodium-alumino-silicate-hydrate (N-A-S-H) upon alkali activation (Zhang 2015; Manjunath and Narasimhan 2020). The incorporation of glass powder into construction materials has been shown to improve mechanical properties, enhance durability, and reduce water absorption (Asokan et al. 2010). In addition, waste glass powder contributes to the formation of a more compact matrix by improving the microstructure of concrete thanks to its pozzolanic properties and fine grain structure (Barbhuiya et al. 2025; Amin et al. 2024). Some studies have shown that glass powder, especially when finely ground, promotes C–S–H gel formation, thereby enhancing its binding effect (Lam et al. 2024; Lai and Chen 2024). Additionally, it has been reported that glass powder can reduce the risk of alkali-silica reaction (ASR) at low usage rates, thereby positively affecting long-term durability (Almakrab et al. 2024). These findings highlight the potential of waste glass powder as an effective additive in concrete and present an important opportunity for sustainable material design. Moreover, utilizing waste glass in construction helps address environmental issues related to glass disposal and reduces the demand for natural raw materials, contributing to resource conservation and landfill reduction. These benefits align with the broader strategies for achieving carbon-neutral construction practices and mitigating the environmental impact of urban development (Huovila et al. 2022).

In this study, the use of waste glass powder sourced from glass manufacturing processes in Turkey was investigated for the production of completely cement-free geopolymeric construction materials. While existing literature includes studies where waste glass is used in combination with other materials such as fly ash or slag (Siddika et al. 2021), Research focusing solely on waste glass powder and sodium hydroxide as the activating agent remains limited. This study differentiates itself by employing only waste glass powder and varying concentrations of sodium hydroxide (2%, 4%, and 6%) to evaluate their effects on the physical and mechanical properties of the resulting geopolymer. This study differs by utilizing 100% waste glass powder as the sole aluminosilicate source in a completely cement-free geopolymer system, addressing the gap in literature regarding its standalone use and structural applicability in building elements. The goal is to determine the optimal alkali content for maximizing performance and to demonstrate that waste glass can serve as a viable precursor in geopolymer production. By doing so, this research contributes both to environmental sustainability and to the advancement of eco-friendly, lightweight, and durable construction materials.

2. Experimental Study

In the production of geopolymers, the glass powder whose chemical, physical, and particle size distribution properties are presented in Table 1 was used. As the activator, sodium hydroxide commonly known as caustic soda was selected due to its widespread use. In geopolymer production, sodium silicate and/or sodium hydroxide are typically preferred as activators. However, due to the high silica content of the glass powder, sodium silicate alone was not chosen. In mixture, Eskişehir tap water, whose properties are given in Table 2, was used.

Table 1. Chemical, physical, and particle size distribution properties of the waste glass.

	SiO_2 (%)	Na_2O (%)	CaO (%)	MgO (%)	Al_2O_3 (%)	Density (gr/dm^3)	10 % (mm)	50 % (mm)	90 % (mm)
Fine glass waste	72.5	13.7	9.8	3.3	0.4	2.504	<0.01	<0.04	<0.13

Table 2. Chemical analysis of the water (mg/lt).

pH	Na_2O	Ka_2O	Cl^-	SO_4	Zn	Pb	P_2O_3	NO_3	∑alkalinity	Color
7.7	54	10	63	21	10	0.05	1.6	0.2	8	Crystal clear

For geopolymer production, the required amounts of sodium hydroxide were first determined based on the ratios provided in Table 3 and then mixed with water. The resulting solution was combined with glass powder to obtain a binder paste mixture. As the particle size of the glass powder decreased (i.e., as it became finer), the surface area increased, leading to a higher water demand. Therefore, higher water-to-glass powder ratios were used to achieve the same plastic consistency.

Table 3. Mixing ratio.

Na, %	2	4	6
Caustic soda / Fine glass waste	0.035	0.070	0.105
Water/ Fine glass waste	0.70	0.70	0.70

The prepared mixtures were poured into prismatic molds, each with three compartments measuring 4x4x16 cm, as shown in Fig. 1. Subsequently, the mixtures were compacted using a table vibrator, and the surfaces were leveled with a trowel. The samples were demolded after 24 hours and placed in an oven at a constant temperature of 60 °C for 3 hours. Afterwards, the samples were stored under standard curing conditions to gain strength. After 28 days from the production date, the dimensions, weights, and ultrasonic pulse velocities of the samples were measured. Flexural strength was tested by applying load at the midpoint of the specimens. Two additional tests were conducted on the broken parts: one part was used to measure the splitting tensile strength, while the other part was subjected to a compressive strength test by placing 4x4 cm plates on the top and bottom surfaces. All experiments were conducted on at least three different samples, and during this process, the unit weights, ultrasonic pulse velocities, compressive, flexural, and tensile strengths of the samples were determined.

Fig. 1. Production, sampling and testing.

3. Results and Discussion

According to the results as seen in Fig. 2, a noticeable change was observed in the unit weight values of geopolymer mortars with increasing sodium content. The unit weight of the mixture containing 2% sodium was 1.577 kg/dm^3, which increased by 10.78% to 1.747 kg/dm^3 with 4% sodium content. However, when the sodium content was raised to 6%, the unit weight decreased to 1.62 kg/dm^3, representing a 7.28% reduction compared to the 4% sodium mixture. These findings indicate that increasing the sodium hydroxide content initially leads to a denser matrix structure, thus increasing the unit weight. Nevertheless, at 6% sodium, the excess alkali likely caused increased micro-porosity or disrupted the homogeneity of the reaction products, leading to a decrease in density. This suggests that exceeding the optimum sodium content may compromise structural integrity, negatively affecting both mechanical and physical properties.

Ultrasonic pulse velocity test results shown in Fig. 3 provide valuable insights into the internal structural integrity and density of geopolymer mortars. At 2% sodium content, the pulse velocity was 0.66 km/s, which increased by 55% to 1.023 km/s at 4% sodium. This significant increase indicates that the higher sodium hydroxide content enhanced reactivity and gel formation, resulting in a more compact and homogeneous structure. However, when the sodium content reached 6%, the pulse velocity dropped to 0.843 km/s—approximately 17.6% lower than that of the 4% mixture. This decline suggests that excess sodium may have induced microstructural voids or cracks within the matrix, reducing wave transmission speed. The results indicate that the optimum sodium content is around 4%, providing a denser and more cohesive geopolymer matrix, whereas higher levels weaken structural integrity.

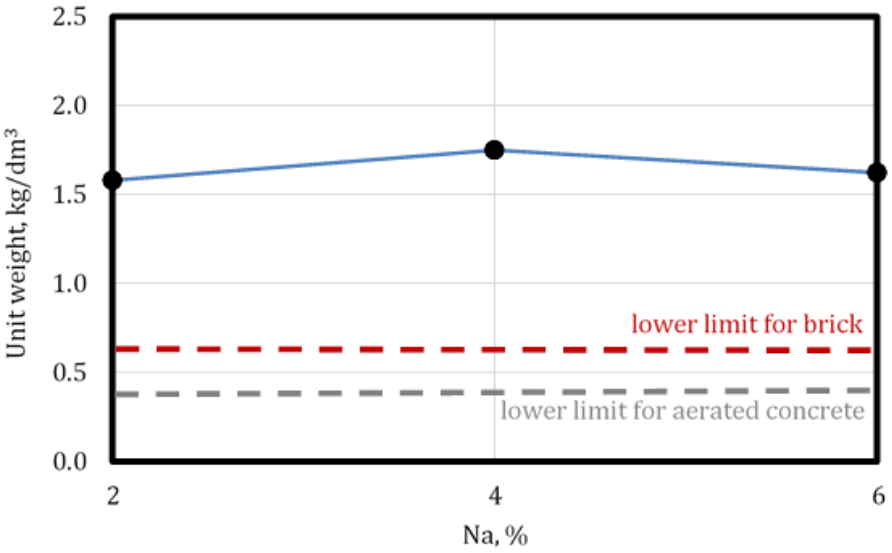

Fig. 2. Unit weight values of geopolymer specimens.

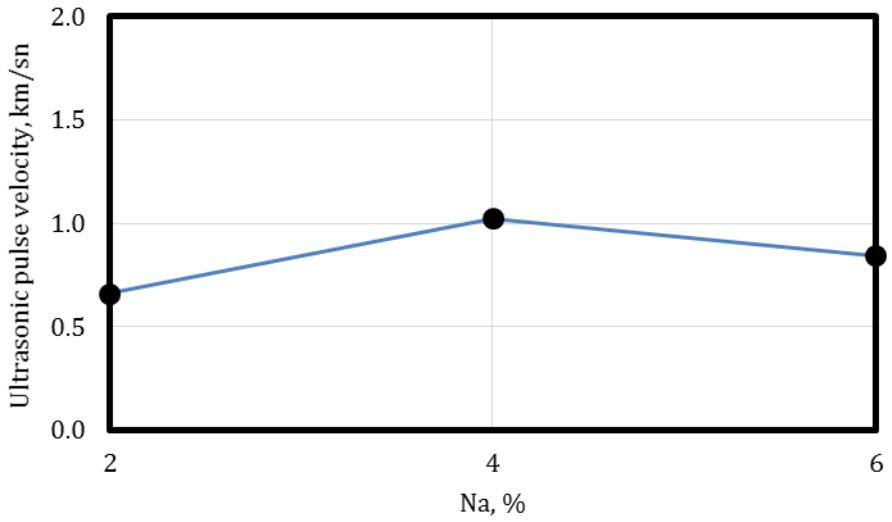

Fig. 3. Ultrasonic pulse velocity values of geopolymer specimens.

Flexural strength results as seen in Fig. 4 clearly demonstrate the influence of sodium hydroxide content on the mechanical properties of the geopolymer mortar. The flexural strength of the mixture with 2% sodium was 1.83 MPa, which increased by approximately 25.7% to 2.3 MPa at 4% sodium. However, when the sodium content was increased to 6%, the flexural strength dropped to 1.777 MPa, showing a 22.7% decrease compared to the 4% mixture. These findings suggest that 4% sodium is the optimum level at which the binder is most effectively activated. While an increase in sodium content initially improves the solubility of glass waste and the degree of geopolymerization, excessive alkali conditions beyond 4% may disrupt the reaction balance and increase the formation of microcracks, ultimately leading to strength reduction. Therefore, flexural strength data underscore the critical importance of optimizing sodium content for improved geopolymer performance.

Compressive strength results shown in Fig. 5 further highlight the significant effect of sodium hydroxide content on the mechanical performance of geopolymer mortars. In the mixture with 2% sodium, the compressive strength was measured at 6.77 MPa. This value increased by approximately 64.3% to 11.12 MPa at 4% sodium. This improvement is attributed to increased solubility and reaction rates within the binder system, contributing to the formation of a more compact and robust matrix. However, with 6% sodium content, the compressive strength slightly decreased to 10.85 MPa—about 2.4% lower than at 4% sodium. Although this decrease is relatively small, it may still indicate a disruption in the reaction balance caused by excessive sodium, leading to microstructural voids or weak bonding. These findings confirm that the optimal sodium level for compressive strength is around 4%, where the binder achieves its highest activation efficiency. Careful control of sodium content is thus essential to avoid adverse effects on mechanical performance.

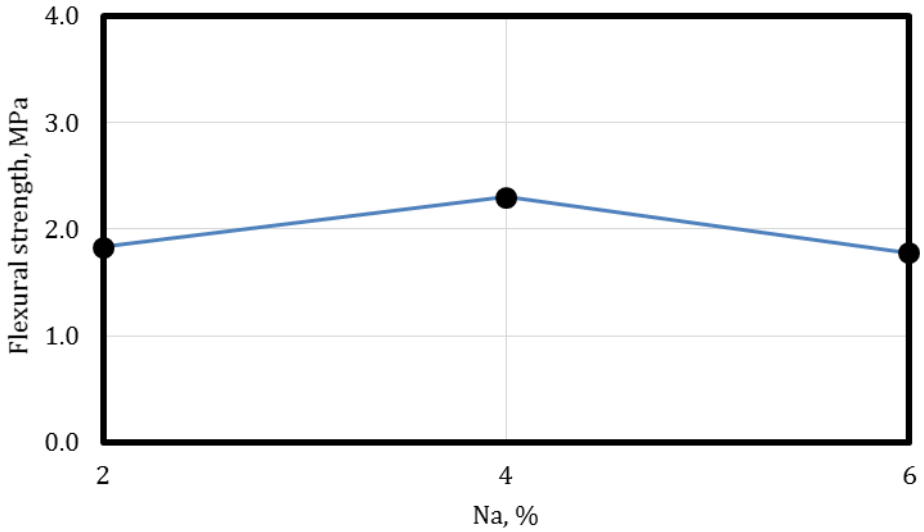

Fig. 4. Flexural strength values of geopolymer specimens.

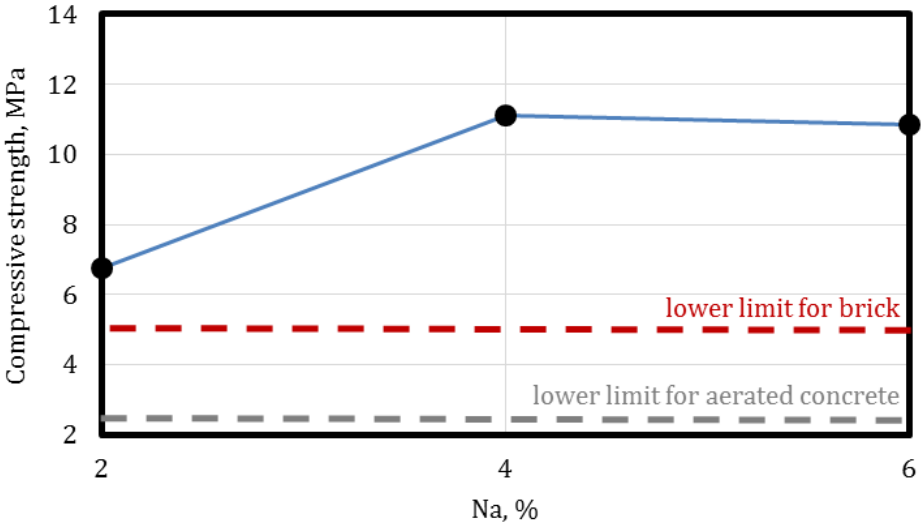

Fig. 5. Compressive strength values of geopolymer specimens.

Splitting tensile strength results reveal a distinct influence of sodium hydroxide on the tensile properties of geopolymer mortars in Fig. 6. At 2% sodium, the splitting tensile strength was 0.61 MPa, increasing by approximately 25.7% to 0.767 MPa at 4% sodium. This enhancement reflects improved gel formation and structural integrity due to increased sodium content. However, at 6% sodium, the strength dropped to 0.592 MPa, showing a 22.8% decrease compared to the 4% mixture. This reduction suggests that excessive alkali content can cause microcracking and poor bonding, negatively impacting internal structure. The results indicate that 4% sodium content represents the optimum level for tensile strength. Lower contents result in insufficient activation, while higher levels disrupt structural integrity. Therefore, optimizing alkali content is critical in geopolymer systems to achieve desirable mechanical performance.

Fig. 7 presents the internal structure images and elemental analyses of the geopolymer samples. In the analyses conducted using a scanning electron microscope (SEM), the internal structure and elemental distribution of the geopolymer produced from fine glass powder and sodium hydroxide solution were examined in detail. The SEM images revealed that the glass powder particles reacted with the sodium hydroxide solution to form a binding matrix. At lower magnifications (250X and 500X), the formation of pores on the surface and the binding phase were observed, while at higher magnifications (1000X and 5000X), amorphous phases within the matrix and unreacted glass particles were detected. Elemental analysis confirmed that the matrix contained sodium-aluminum-silicate-hydrate (N-A-S-H) phases, which are characteristic of geopolymers. It was determined that silicon, aluminum, and sodium were homogeneously distributed across the surface, indicating the formation of the binding phase. Additionally, the presence of a small amount of calcium was found to contribute to the stability of the matrix. These findings suggest that the binding phase within the internal structure of the geopolymers is optimized in terms of both chemical and microstructural strength. However, a more homogeneous structure could be achieved by reducing porosity and the amount of unreacted particles.

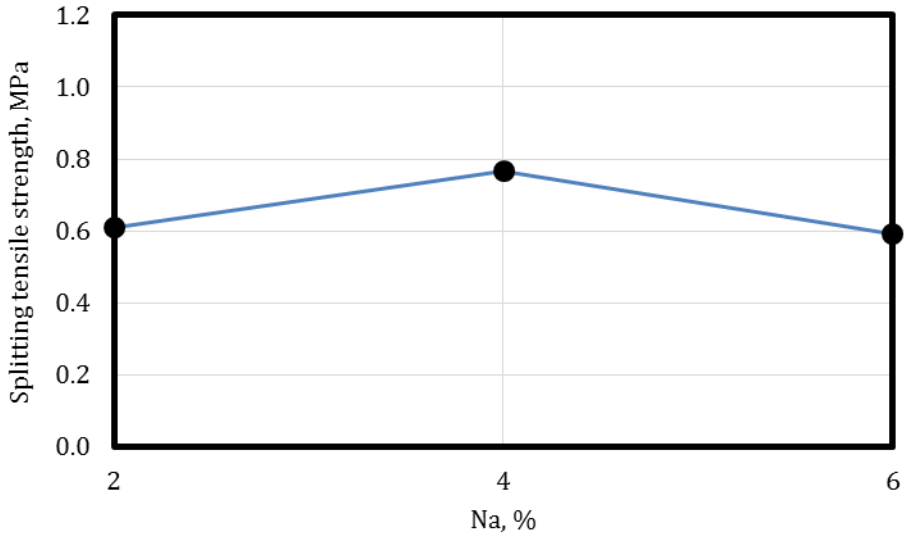

Fig. 6. Splitting tensile strength values of geopolymer specimens.

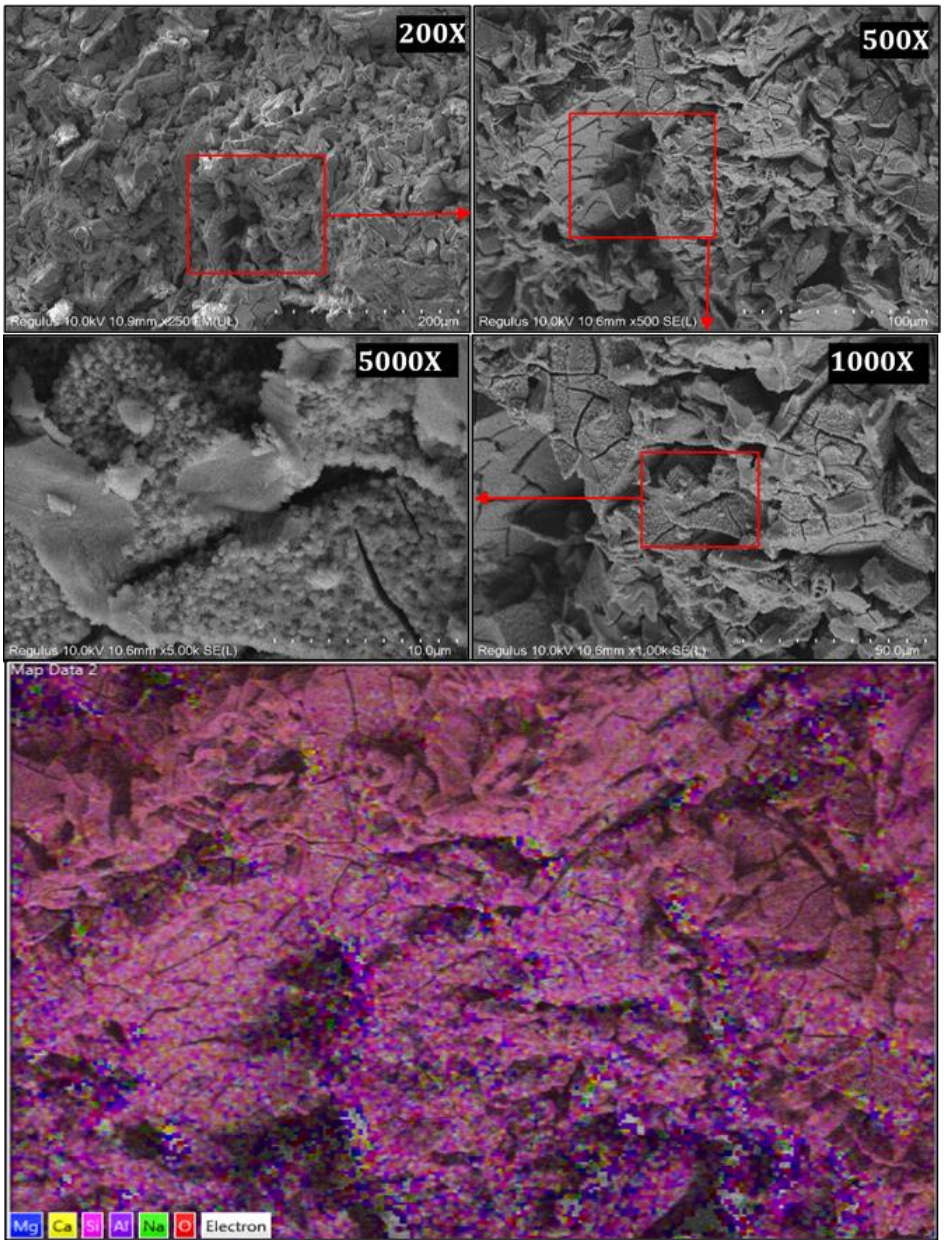

Fig. 7. Microstructure and elemental analysis of geopolymer formed with fine glass powder.

4. Conclusions

This study demonstrated that geopolymer building materials can be successfully produced using only waste glass powder and sodium hydroxide, without the need for traditional cement. The experimental results revealed that the sodium hydroxide content plays a crucial role in determining the physical and mechanical performance of the geopolymer matrix. Among the three tested activator ratios (2%, 4%, and 6%), the mixture containing 4% sodium hydroxide exhibited the most favorable properties in terms of unit weight, ultrasonic pulse velocity, and strength values. Specifically, this mixture achieved a denser internal structure, higher ultrasonic pulse velocity, and superior mechanical strength, including compressive, flexural, and tensile strengths. These enhancements are attributed to the effective activation of the silica-rich glass powder and the optimal formation of binding gels at this concentration.

On the other hand, increasing the sodium hydroxide content to 6% resulted in a decline in performance, indicating that excessive alkali levels may disrupt the geopolymerization process by increasing porosity and microcracking within the matrix. Microstructural analyses conducted via SEM and energy dispersive x-ray spectroscopy (EDS) further supported these findings by confirming the formation of sodium-alumino-silicate-hydrate (N-A-S-H) gels and identifying a homogenous distribution of key elements, including silicon, aluminum, and sodium, in addition to a minor presence of calcium that contributed to matrix stability. These observations validate the chemical and structural soundness of the material at the optimum sodium hydroxide level. In conclusion, the use of 4% sodium hydroxide is recommended to obtain the best mechanical and physical properties.

Ultimately, the glass powder-based geopolymer developed in this study presents a lightweight, durable, and environmentally responsible alternative to conventional construction materials. With physical and mechanical properties close to those of brick and superior to aerated concrete, the material holds significant promise for practical applications in non-load-bearing and insulating building components. Moreover, the valorization of waste glass in this context contributes to circular economy goals and aids in reducing the carbon footprint associated with cement production. Thus, this research provides a viable and scalable approach for integrating industrial glass waste into sustainable construction practices. Future studies should explore the long-term durability, microstructural development, and large-scale application potential of waste glass powder-based geopolymers under various environmental conditions.

Acknowledgements

None declared.

Funding

The authors received no financial support for the research, authorship, and/or publication of this manuscript.

Conflict of Interest

The authors declare no potential conflicts of interest with respect to the research, authorship, and/or publication of this manuscript.

Data Availability

The datasets generated and/or analyzed during the current study are not publicly available but are available from the corresponding author upon reasonable request.

AI Assistance

No AI-based tools were used in the preparation of this manuscript.

Author Contributions

All authors made substantial contributions to the conception and design of the study, acquisition of data, analysis and interpretation of data; drafted or critically revised the manuscript for important intellectual content; and approved the final version to be published.

References

Almakrab A, Elshazli MT, Ibrahim A, Khalifa YA (2024). Assessment of various mitigation strategies of alkali-silica reactions in concrete using accelerated mortar test. *Materials*, 17(20), 5124.

Amin M, Zeyad AM, Agwa IS, Rizk MS (2024). Effect of industrial wastes on the properties of sustainable ultra-high-performance concrete: Ganite, ceramic, and glass. *Construction and Building Materials*, 428, 136292.

Asokan P, Osmani M, Price AD (2010). Improvement of the mechanical properties of glass fibre reinforced plastic waste powder filled concrete. *Construction and Building Materials*, 24(4), 448-460.

Barbhuiya S, Kanavaris F, Ashish DK, Tu W, Das BB, Adak D (2025). Ground waste glass as a supplementary cementitious material for concrete: sustainable utilization, material performance and environmental considerations. *Journal of Sustainable Cement-Based Materials*, 14(7), 1221–1249.

Bulut H (2024). A different approach for green concrete production: Determination of the effect of e-waste and waste rubber powder on durability properties of concrete. *Challenge Journal of Concrete Research Letters*, 15(3), 69-81.

Charef R, Lu W, Hall D (2022). The transition to the circular economy of the construction industry: Insights into sustainable approaches to improve the understanding. *Journal of Cleaner Production*, 364, 132421.

Çelik Z, Turan E, Oltulu M, Öner G (2024). Reinforcement of concrete beams using waste carbon-nanoclay-fiberglass laminate pieces. *Challenge Journal of Concrete Research Letters*, 15(1), 1-6.

Davidovits J (2015). False values on CO_2 emission for geopolymer cement/concrete published in scientific papers. *Technical Paper #24, Geopolymer Institute Library,* www.geopolymer.org.

Gao Z, Li Y, Qian H, Wei M (2023). Environmental, economic, and social sustainability assessment: A case of using contaminated tailings stabilized by waste-based geopolymer as road base. *Science of the Total Environment*, 888, 164092.

Hegyi A, Lăzărescu AV, Ciobanu AA, Ionescu BA, Grebenişan E, Chira M, Stoian V (2023). Study on the possibilities of developing cementitious or geopolymer composite materials with specific performances by exploiting the photocatalytic properties of TiO_2 nanoparticles. *Materials*, 16(10), 3741.

Huovila A, Siikavirta H, Rozado CA, Rökman J, Tuominen P, Paiho S, Ylén P. (2022). Carbon-neutral cities: Critical review of theory and practice. *Journal of Cleaner Production*, 341, 130912.

Imbabi MS, Carrigan C, McKenna S (2012). Trends and developments in green cement and concrete technology. *International Journal of Sustainable Built Environment*, 1(2), 194-216.

Kriven WM, Leonelli C, Provis JL, Boccaccini AR, Attwell C, Ducman VS, Lombardi JE (2024). Why geopolymers and alkali-activated materi-

als are key components of a sustainable world: A perspective contribution. *Journal of the American Ceramic Society*, 107(8), 5159-5177.

Lai Z, Chen Y (2024). Enhancing the mechanical and environmental performance of solidified soil using construction waste and glass micro-powder. *Heliyon*, 10(22), e40187.

Lam WL, Cai Y, Sun K, Shen P, Poon CS (2024). Roles of ultra-fine waste glass powder in early hydration of Portland cement: Hydration kinetics, mechanical performance, and microstructure. *Construction and Building Materials*, 415, 135042.

Luhar S, Cheng TW, Nicolaides D, Luhar I, Panias D, Sakkas K (2019). Valorisation of glass wastes for the development of geopolymer composites–Durability, thermal and microstructural properties: A review. *Construction and Building Materials*, 222, 673-687.

Manjunath R, Narasimhan MC (2020). Alkali-activated concrete systems: A state of art. *New Materials in Civil Engineering*, 2020, 459-491.

Nasir M, Mahmood AH, Bahraq AA (2024). History, recent progress, and future challenges of alkali-activated binders–An overview. *Construction and Building Materials*, 426, 136141.

Sbahieh S, McKay G, Al-Ghamdi SG (2023). Comprehensive analysis of geopolymer materials: Properties, environmental impacts, and applications. *Materials*, 16(23), 7363.

Siddika A, Hajimohammadi A, Ferdous W, Sahajwalla V (2021). Roles of waste glass and the effect of process parameters on the properties of sustainable cement and geopolymer concrete—a state-of-the-art review. *Polymers*, 13(22), 3935.

Ślosarczyk A, Fořt J, Klapiszewska I, Thomas M, Klapiszewski Ł, Černý R (2023). A literature review of the latest trends and perspectives regarding alkali-activated materials in terms of sustainable development. *Journal of Materials Research and Technology*, 25, 5394-5425.

Ünal S, Canbaz M (2025). Utilization of expired cement and aged roof tile powder in the production of sustainable geopolymer: Mechanical and physical properties. *Challenge Journal of Structural Mechanics*, 11(2), 82-88.

Zhang S (2015). Waste glass as partial binder precursor and fine aggregate replacement in alkali activated slag/fly ash system. *Cement and Concrete Research*, 102, 29-40.

Challenge Journal of STRUCTURAL MECHANICS

Research Article

Structural performance analysis of steel piled offshore platforms under environmental loads

Mahir Aliyev [a], Fethi Şermet [a,*], Rüstem Gül [a]

[a] *Department of Civil Engineering, Iğdır University, 76000 Iğdır, Türkiye*

ABSTRACT

Steel pile foundations used in offshore structures must be able to maintain their structural integrity and safety throughout the structure's service life under environmental effects such as waves, currents, and wind. In this context, this study conducts a detailed investigation of the structural performance of a steel-piled offshore platform under environmental wave loads with different return periods. Within the scope of the analysis, the behavior of a typical platform pile group was modeled and analyzed using the Sesam Genie software under wave loads with 1-year (operating), 100-year (extreme), and 10,000-year (abnormal) return periods, considering four different soil units (ZU1, ZU2, ZU3, and ZU4). The analysis determined the maximum internal forces acting on the piles (axial forces, lateral forces, and moments) as well as the maximum displacement values at the pile tips, which ranged between 0.012 m and 0.054 m depending on the load direction and return period. Furthermore, the maximum utilization factor (UF) for each pile was calculated, varying between 0.22 and 0.49, and compared against the minimum safety factors specified in the ISO 19902 standard. It was found that in all scenarios, the maximum utilization factors of the piles remained below the respective safety limits, and the horizontal displacements at the pile tips were within acceptable engineering levels. Unlike many previous studies focusing on single piles, this study systematically evaluates group pile behavior in layered soil conditions, providing more realistic insights into offshore foundation performance. In conclusion, this study highlights the importance of concurrently evaluating soil properties and environmental loads for the structural safety of steel pile foundations and contributes to the multifaceted engineering parameters that must be considered during the design phase.

ARTICLE INFO

Article history:
Received – July 7, 2025
Revision requested – August 22, 2025
Revision received – September 26, 2025
Accepted – October 7, 2025

Keywords:
Soil-structure interaction
Pile foundation
Dynamic loading
Hybrid soil model
Offshore structure

Citation: Aliyev M, Şermet F, Gül R (2026). Structural performance analysis of steel piled offshore platforms under environmental loads. *Challenge Journal of Structural Mechanics*, 12(1), 30–44.

1. Introduction

The design and performance of pile foundations are of fundamental importance for the stability and integrity of offshore structures, especially under harsh environmental conditions. Such structures are subjected to dynamic forces resulting from waves, wind, and seismic activity, making it critical to accurately understand the interaction between pile foundations and the surrounding soil. Among the various factors influencing pile behavior, soil properties and composition play a decisive role. Soil types directly affect load transfer mechanisms, pile deformations, and the overall stability of the foundation under both vertical and lateral loading.

Pile foundations in offshore structures, as well as in many onshore civil engineering applications, are exposed to cyclic loading. These loads typically originate from sources such as waves, wind, traffic, and seismic effects. Under cyclic loading, the load-bearing capacity, stiffness, and soil–pile interaction may change over time.

* *Corresponding author*. E-mail address: fethi.sermet@igdir.edu.tr (F. Şermet)
ISSN: 2149-8024 / DOI: https://doi.org/10.20528/cjsmec.2026.01.003

Andersen (2015) presented key parameters related to cyclic soil behavior, which are critical for the design of offshore foundations. Randolph and Gourvenec (2011) emphasized geotechnical engineering principles for offshore environments, forming a basis for the assessment of cyclic loading. LeBlanc et al. (2010) investigated the degradation tendencies in stiffness and capacity under long-term cyclic lateral loading of piles in sandy soils. Seidel and Coronel (2011) proposed a novel approach for evaluating axial cyclic loading on offshore piles, offering practical contributions to design methods. Basack and Banerjee (2014) experimentally studied lateral cyclic responses in layered soils, providing critical insights into pile–soil interaction. Similarly, Liu et al. (2019) numerically examined the dynamic responses of open-ended offshore piles under lateral cyclic loading and validated the findings with field data. Achmus et al. (2009) detailed the behavior of monopile foundations under cyclic lateral loading, highlighting the influence of soil properties and pile stiffness on performance. Buckley et al. (2023) contributed to offshore pile design principles through large-scale pile testing.

Although these studies provide valuable insights, most of them focus either on sandy soils or simplified single-layer soil conditions. Limited attention has been given to heterogeneous soil profiles that typically exist in offshore environments, and the combined influence of cyclic loading and layered soil properties is not fully captured.

Offshore structures are engineering systems that are continuously exposed to dynamic forces such as waves, wind, currents, and seismic loads (Yigit et al. 2018, Şermet et al. 2022). The long-term stability and durability of these structures depend on the accurate analysis of soil–structure interaction (Hacıefendioglu and Birinci 2015). Numerous studies have been conducted on this subject. Memarpour et al. (2012) investigated the cyclic lateral load response of pile foundations in offshore platforms using numerical methods. Cairo et al. (2005) examined interaction factors for pile groups in layered soils, providing insights into group effects. Sun et al. (2024) numerically analyzed stability under extreme environmental conditions and proposed design recommendations for wind energy applications. Chen et al. (2014) studied pile settlement in mixed soils and highlighted time-dependent variations in load-bearing capacity. Xu et al. (2021) analyzed dynamic stability under wave loading and offered practical design implications for offshore infrastructure. Ashour et al. (2004) explored the lateral behavior of pile groups in layered soils, emphasizing load sharing and group interactions. Basack et al. (2022) expanded the field by analyzing pile–soil interaction under cyclic loading in loose sands through both experimental and numerical approaches. Karalar et al. (2024) simulated the nonlinear behavior of soil type on structures. They stated that soil type significantly affects the behavior of the structure.

However, most of these studies emphasize lateral load behavior or settlement, while only a few explicitly incorporate both vertical and lateral responses under extreme cyclic loading. In addition, the consideration of return period–based wave loading (e.g., 1-year, 100-year, and 10,000-year scenarios) remains largely absent in existing research.

To provide a clear understanding of the research scope and methodology, this study systematically analyzes the vertical and lateral behavior of steel pile foundations under four different soil types (ZU1–ZU4) and three wave loading scenarios corresponding to return periods of 1, 100, and 10,000 years. Pile displacements were evaluated for each loading scenario, and the maximum safety factors of the piles were compared with the ISO 19902 standard. This approach allows a comprehensive assessment of soil–pile interaction under varying environmental conditions.

Piles, which form the foundation system of offshore platforms, are critically important for the stability and safety of the structure. The performance of these systems varies depending on soil conditions, loading scenarios, and environmental factors. In particular, the group pile effect refers to the condition in which multiple piles work together within the same structural system; this interaction can either enhance or reduce the overall load-bearing capacity by influencing the behavior of each individual pile in contact with the soil. This effect can be a determining factor in the platform's durability and long-term performance.

Al-Khazaali and Vanapalli (2019) conducted experimental studies on single piles and pile groups in saturated and unsaturated sandy soils, revealing variations in load-bearing capacity and load distribution. Basack (2014) developed comprehensive design methodologies by integrating field data with analytical approaches. Chandrasekaran et al. (2010) examined lateral cyclic loading in clay soils and proposed empirical correlations for design purposes. Horsnell et al. (1990) investigated the lateral behavior of pile groups in marine soils, producing findings that remain relevant today. Tedesco (2013) analyzed the numerical responses of single piles and pile groups in soft clay soils, exploring their interaction with lattice structures. Wang et al. (2024) studied the lateral performance of pile-supported wharves under cyclic loading using quasi-static model tests. It has been found that displacement accumulation is closely related to load amplitude and the number of loading cycles. Duan et al. (2024) conducted model tests to understand how cyclic lateral loads affect pile–soil interaction, identifying progressive failure modes and a reduction in stiffness. Qin et al. (2024) investigated the lateral resistance behavior of piles in sandy soils, demonstrating that stiffness initially increases but decreases with continued cycling due to soil loosening. Sallam et al. (2024) examined the response of piles subjected to simultaneous lateral and torsional loading, observing reductions in both capacity and stiffness, particularly in sandy soils. Thangavel and Rathod (2024) studied the behavior of rigid piles under unidirectional cyclic loading, showing an initial increase in stiffness followed by increased displacements with further cycles. Krishnanunni and Rathod (2024) tested the behavior of piles under lateral loads on sloped ground, reporting that the best performance was achieved when piles were placed at a distance of two diameters from the crest, though load eccentricity was found to reduce lateral resistance. Anasta-

sopoulos and Theofilou (2016) compared hybrid foundations with monopile systems under environmental and seismic loading, showing that hybrid systems reduce rotational accumulation and offer improved overall performance. Chen et al. (2023) developed an analytical method to evaluate the behavior of offshore pipe piles under S-wave loading, revealing that hydrodynamic pressure has a significant influence on vibration and deformation responses. Hu et al. (2023) conducted full-scale tests on grouted large-diameter piles and demonstrated that grouting enhances load-bearing capacity, with greater effectiveness observed in coarse-grained soils. Xu et al. (2020) assessed the lateral performance of offshore piles through field tests using fiber optic sensors and proposed a modified p–y method that better fits the observed displacement and moment data. Dai et al. (2023) analyzed semi-rigid piles in cement-improved clay under both monotonic and cyclic loading, showing that soil improvement significantly reduces displacements and stiffness degradation, and that numerical models can effectively support design optimization.

Although these studies highlight group effects, soil improvement, and innovative design methods, there is still a lack of systematic comparison between different soil types and their influence on both vertical and lateral pile responses. In particular, the combined evaluation of soil heterogeneity and long-term wave loading scenarios is rarely explored.

In offshore engineering projects, a wide range of soil types- from soft clays to dense sands- are encountered, each presenting unique challenges. Soft soils are typically associated with excessive settlement and lateral displacement, whereas stiff soils, while offering higher load-bearing capacity, can lead to larger bending moments and increased structural stresses. However, hybrid soil profiles containing both soft and stiff layers have the potential to offer cost-effective solutions without compromising performance. Despite growing awareness of the significance of soil properties, there remains a need for detailed investigations into the performance of pile foundations under varying soil conditions and loading scenarios.

In summary, the literature demonstrates considerable progress in understanding cyclic loading, group effects, and soil–pile interaction. Nevertheless, four critical gaps remain: (i) limited integration of heterogeneous soil profiles in analyses, (ii) insufficient consideration of return period–based wave loading, (iii) almost no investigations into abnormal loading conditions associated with very rare events such as 10,000-year return periods, and (iv) lack of comparative evaluations aligned with international design standards such as ISO 19902.

Unlike earlier research that focused mainly on single piles, the novelty of this work lies in its integrated assessment of group piles, layered soil units (ZU1–ZU4), and wave loads with multiple return periods.

The primary objective of the study is to highlight the soil–pile interaction under various environmental loading conditions and provide valuable data to support the safe design of offshore pile foundations.

In this context, the main objectives of the study are as follows:

- To analyze the behavior of piles under different wave loading scenarios,
- To perform comparisons based on safety factor approaches in accordance with the ISO 19902 standard,
- To investigate the influence of soil types on pile–soil interaction.

A limitation of this study is that the numerical models have not been directly validated against field or experimental data; however, they are based on site-specific geotechnical parameters and measured environmental conditions (wave and wind data), ensuring a realistic representation of the Caspian Sea region.

2. Materials and Method

2.1. Platform design and structural details

The platform design is optimized for offshore conditions and consists of a lattice-type superstructure supported by a four-legged, slender jacket framework. The foundation system comprises a total of eight main steel piles arranged as 2×4, each having a diameter of 96 inches (2438 mm) and a wall thickness of 60 mm. The penetration depth of these piles is 117 meters. Fig. 1 illustrates the overall structure and design details of the platform.

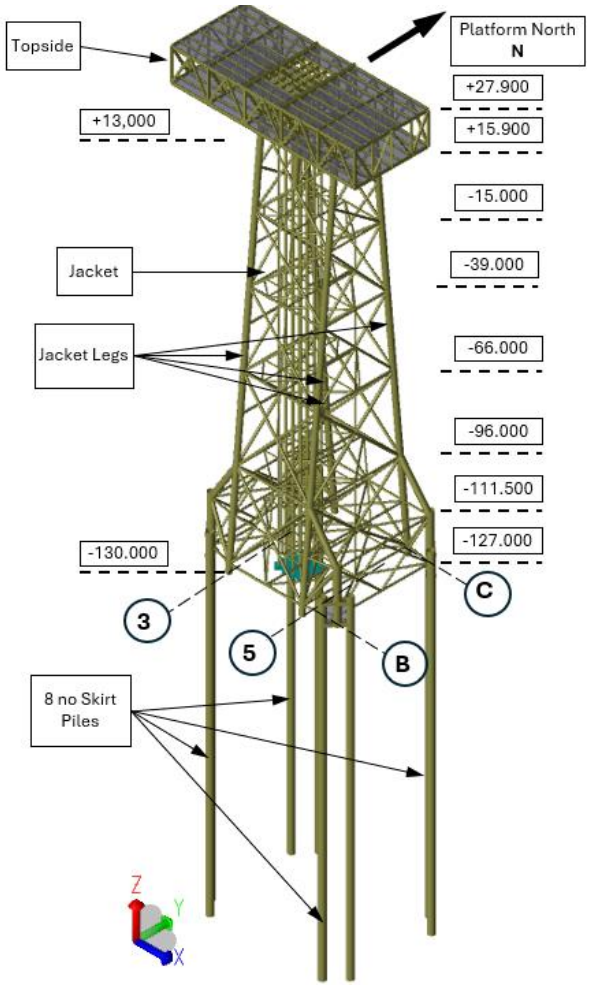

Fig. 1. The view of the modeled platform.

2.1.1. Superstructure geometry

The platform consists of a superstructure housing the Living Quarters (LQ), Modular Drilling Support Modules (MDSM), process area, utility services, wellhead area, and two cranes. Its dimensions are 12 m in height, 28 m in width, and 70 m in length. The 12 m deck height was determined considering structural stiffness and strength (Fig. 2).

The support legs measure 28 m by 15 m and are located at positions B5, C5, B4, C4, B3, and C3. The superstructure consists of two deck levels: the upper deck at elevation +15.9 m and the lower deck at elevation +27.9 m. Primary steel members were modeled with a yield strength of 460 N/mm^2, while secondary members were assigned 355 N/mm^2. Plates were modeled to carry shear forces only; axial stiffness was reduced so that the main lattice girders bear the global loads.

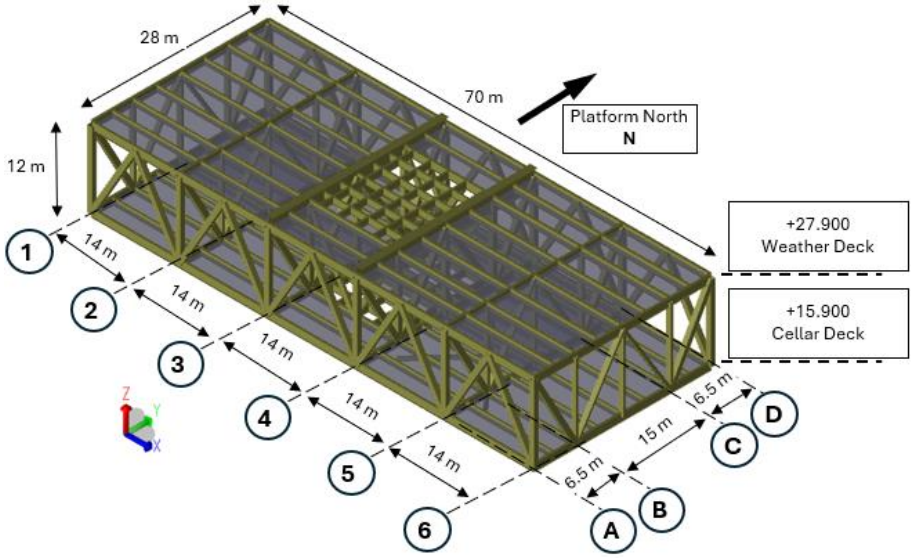

Fig. 2. Modeled superstructure dimensions.

2.1.2. Jacket geometry

The jacket structure is optimized for a water depth of 130 meters. Its top dimensions are 15 m × 28 m, while the base dimensions are 40 m × 48 m (Fig. 3). The superstructure rests on a total of six main legs; the two central legs are shorter than the others, terminating at elevation -1 m at the intersection of the jacket bracing. Inside the jacket, there are 16 conductor pipes, each with an outer diameter of 30 inches. These pipes are arranged at intervals of 2.8 m × 2.6 m and modeled to be self-supporting along the vertical axis. The conductor pipes are laterally stabilized by connections to the jacket members at elevations -15 m, -39 m, -66 m, and -96 m; however, they are not fixed vertically to the jacket structure.

2.1.3. Main skirt pile geometry

In this study, a total of eight steel piles with an outer diameter of 96 inches (2438 mm) and a wall thickness of 60 mm were used. The embedment depth of the piles into the soil is 117 m. The material selected is S460 grade steel; however, in accordance with applicable standards for wall thicknesses between 40 mm and 75 mm, the yield strength was reduced to 415 N/mm^2 (BS EN 10025-2:2019). The total length of each pile is 120 m, with a 3-meter section above the seabed reserved for connection to the jacket structure or the pile sleeve. This length also includes a shear allowance of 0.5 to 1.5 m to accommodate potential damage during pile driving operations (BS EN ISO 19902:2007). Furthermore, the pile length was determined considering field equipment limitations and dynamic effects during installation, ensuring adequate embedment for structural stability and load transfer. The modeled pile geometry is illustrated in Fig. 4.

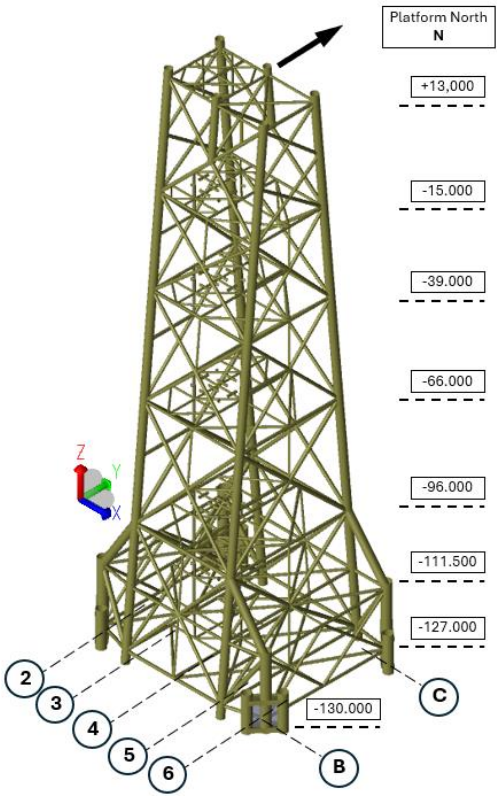

Fig. 3. Modeled jacket dimensions.

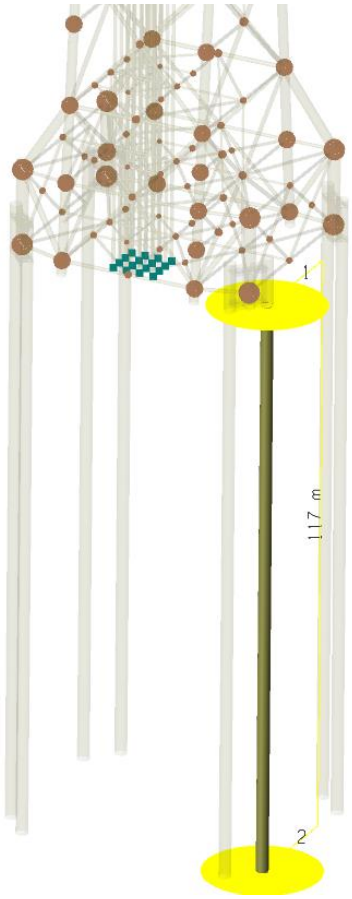

Fig. 4. Modeled pile geometry.

The piles will be driven to the target depth using an underwater hydraulic hammer and fixed to the jacket structure via a grouted pile–sleeve connection (BS EN ISO 19902:2007). Piles located beneath each jacket member are arranged in pairs with a center-to-center spacing of 7.2 m. This configuration aims to minimize soil–pile interaction effects.

The SESAM model also accounts for scour effects caused by marine currents on the seabed. A general scour depth of 2 meters and a local scour depth of 2 meters were defined in the upper soil layer. Temporary installation piles were excluded from this analysis.

2.2. Environmental loads and loading scenarios

This section summarizes the total weights acting on the platform structure. These data are critical for load analyses and structural stability assessments:

- Jacket Weight: The total weight of all components including legs, diagonals, and the base.
- Superstructure Weight: The weight of living quarters, process units, cranes, and other superstructure elements.
- Pile Weight: The total weight of eight steel piles with a diameter of 96 inches, wall thickness of 60 mm, and an embedment depth of 117 m.
- Guide Pipe Weight: The total weight of sixteen guide pipes with a diameter of 30 inches arranged at 2.8 m × 2.6 m spacing.
- Other Weights: Additional loads arising from various equipment and structural components not specified above.

Fig. 5 illustrates the main modules modeled in the system (MDR, DSM, LQ, Wellbay, Process) volumetrically, enabling accurate load distribution and structural interaction modeling.

The total weights of the superstructure, jacket, and piles are presented in Table 1.

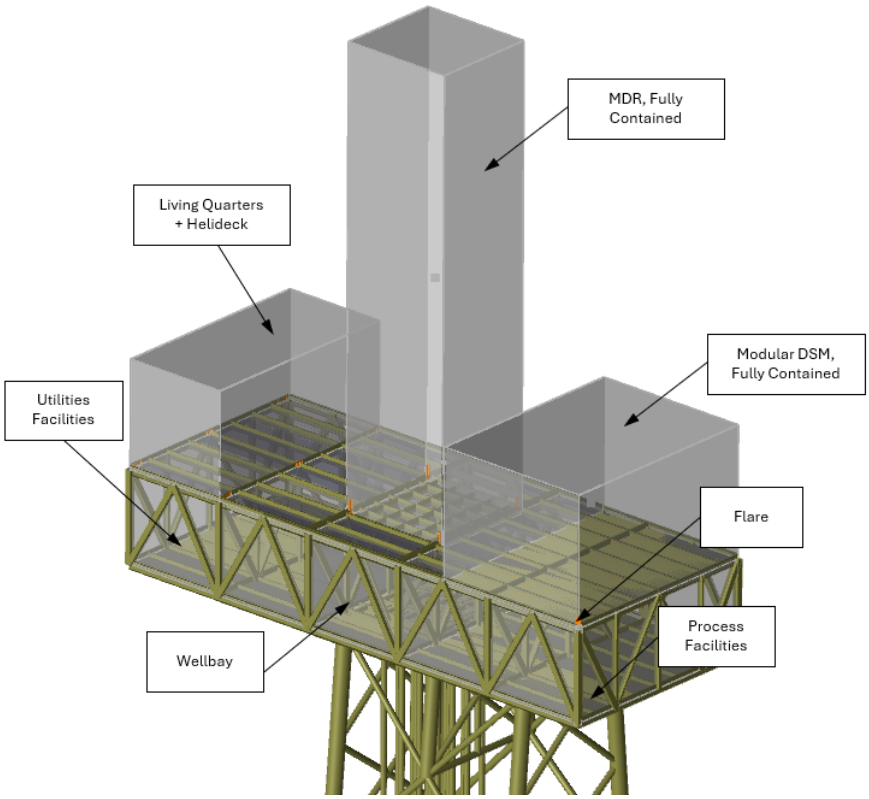

Fig. 5. Applied vertical loads.

Table 1. Total weight summary.

Structure	Self weight (t)	Content weight (t)	Total weight (t) (self weight+ content)
Topside	7638	3719	11357
Jacket	9666	–	9666
Pile	3294	–	3294

Wave and current loads acting on the platform were determined by considering wave height, wave period, current velocity, and flow direction. Using the "WAJAC" module of the SESAM-GeniE software, loads due to waves, wind, and currents were defined for operational (1-year), extreme (100-year), and abnormal (10,000-year) conditions.

A total of 18 different wave approach directions (Fig. 6) were considered, and these directions were transformed based on the positive X-axis reference defined within the "WAJAC" module of SESAM-GeniE.

As an example, wave and current loads for the 320° direction under 1-year, 100-year, and 10,000-year conditions, obtained from analyses performed with SESAM GeniE, are shown in Fig. 7.

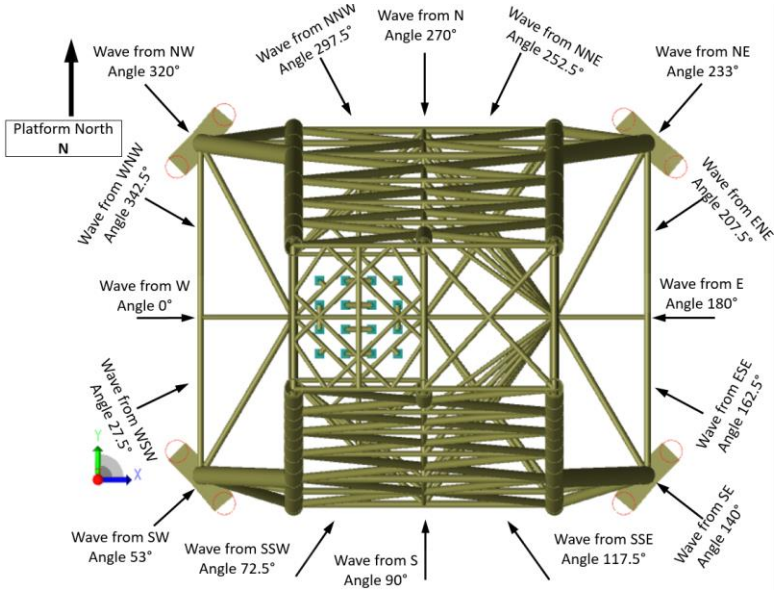

Fig. 6. Wave directions with respect to Sesam axes.

2.3. Analysis method

It should be noted that the 1-year, 100-year, and 10,000-year loading scenarios considered in this study pertain exclusively to the Inplace analysis and account only for dynamic environmental loads, specifically waves and wind, without including seismic effects. In this study, the structural behavior of a steel-piled offshore platform under environmental loading conditions was numerically modeled and analyzed using the Sesam Genie software developed by DNV GL. The analysis incorporated the interaction between the superstructure and pile foundation, soil properties, and various environmental loads.

The following modules were utilized throughout the modeling and analysis process:

- Splice: This module solves the interaction between a linear elastic superstructure and a nonlinear piled foundation. It calculates pile-head displacements and subsequently determines the distribution of internal forces, moments, and displacements along each pile. Advanced features such as pile-soil-pile interaction (group effects), multilayered soil profiles, second-order effects, and incremental loading are supported to enable comprehensive foundation analysis.
- Gensod: Generates nonlinear soil springs based on soil profiles defined within the Genie environment. It models the soil behavior realistically to represent pile-soil interaction accurately.
- Sestra: Performs linear static analysis of the jacket-type superstructure and evaluates global stability. The resulting global stiffness (K) and load (R) matrices are reduced and transferred to the Splice module for foundation analysis.
- Wajac: This module is used to apply wave and current loads. It employs Morison's equation with a nonlinear drag formulation to compute hydrodynamic forces in the time domain. In deterministic wave load analysis, the structure is subjected to unidirectional, periodic waves. At each step, the forces are computed up to the instantaneous water surface. Four wave theories are available for modeling: Airy, Stokes 5th-order, Dean's stream function, and Cnoidal wave theory.

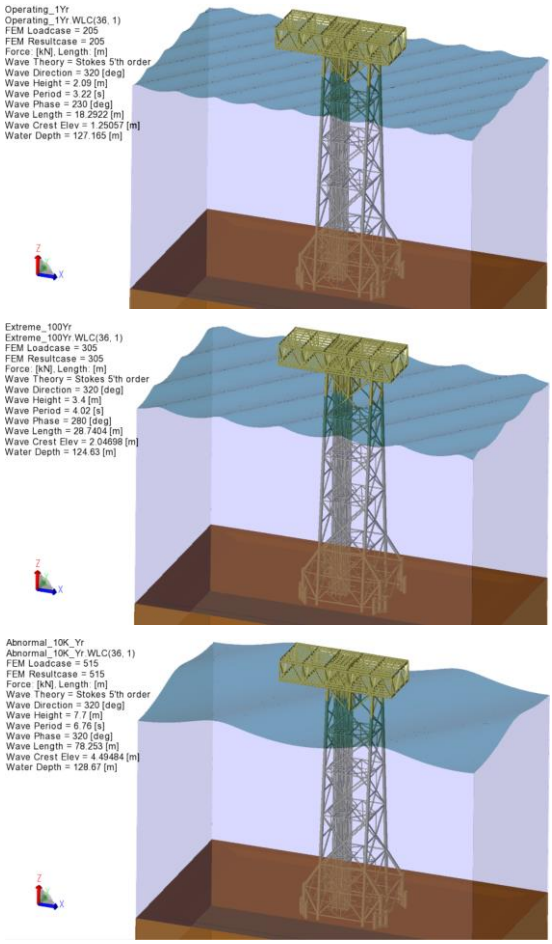

Fig. 7. Wave and current loads at 320° for 1, 100, and 10,000-year conditions.

In this study, Stokes 5th-order wave theory was applied to more accurately capture nonlinear wave effects. In addition, wind loads acting on the exposed jacket elements above the water surface were included using a stationary wind field assumption.

2.4. Soil models

A schematic illustration of the piled foundation system of a "Jacket Type" offshore platform and the soil structure surrounding this foundation is shown in Fig. 8.

The soil parameters (ZU1–ZU4) used in this study were derived from site-specific geotechnical investigations (Geotechnical Report, 2013). These soil units were used in various model combinations to evaluate the performance of pile foundations under coastal conditions. A summary of the soil models is presented in Table 2.

Each soil model includes variations in undrained shear strength, layer depth, and soil behavior under loading conditions (Table 3). The geotechnical parameters were obtained from detailed field investigations conducted in the Caspian Sea and were implemented into the structural models using the Sesam Genie software. These combinations were analyzed to evaluate pile capacity, deformation, and safety factors under operational, extreme, and exceptional loading scenarios.

Table 3 includes fundamental parameters such as depth intervals, unit weights (γ), shear strengths (Su), adhesion coefficients (α), shear stresses (τs), and layer thicknesses (ΔLi). These parameters are critical for understanding the geotechnical properties of each soil unit and for evaluating their effects on pile–soil interaction in the analysis.

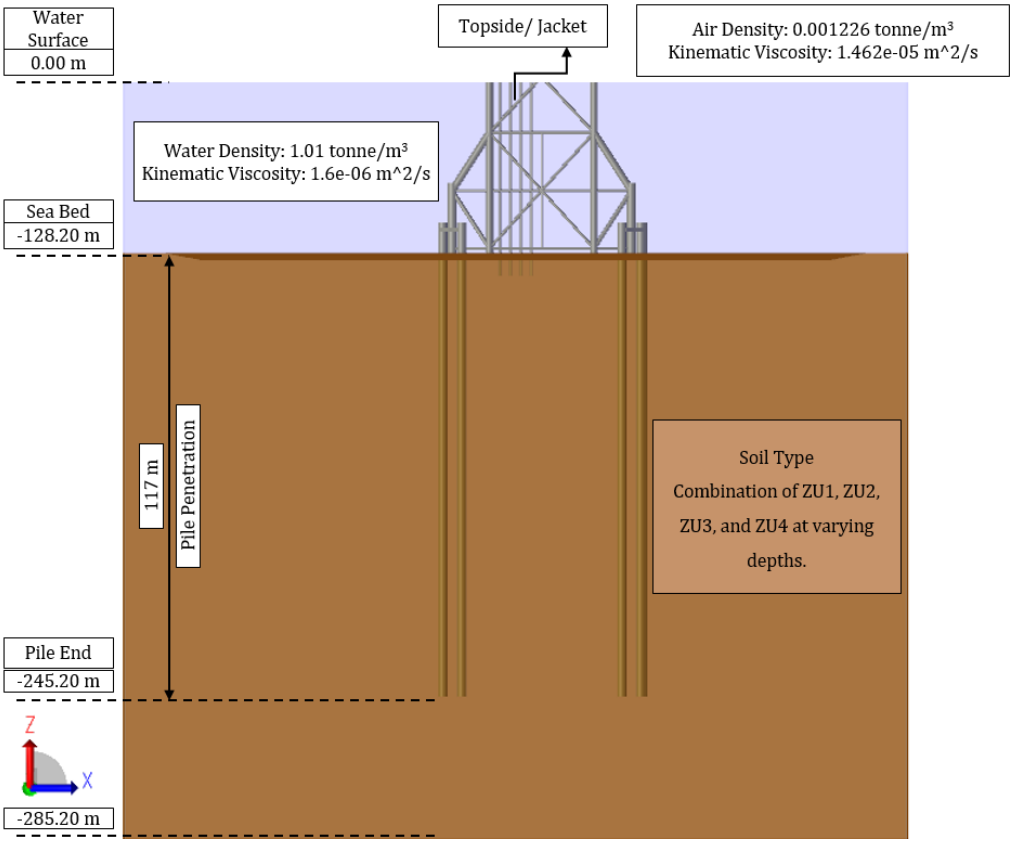

Fig. 8. Soil, water, and air geometry.

Table 2. Soil model units.

Soil unit	Soil type
ZU-1	Calcareous clay, yellowish gray, very soft to soft, with low plasticity, locally containing some shell fragments, organic matter inclusions, and layers of silt and fine sand. Representing soft clay with lower undrained shear strength values, commonly found in upper sedimentary layers.
ZU-2	Clay, greenish to bluish-gray, hard, high plasticity, with a plate and block structure and many slippery surface planes. A transitionary soil type, plastic and slightly stiffer than ZU1, used to simulate intermediate layers
ZU-3	Clay, hard, with a plate/block structure and many slippery surfaces. Medium stiff clay with higher resistance compared to ZU1 and ZU2. Represents more consolidated layers.
ZU-4	Clay, hard, with a plate/block structure and many slippery surfaces. Represents stiff clay with consistent strength and low plasticity index.

Table 3. Soil properties and geotechnical parameters.

Soil unit	Depth range (m)	Unit weight (γ) (kN/m^3)	Shear strength (Su) (kPa)	α	τs (kPa)	ΔLi (m)
ZU1	0 / 42	18.8	10 / 73	0.5/0.28	5.0 / 36.5	42
ZU2	−42 / −90	18.0	101 / 125	0.25	25.3 / 31.3	48
ZU3	−90 / −104	18.0	125 / 132	0.25	31.3 / 33.0	14
ZU4	−104 / −157	18.5	132 / 159	0.25	33.0 / 39.8	53

2.4.1. Soil model combination

In this study, a layered soil profile was created by combining four soil types: ZU1, ZU2, ZU3, and ZU4. Starting with a soft clay layer (ZU1) near the surface and transitioning to stiffer clay layers (ZU4) at greater depths, this configuration represents multi-layered soil conditions. Each layer is defined at different depths, and this approach was used to evaluate how pile–soil interaction varies under changing soil stiffness and strength. Fig. 9 visually presents the layered soil profile by displaying the ZU1–ZU4 soil units in different colors, illustrating their distribution with respect to depth. This visualization facilitates a clearer understanding of the pile–soil interaction.

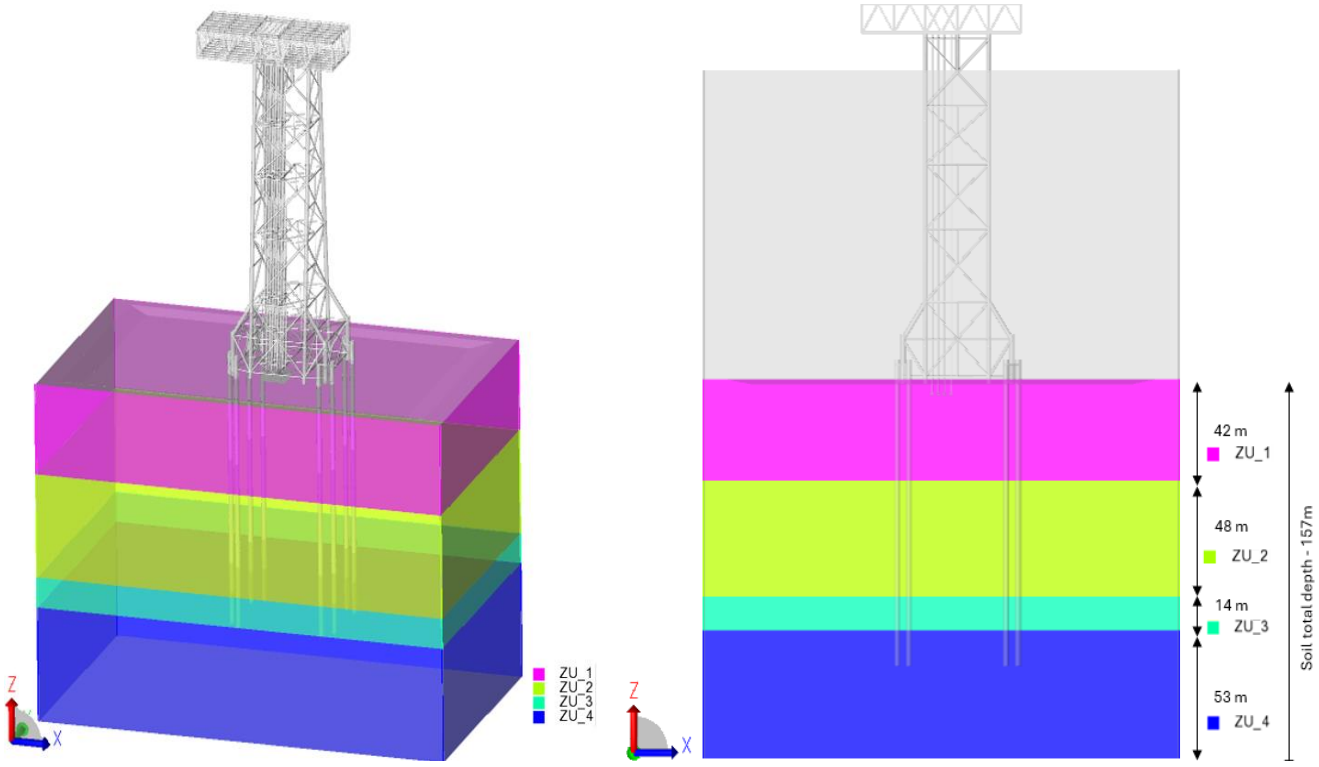

Fig. 9. Soil types and depths.

3. Results and Discussion

Fig. 10 presents the maximum utilization factors (UF) of the pile groups for each individual pile under 1-year, 100-year, and 10,000-year loading conditions. The utilization factor (UF) indicates the ratio of the applied load to the pile capacity; values approaching 1 signify that the capacity limit is nearly reached, while values exceeding UF>1 indicate that the capacity has been exceeded.

Below, code-check results for all pile groups are provided, considering operational (1-year), extreme (100-year), and abnormal (10,000-year) loading scenarios. Additionally, separate result tables are presented for each pile group. The evaluations are based on the most critical loading conditions and have been conducted in accordance with the ISO 19902 (2007).

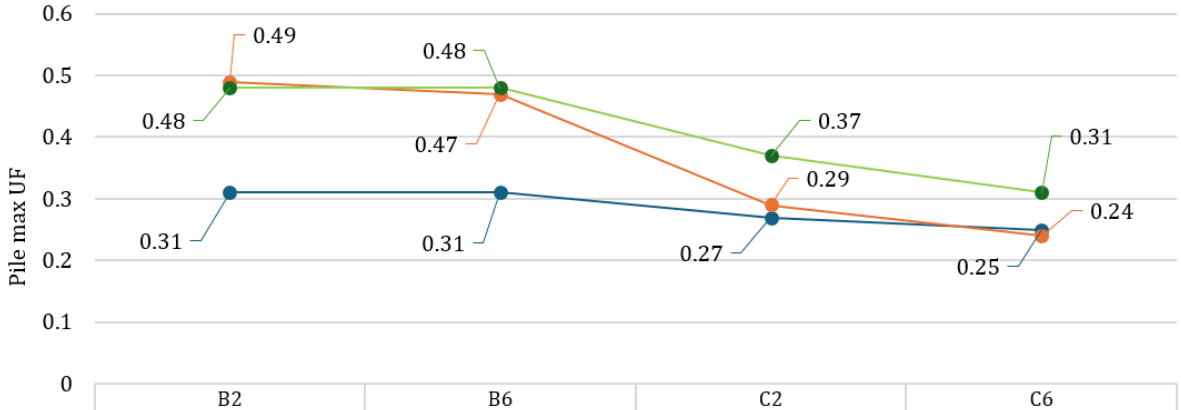

	B2	B6	C2	C6
1yr Operating	0.31	0.31	0.27	0.25
100yr Extreme	0.49	0.47	0.29	0.24
10000yr Abnormal	0.48	0.48	0.37	0.31

Fig. 10. Maximum utilization factors (UF) of pile groups.

In the soil profile dominated by softer soils, pile utilization factors (UF) under lateral loading tend to exhibit relatively higher values. The highest utilization ratios occur under the combined effects of bending moments and lateral forces.

The UF values presented in Table 5 and illustrated in Fig. 11 reveal that pile groups B2 and B6 reach the highest utilization levels, particularly under the 100-year extreme and 10,000-year abnormal loading conditions. For example, Pile_B2_b attains a UF of 0.49 for the 100-year scenario and 0.48 for the 10,000-year scenario. Similarly, the B6 piles show high utilization values in the range of 0.47 to 0.48. These piles, located at the platform corners, are subjected to greater lateral moments and eccentric loads.

Conversely, the central piles in groups C2 and C6 demonstrate lower utilization ratios. For instance, Pile_C6_a exhibits a UF of 0.22 under the 1-year operational load, increasing to 0.30 under the 10,000-year abnormal condition. This indicates that central piles experience less impact from environmental loads and maintain a higher structural capacity reserve.

The most critical utilization factor (UF) values were observed under the 100-year extreme loading scenario rather than the 10,000-year abnormal loading scenario. This is primarily due to the fact that, in the 100-year wave scenario, the wave period and direction are more compatible with the natural frequencies of the structure, resulting in higher lateral responses in certain piles. In contrast, although the wave loads are generally higher in the 10,000-year scenario, the wave period and direction interact less with the structural stiffness, or the loads are more uniformly distributed, leading to lower local stresses in some piles.

This finding highlights that, in structural design, not only the magnitude of the loads but also the load direction, period, and the dynamic behavior of the structure have significant effects on the utilization factors.

3.1. Evaluation of maximum pile force and moment results

According to the results obtained by the SESAM Genie program, maximum tensile (positive) and compressive (negative) forces as well as moment values on the piles are reported for worst loading scenario (1-year operational, 100-year extreme, and 10,000-year abnormal). The force components acting on the piles are classified along the axial (NXX), transverse (NXY), and longitudinal (NXZ) directions; moment components represent rotations about the pile's X, Y, and Z axes (MXX, MXY, MXZ).

Focusing particularly on the NXX component, the highest tensile and compressive forces were observed in piles Pile_C6_b and Pile_B2_b. For example, under the 10,000-year loading scenario, Pile_C6_b experienced a tensile force of +38,397.6 kN and a compressive force of -58,092.8 kN. These values clearly demonstrate the effect of vertical loads (including dead loads and vertical environmental components) on the pile capacities.

Regarding the lateral forces NXY and NXZ, environmental effects such as waves and wind were dominant. Notably, Pile_C2_b carried a high lateral force of +4,839.7 kN in the NXZ direction under the 10,000-year condition. Similarly, Pile_B2_a was subjected to a lateral force of -3,007.4 kN in the transverse direction during the 100-year scenario. These forces vary depending on the orientation and magnitude of wave loads as well as the stiffness distribution of the structure.

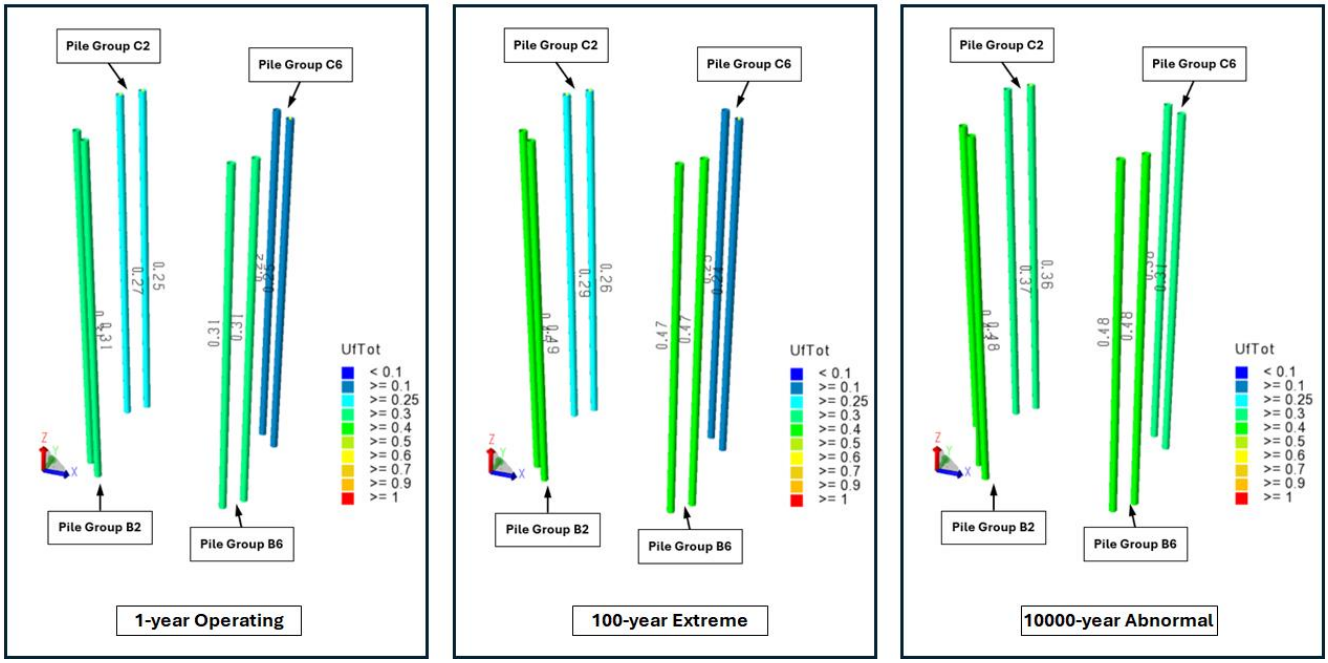

Fig. 11. Maximum utilization factors (UF) plot.

When examining moment components, the largest moments generally occurred at the pile toe and at piles located at corner positions. For instance, Pile_C6_a reached an MXZ moment value of -22,169.2 kN·m under the 10,000-year loading scenario, representing one of the highest moments. Additionally, Pile_C2_b exhibited an MXY moment of +19,862.1 kN·m. Such bending moments are critical parameters that directly influence the pile's stiffness under lateral loads and its anchorage behavior.

When the results are evaluated overall, it is observed that as the load magnitude increases, the forces and moments in the piles also increase. However, in some specific cases, the 100-year extreme loading scenario produces higher lateral forces or moments compared to the 10,000-year scenario. This difference arises from the wave direction and period resonating with the dynamic characteristics of the structure, thereby amplifying the response in certain piles. Particularly, corner piles (such as those in groups B2 and C6) carry greater loads in the rigid system and thus occupy the most critical positions, being subjected to maximum stress.

3.2. Evaluation of pile top displacement results

According to the pile head displacement analysis, limited horizontal and vertical displacements were observed for Pile_B2_a under the 1-year operational loading condition (Figs. 12 and 13). These displacements increased significantly under the 100-year extreme loading scenario, where a resonance-like behavior was observed. This resonance-like behavior is closely related to the interaction between the natural period of the structure and the excitation period of environmental loads. Although the natural period of the present jacket structure was not explicitly calculated in this study, its importance is acknowledged, and future research will aim to provide a detailed dynamic analysis to further clarify this effect. The highest displacement values were obtained under the 10,000-year loading condition. The horizontal and vertical displacements occurring at the pile head with increasing wave loads were evaluated in terms of structural stiffness and considered an important criterion for understanding the system's behavior.

Table 4. Maximum pile head displacements obtained from SESAM Genie program.

Pile name	Load case	DX [m]	DY [m]	DZ [m]
Pile_B2_a	1-Yr Operating	0.036	–	–
Pile_B2_a	1-Yr Operating	–	0.012	–
Pile_B2_a	1-Yr Operating	–	–	0.013
Pile_B2_a	100-Yr Extreme	0.051	–	–
Pile_B2_a	100-Yr Extreme	–	0.020	–
Pile_B2_a	100-Yr Extreme	–	–	0.020
Pile_B2_a	10000-Yr Abnormal	0.054	–	–
Pile_B2_a	10000-Yr Abnormal	–	0.025	–
Pile_B2_a	10000-Yr Abnormal	–	–	0.025

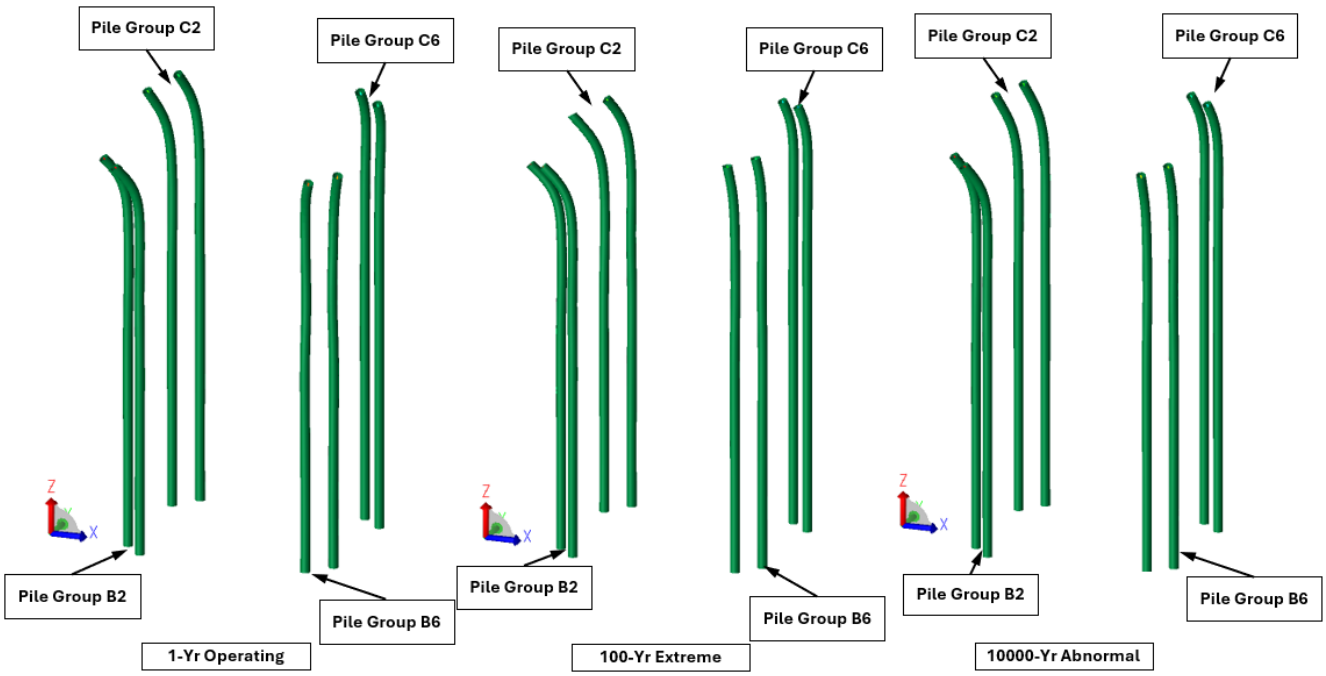

Fig. 12. Maximum displacement visualizations of piles.

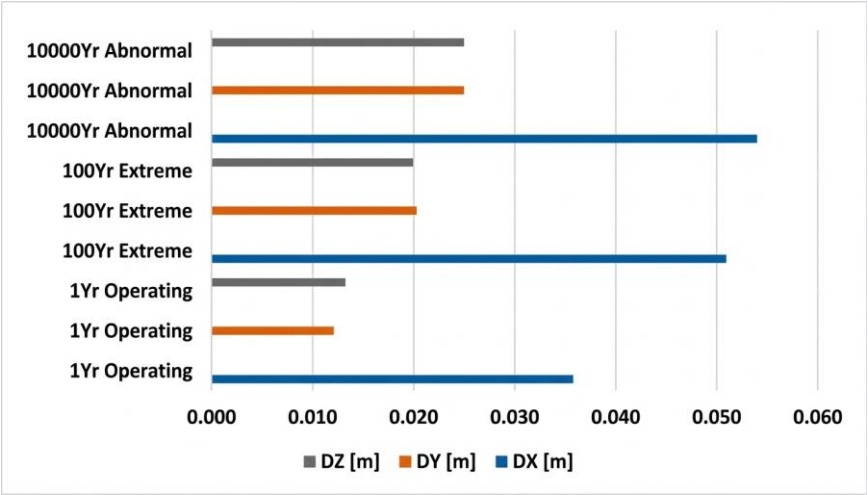

Fig. 13. Maximum displacements (DX, DY, DZ) at the top of Pile_B2_a.

3.3. Evaluation of maximum utilization factors of piles against ISO 19902 safety factors

In this section, the obtained maximum pile utilization factors (UF) are compared with the minimum safety factors specified in the ISO 19902 (2007) standard (Table 5). For each loading condition (1-year operational, 100-year extreme, and 10,000-year abnormal), the UF values were evaluated against the minimum allowable safety factors for the respective analysis cases to assess structural adequacy. This comparison reveals the extent to which the piles approach their design limits and whether the safety criteria for secure design are met.

The maximum pile utilization factors presented in Table 5 remain within safe limits when compared to the minimum safety factors specified in ISO 19902 (2007). Specifically, under the 1-year operational scenario (UF ≤ 0.67), 100-year extreme scenario (UF ≤ 0.80), and 10,000-year abnormal scenario (UF ≤ 1.00), none of the piles exceeded the allowable utilization limits. This indicates that the platform's load-carrying capacity is adequate (Fig. 14).

Figs. 15–17 show the program outputs for the maximum loads experienced by Pile_B2_a, which has the highest utilization factor (UF).

3.4. Evaluation of maximum pile head displacements against ISO 19902 allowable limits

The maximum pile head displacements (DX, DY, and DZ) observed under the 1-year, 100-year, and 10,000-year loading scenarios are summarized in Table 6. The allowable limits are based on ISO 19902 criteria.

All maximum displacements are well below the allowable limits, confirming that the pile foundation system maintains structural adequacy under the considered environmental loading conditions.

3.5. Comparison of utilization factors with literature

To provide context and highlight the novelty of the current study, Table 7 presents a comparison of maximum pile utilization factors (UF) reported in the literature for similar offshore platforms. It should be noted that the numerical results in the present study were obtained using the SESAM model with ZU1–ZU4 soil units, whereas the literature references used different modeling approaches, soil conditions, or experimental setups. Therefore, this comparison serves as a qualitative reference rather than a strict validation.

Table 5. Comparison of Utilization Factors (UF) and ISO minimum safety factors (FoS).

Pile group	Pile name	1 Yr Operating UF	ISO FoS (1/1.5 = 0.67)	1 Yr Extreme UF	ISO FoS (1/1.25 = 0.80)	10.000 Yr Anormal UF	ISO FoS (1/1.0 = 1.00)
B2	Pile_B2_a	0.31	✓ (0.67)	0.45	✓ (0.80)	0.43	✓ (1.00)
	Pile_B2_b	0.31	✓	0.49	✓	0.48	✓
B6	Pile_B6_a	0.31	✓	0.47	✓	0.48	✓
	Pile_B6_b	0.31	✓	0.47	✓	0.48	✓
C2	Pile_C2_a	0.25	✓	0.26	✓	0.36	✓
	Pile_C2_b	0.27	✓	0.29	✓	0.37	✓
C6	Pile_C6_a	0.22	✓	0.23	✓	0.30	✓
	Pile_C6_b	0.25	✓	0.24	✓	0.31	✓

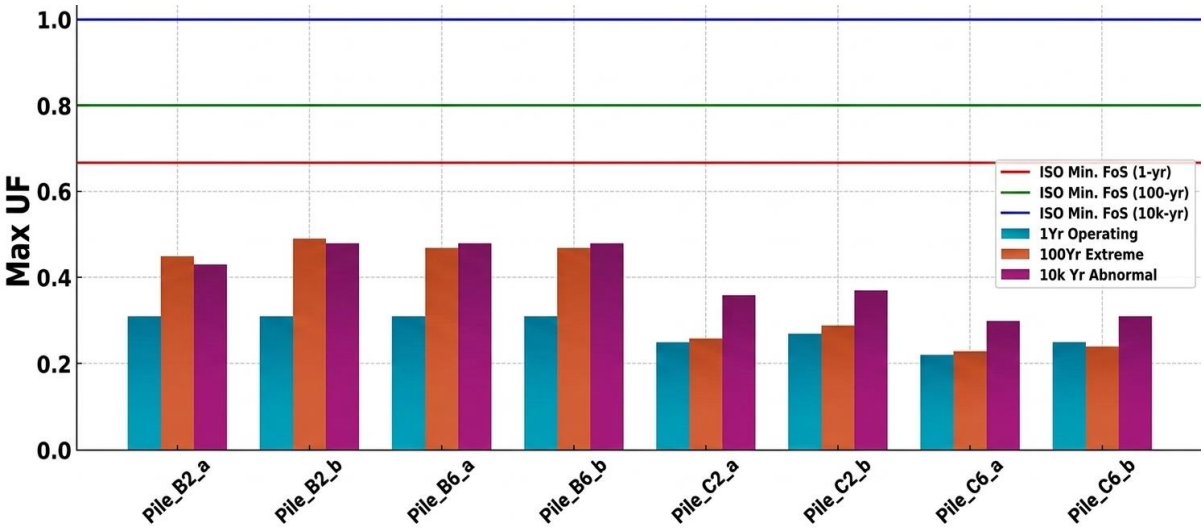

Fig. 14. Comparison of maximum utilization factors (UF) with ISO 19902 minimum FoS.

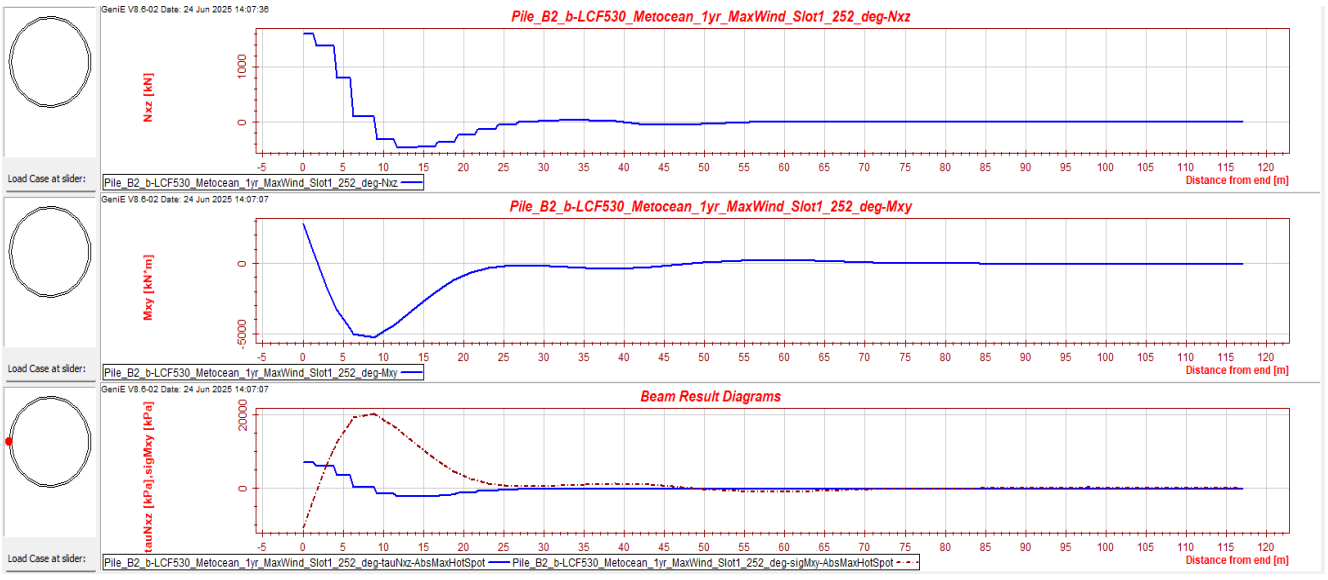

Fig. 15. Pile force outputs for Pile_B2_a under 1-year condition.

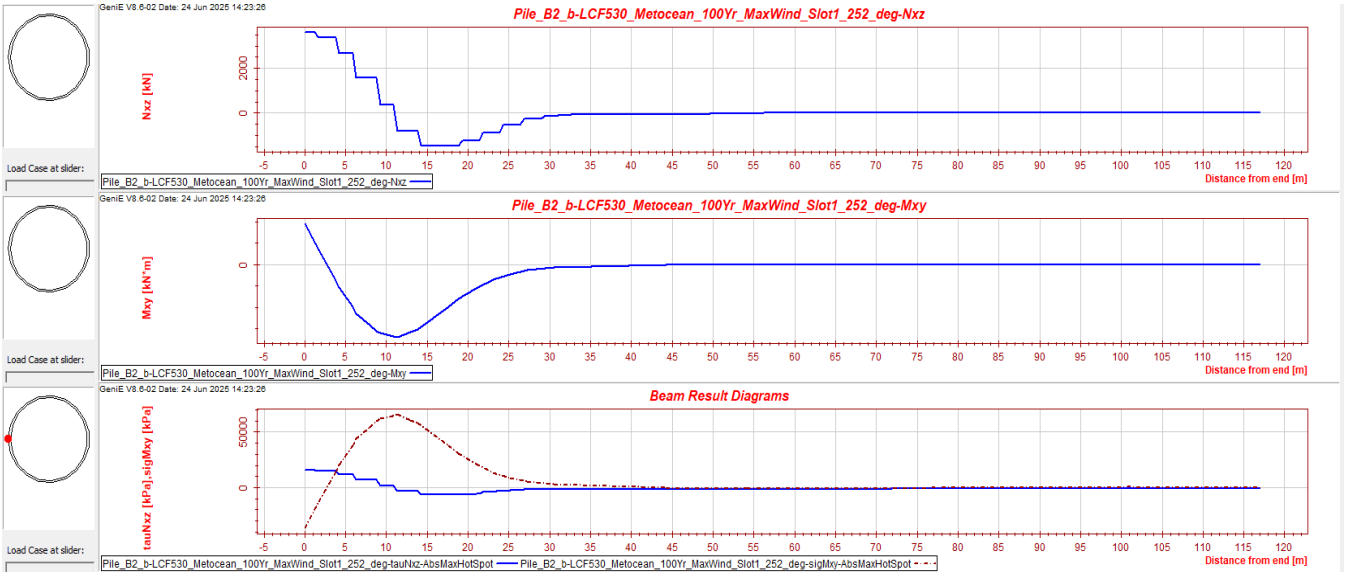

Fig. 16. Pile load outputs for Pile_B2_a under 100-year condition.

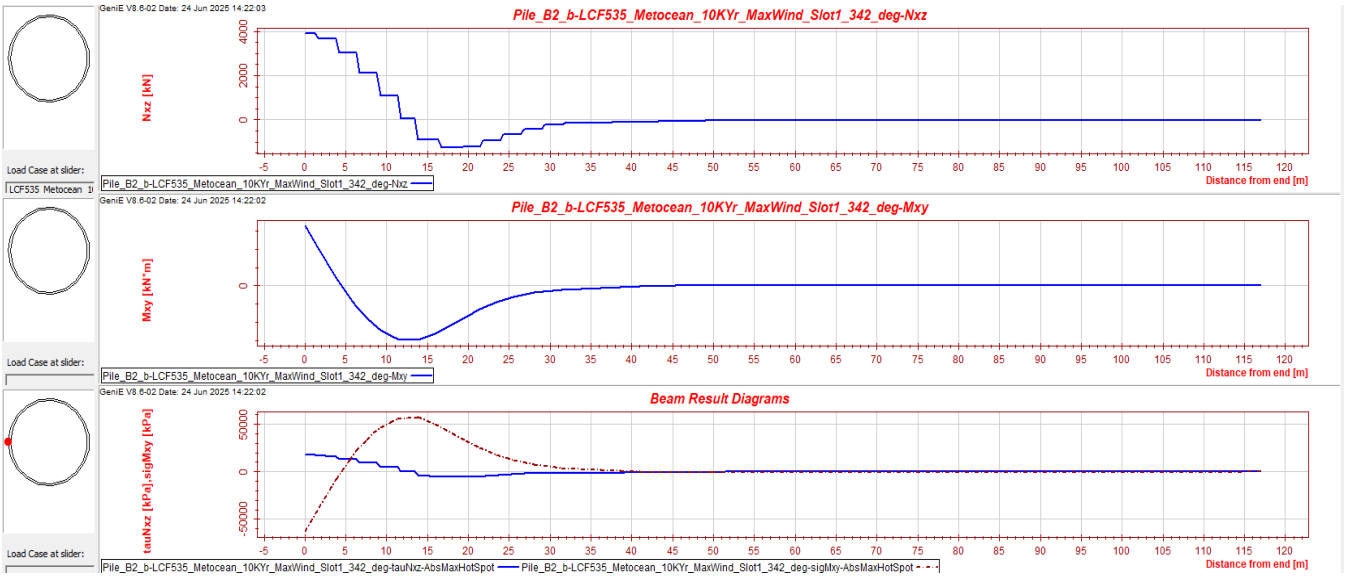

Fig. 17. Pile load outputs for Pile_B2_a under 10,000-year condition.

Table 6. Comparison of maximum pile head displacements against ISO 19902.

Worst pile	DX (m)	DY (m)	DZ (m)	Allowable DX/DY/DZ (m, ISO 19902) L/500	Compliance
Pile_B2_a	0.054	0.025	0.025	0.234 / 0.234 / 0.234	Acceptable

Table 7. Comparison of maximum utilization factors (UF) with literature.

Study / Source	Platform type	Soil type / Conditions	Maximum UF	Notes
Andersen (2015)	Jacket	Sand, layered	0.45	Laboratory and numerical data
LeBlanc et al. (2010)	Jacket	Stiff sand	0.40	Long-term cyclic lateral tests
Basack & Banerjee (2014)	Jacket	Layered soil	0.50	Numerical simulation
Liu et al. (2019)	Monopile	Sand	0.38	Lateral cyclic loadings
Xu et al. (2021)	Jacket	Clay / sand	0.55	Dynamic wave load analysis
This study	Jacket	Hybrid clay	0.49	SESAM model, 1-year / 100-year / 10,000-year loading

The comparison in Table 7 indicates that the maximum pile utilization factors obtained in this study are generally consistent with values reported in the literature for similar offshore platforms. While the literature results include different soil conditions and modeling approaches, the present work uniquely applies ZU1–ZU4 soil units in a detailed SESAM model under operational (1-year), extreme (100-year), and abnormal (10,000-year) wave and wind loading scenarios. Pile displacements are also in the expected range, reaching a maximum of 0.054 m in critical piles. This table therefore provides a qualitative benchmark rather than a direct validation.

3.6. Risk classification of piles based on UF

To provide an application-oriented interpretation of the utilization factor (UF) results, a simple risk classification framework was adopted (Table 8). In this scheme, piles with UF < 0.80 are categorized as Low Risk, UF between 0.80–0.90 as Moderate Risk, and UF > 0.90 as High Risk. This classification is consistent with practical engineering assessments of safety margins.

As shown in Table 8, all maximum UF values obtained in this study fall below 0.80, indicating that the analyzed pile foundations remain within the Low Risk category for all considered scenarios.

Table 8. Risk classification of piles based on utilization factors (UF).

Utilization Factor (UF)	Risk Level
UF < 0.80	Low Risk
0.80 ≤ UF < 0.90	Moderate Risk
UF ≥ 0.90	High Risk

4. Conclusions

This study provides a detailed evaluation of the structural performance of pile foundation systems installed in hybrid soil profiles (ZU1–ZU4) under different environmental loading scenarios. The analyses cover operational (1-year), extreme (100-year), and abnormal (10,000-year) conditions, considering axial and lateral force components (NXX, NXY, NXZ), moment components (MXX, MXY, MXZ), pile head displacements, and utilization factors (UF). The results were compared with the minimum safety factors specified in ISO 19902 (2007) to assess structural adequacy.

The maximum axial forces acting on the piles (NXX) reached approximately 58,100 kN under the 10,000-year scenario, testing the long-term strength reserves of the structure. Lateral force and moment components increased notably in scenarios dominated by wave and wind effects, highlighting the need to assess both axial capacity and lateral stability of pile foundations.

Pile head displacement analyses demonstrated reduced stiffness and increased horizontal displacements with higher loading intensities. For example, at Pile_B2_a, DX, DY, and DZ displacements increased from approximately 0.036 m, 0.012 m, and 0.013 m under the 1-year operational condition to about 0.054 m, 0.025 m, and 0.025 m under the 10,000-year loading condition. This indicates that pile–soil interaction evolves with loading and that structural stiffness control is critical for long-term performance.

Utilization factors remained well below critical limits across all scenarios, confirming that the current pile design maintains significant safety reserves. Corner piles (B2 and B6) experienced the highest UF values due to larger lateral moments, whereas central piles (C2 and C6) maintained lower utilization ratios, preserving structural capacity margins. Notably, some local UF maxima under the 100-year scenario exceeded those of the 10,000-year scenario due to resonance-like interactions between the wave period and the structure's natural frequencies. Although modal analysis was not included in this study, its potential influence is acknowledged and recommended for future investigations.

Overall, the pile geometry safely satisfies ISO 19902 requirements regarding load-carrying capacity and displacement criteria. However, displacement accumulation over long-term loading warrants careful monitoring. Critical areas of the structure should be instrumented to track performance and ensure durability under operational, extreme, and abnormal conditions.

From an engineering and practical standpoint, the significant safety margins identified in this study suggest opportunities for economic optimization. For instance, reducing pile diameter, wall thickness, or the total number of piles could result in cost savings without compromising safety, provided that ISO 19902 compliance is maintained.

For future research, additional aspects such as pile fatigue behavior, long-term soil degradation, scour evolution, and climate change–induced environmental loading should be incorporated. Furthermore, parametric studies involving different pile diameters, configurations, and soil types would enhance the generalizability of the findings and provide deeper insight for offshore foundation design.

5. Recommendations

- Analyze pile behavior under different wave loading scenarios to capture operational, extreme, and abnormal conditions.
- Perform seismic load case analyses to evaluate pile behavior under earthquake effects.
- Compare pile performance across different soil units, such as sandy, clayey, and other hybrid soil layers, to assess the influence of soil type on load-bearing capacity, displacement, and structural response.
- Extend analyses to include varying pile configurations and spacing within the different soil profiles to optimize foundation design.
- From an engineering and practical standpoint, the significant safety margins identified in this study suggest opportunities for design optimization and cost efficiency. For example, reducing pile diameter, thickness, or number of piles could provide economic benefits without compromising structural safety. Future research should further explore these optimization pathways, as well as incorporate aspects such as fatigue, long-term soil degradation, and climate change effects.

Acknowledgements

None declared.

Funding

The authors received no financial support for the research, authorship, and/or publication of this manuscript.

Conflict of Interest

The authors declare no potential conflicts of interest with respect to the research, authorship, and/or publication of this manuscript.

Data Availability

The datasets generated and/or analyzed during the current study are not publicly available but are available from the corresponding author upon reasonable request.

AI Assistance

No AI-based tools were used in the preparation of this manuscript.

Author Contributions

All authors made substantial contributions to the conception and design of the study, acquisition of data, analysis and interpretation of data; drafted or critically revised the manuscript for important intellectual content; and approved the final version to be published.

REFERENCES

Achmus M, Kuo YS, Abdel-Rahman K (2009). Behavior of monopile foundations under cyclic lateral loading. *Journal of Geotechnical and Geoenvironmental Engineering*, 135(3), 430-441.

Al-Khazaali M, Vanapalli SK (2019). Experimental investigation of single model pile and pile group behavior in saturated and unsaturated sand. *Journal of Geotechnical and Geoenvironmental Engineering*, 145(12), 04019112.

Anastasopoulos I, Theofilou M (2016). Hybrid foundation for offshore wind turbines: Environmental and seismic loading. *Soil Dynamics and Earthquake Engineering*, 80, 192-209.

Andersen KH (2015). Cyclic soil parameters for offshore foundation design. *Frontiers in Offshore Geotechnics III*, 5, 5-82.

API RP 2A-WSD (2014). Recommended Practice for Planning, Designing, and Constructing Fixed Offshore Platforms – Working Stress Design. 22nd ed. American Petroleum Institute, Washington, DC, USA.

Ashour M, Pilling P, Norris G (2004). Lateral behavior of pile groups in layered soils. *Journal of Geotechnical and Geoenvironmental Engineering*, 130(6), 580-592.

Basack S (2014). Analysis and design of offshore pile foundation. *Advanced Materials Research*, 891, 17-23.

Basack S, Banerjee AK (2014). Offshore pile foundation subjected to lateral cyclic load in layered soil. *Advanced Materials Research*, 891, 24-29.

Basack S, Karami M, Karakouzian M (2022). Pile-soil interaction under cyclic lateral load in loose sand: Experimental and numerical evaluations. *Soil Dynamics and Earthquake Engineering*, 162, 107439.

BS EN 10025-2:2019 (BSI) (2019). Hot Rolled Products of Structural Steels – Part 2: Technical Delivery Conditions for Non-Alloy Structural Steels. British Standards Institution, London, UK.

BS EN ISO 19902 (2007). Petroleum and Natural Gas Industries – Fixed Steel Offshore Structures. British Standards Institution, London, UK.

Buckley RM, Byrne B, Houlsby GT, McAdam RA (2023). Large-scale pile testing research to advance offshore pile design. *Offshore Site Investigation and Geotechnics: 9th International Conference Proceedings*, 572-594.

Cairo R, Conte E, Dente G (2005). Interaction factors for the analysis of pile groups in layered soils. *Journal of Geotechnical and Geoenvironmental Engineering*, 131(4), 525-528.

Chandrasekaran SS, Boominathan A, Dodagoudar GR (2010). Experimental investigations on the behaviour of pile groups in clay under lateral cyclic loading. *Geotechnical and Geological Engineering*, 28, 603-617.

Chen L, Li J, Wu W, Liu H, Yao Y, Zhang P (2023). New method to calculate the kinematic response of offshore pipe piles under seismic S-waves. *Soil Dynamics and Earthquake Engineering*, 165, 107651.

Chen Q, Zhang H, Li S (2014). Field investigation of pile setup in mixed soil. *Geotechnical Testing Journal*, 37(2), 268-281.

Dai G, OuYang H, Gao L, Liu H, Guo Q, Gong W (2023). Monotonic and cyclic lateral behavior of semi-rigid pile in cement-improved clay: centrifuge tests and numerical investigation. *Acta Geotechnica*, 18(8), 4157-4181.

DNV GL (2020). SESAM User Manual: Splice—Structure-Pile-Soil Interaction Analysis. DNV GL AS, Høvik, Norway.

Duan L, Fan M, Zhan B, Wang H, Liu H, Tang G, Geng B (2024). Experimental study on the failure mechanism of finned pile foundation under horizontal cyclic loads. *Buildings*, 14(9), 2814.

Geotechnical Report (2013). Assessment of Pile Foundation Integrity. Caspian Sea, Azerbaijan.

Hacıefendioğlu K, Birinci F (2015). Seismic analysis of offshore wind turbine including fluid- structure-soil interaction. *Challenge Journal of Structural Mechanics*, 1(4), 198–201.

Horsnell MR, Aldridge TR, Erbrich C (1990). Lateral group behavior of piles in offshore soil conditions. *Proceedings of the Offshore Technology Conference*, Houston, TX, USA.

Hu T, Dai G, Wan Z, Fang B, Chen X (2023). Full-scale tests on the grouting effectiveness of offshore bored piles with various bearing strata. *Applied Ocean Research*, 141, 103791.

Karalar M, Demirköse M, Necati M (2024). Effect of soil types on nonlinear earthquake behavior of buildings. *Challenge Journal of Structural Mechanics*, 10(1), 7–13.

Krishnanunni KT, Rathod D (2024). Behaviour of a laterally loaded short-finned pile located on sloping ground. *International Journal of Physical Modelling in Geotechnics*, 24(3), 110-123.

LeBlanc C, Houlsby GT, Byrne BW (2010). Response of stiff piles in sand to long-term cyclic lateral loading. *Géotechnique*, 60(2), 79-90.

Liu J, Guo L, Zhang R (2019). Dynamic response of offshore open-ended pile under lateral cyclic loadings. *Journal of Marine Science and Engineering*, 7(5), 128.

Memarpour MM, Zhang Y, Niazi H (2012). Cyclic lateral response of pile foundations in offshore platforms. *Computers and Geotechnics*, 42, 180-192.

Qin H, Hung CY, Wang H, Zhang J (2024). Response of laterally loaded finned piles in sand. *Acta Geotechnica*, 19(4), 1765-1786.

Randolph M, Gourvenec S (2011). Offshore Geotechnical Engineering. 1st ed. CRC Press, Boca Raton, FL, USA.

Sallam A, Nasr A, Azzam W (2024). Effect of simultaneous torsional and lateral loads on shaft piles with fins in sandy soil. *Geotechnical and Geological Engineering*, 42(5), 3777-3803.

Seidel M, Coronel MC (2011). A new approach for assessing offshore piles subjected to cyclic axial loading. *Geotechnik*, 34(4), 276-284.

Şermet F, Yiğit ME, Yıldız M (2022). Analysis of offshore wind turbine towers with different types of buoys in linear wave action by finite element method. *3rd International Conference on Applied Engineering and Natural Sciences*, 1617-1624.

Sun M, Shan Z, Wang W, Xu S, Liu X, Zhang H, Guo X (2024). Numerical investigation into the stability of offshore wind power piles subjected to lateral loads in extreme environments. *Journal of Marine Science and Engineering*, 12(6), 915.

Tedesco G (2013). Offshore tower or platform foundations: Numerical analysis of a laterally loaded single pile or pile group in soft clay and analysis of actions on a jacket structure. *Ph.D. thesis*, University of Bologna, Bologna, Italy.

Thangavel JK, Rathod D (2024). Behaviour of a laterally loaded rigid pile subjected to one-way cyclic loading. *Geotechnical and Geological Engineering*, 42(6), 4931-4951.

Wang J, Su L, Xie L, Ling X (2024). Quasi-static model test of pile-supported wharf under cyclic lateral loading. *Journal of Marine Science and Engineering*, 12(1), 115.

Xu DS, Xu XY, Li W, Fatahi B (2020). Field experiments on laterally loaded piles for an offshore wind farm. *Marine Structures*, 69, 102684.

Xu X, Wang Q, Zhao Y (2021). Dynamic stability analysis of pile foundation under wave load. *International Journal of Geomechanics*, 21(4), 04021021.

Yigit ME, Özdemir A, Şermet F, Pınarlık M (2018). Analysis of Offshore wind turbine towers with different design by finite elements method. *International Journal of Advanced Research in Engineering*, 43, 1-4.

Challenge Journal of STRUCTURAL MECHANICS

Research Article

Investigating Iosipescu shear properties of laser powder bed fusion 316L stainless steel via digital image correlation technique

Elanur Çelebi Kavdır [a], Gürkan Kaya [a,*], Yusuf Polat [a,b]

[a] *Department of Mechanical Engineering, Erzurum Technical University, 25050 Erzurum, Türkiye*
[b] *High Technology Application and Research Center, Erzurum Technical University, 25050 Erzurum, Türkiye*

ABSTRACT

Laser Powder Bed Fusion (LPBF) has been widely adopted for producing stainless steel 316L components with complex geometries; however, despite extensive research on its tensile performance, the shear behavior of LPBF 316L remains insufficiently characterized. Reliable shear properties are crucial for structural components operating under multiaxial loading, yet experimental data enabling accurate calibration of multiaxial yield and failure models are still scarce. In this study, the tensile and shear responses of LPBF 316L were systematically investigated through standard uniaxial tensile testing and Iosipescu shear testing, supported by full-field Digital Image Correlation (DIC). All specimens were fabricated using LPBF system, and their build orientations were precisely documented to account for anisotropy effects. Tensile tests yielded an ultimate tensile strength of approximately 650 MPa and an average elastic modulus of 197 ± 32 GPa. Iosipescu shear tests demonstrated a maximum shear stress of 621 MPa, revealing a notably close relationship between shear strength and tensile strength. The experimentally measured shear modulus was also consistent with the tensile-derived value through classical elastic relations. The combined results deepen our understanding of LPBF 316L mechanical behavior, especially the coupling between tensile and shear responses. The findings further highlight the importance of integrating shear data into design procedures, multiaxial stress assessments, and material databases for additively manufactured stainless steels. Overall, this study provides a robust experimental foundation for improving structural integrity assessments and advancing the design of LPBF 316L components subjected to complex loading.

ARTICLE INFO

Article history:
Received – September 17, 2025
Revision requested – December 1, 2025
Revision received – December 23, 2025
Accepted – December 29, 2025

Keywords:
Laser powder bed fusion
316L stainless steel
Shear strength
Iosipescu test
Digital image correlation

Citation: Çelebi Kavdır E, Kaya G, Polat Y (2026). Investigating Iosipescu shear properties of laser powder bed fusion 316L stainless steel via digital image correlation technique. *Challenge Journal of Structural Mechanics*, 12(1), 45–54.

1. Introduction

Additive manufacturing (AM) enables the production of geometrically complex and material-efficient components directly from digital models (Fidan et al. 2023; Bănică et al. 2024; Ramos et al. 2025). Within metallic AM, laser powder bed fusion (LPBF) is among the most established techniques due to its ability to achieve near-full density, excellent dimensional accuracy, and tailored microstructural features (Drissi-Daoudi et al. 2023). However, the inherent cyclic thermal history of LPBF introduces unique microstructural characteristics, such as cellular or columnar grains, alongside process-related imperfections including porosity and residual stresses. These features strongly influence the resulting mechanical properties, often leading to anisotropy when compared with conventionally manufactured counterparts. As a result, LPBF continues to attract significant research attention, not only for its capacity to manufacture functional end-use components but also for the need to thor-

* *Corresponding author*. E-mail address: gurkan.kaya@erzurum.edu.tr (G. Kaya)
ISSN: 2149-8024 / DOI: https://doi.org/10.20528/cjsmec.2026.01.004

oughly understand the interplay between process, microstructure, and mechanical performance (Gençoğlu et al. 2022; Ismail et al. 2025). Accordingly, robust mechanical characterisation of LPBF materials should be grounded in rigorously validated reference datasets, since incomplete, inconsistent, or non-traceable records can bias property assessment and undermine cross study comparability (Arzomand et al. 2024). In parallel, data driven modelling approaches including machine learning have been increasingly used to infer critical engineering properties from experimental datasets, thereby reducing reliance on labour intensive and time consuming test campaigns while supporting more efficient materials qualification and decision making (More and Kambekar 2025). Moreover, the growing emphasis on timely and non-destructive evaluation has accelerated the use of wireless sensor networks and in situ monitoring frameworks for continuous condition tracking and early anomaly detection; these principles are directly relevant to LPBF process monitoring and NDE based verification pipelines aimed at linking process signatures to resulting mechanical performance (Narwade and Jadhav 2025).

316L stainless steel remains one of the most investigated alloys in LPBF because of its weldability, corrosion resistance, and stable austenitic structure. Its LPBF-processed form typically shows fine microstructural features and mechanical properties comparable to or exceeding those of conventionally processed 316L (Karthik et al. 2021; Sun et al. 2021; Wang et al. 2021; Tang et al. 2022; Drissi-Daoudi et al. 2023). A quantitative comparison of the measured tensile and shear properties with those reported for LPBF 316L shows that the values obtained in this study fall within the typical ranges documented in recent literature. The observed differences can be associated with microstructural variations arising from thermal histories during processing, as also emphasized by (Rottler et al. 2025b), who demonstrated how heat-driven transformations influence mechanical response. Similarly, (Rottler et al. 2025a) on LPBF temperature history highlights the role of heat accumulation and cooling rates in dictating defect formation and microstructural stability, providing context for the mechanical trends observed here. Overall, this comparison confirms that the present tensile–shear dataset is consistent with established LPBF behavior while offering additional insight into shear response, which remains underreported.

The Iosipescu shear test is a widely used method to determine shear properties of metals and composites (Adams 1990; Stojcevski et al. 2018). It provides a full shear stress–strain response and avoids some limitations of alternative techniques such as the short-beam shear test (Allott and Czabaj 2021), off-axis shear test (Gao et al. 2025), and three-rail shear test (May and Kilchert 2022). The specimen features two opposing V-notches at mid-width that produce a reduced cross-section where the shear stress concentrates, enabling controlled shear failure in the central gauge region (Ramezani Dana et al. 2024). For the tensile and compression loading, the notches act as stress concentrations; however, it is negligible for the shear loading. This phenomenon results in a much more uniform shear stress distribution than unnotched shear specimens. In contrast to unnotched geometries, which develop parabolic shear distributions, the Iosipescu geometry provides conditions suitable for accurate determination of shear modulus and shear strength, even for materials with heterogeneous microstructures such as LPBF metals (Liu et al. 2025). In addition to the advantages of the V-notched shear specimen, the DIC method may contribute to capturing displacements of the full-field area under shear loading, which offers a widely validated approach for determining material properties (Jerabek et al. 2010). DIC has also been adapted for in-situ monitoring of large-scale additive manufacturing processes by exploiting the natural surface texture of polymer–composite prints, enabling accurate tracking of full-field deformation and warpage throughout the build (Spencer et al. 2021). Similarly, high-precision full-field deformation measurements in arc-based directed energy deposition have been achieved using both 2D- and 3D-DIC, with results validated against numerical simulations and shown to reliably capture strain evolution despite challenges such as arc light and steep thermal gradients (Wang et al. 2023).

The implementation process of DIC can be summarized in three main steps. First, the surface of the specimen must be prepared with a random speckle pattern. For this purpose, the surface is initially cleaned and coated with a thin white base layer. Once dried, a fine black spray is applied to generate the required random speckle distribution. Following surface preparation, specimens were positioned in the testing apparatus and digital images were captured before and after deformation. Then, the obtained image sets were then processed using correlation algorithms to evaluate displacement and strain fields (Kavdir and Aydin 2019).

Despite growing interest, shear data for LPBF 316L remain scarce, and most applications of the Iosipescu method in metal additive manufacturing have been limited to systematically studying the shear response of LPBF 316L stainless steel. Furthermore, the researchers continue to debate the most suitable approaches for accurately characterizing shear behavior, which underlines the importance of using DIC to validate the strain distribution in the notched region. In this work, we address these gaps by (i) fabricating LPBF 316L Iosipescu specimens and evaluating their as-built shear response with DIC measurement, and (ii) benchmarking the results against co-fabricated tensile specimens to establish a direct comparison between shear and tensile behavior. This combined testing strategy provides a more comprehensive understanding of LPBF 316L under different loading conditions, complementing the tensile-dominated literature and supporting the development of more reliable design data for engineering applications.

In structural applications, most load-bearing components are subjected to complex, multiaxial stress states rather than purely uniaxial tension. Under such conditions, shear stresses often play a dominant role in both yielding and failure initiation. Therefore, reliable shear property data are essential not only for ensuring safe and robust structural design but also for accurately calibrating multiaxial yield criteria such as von Mises, Tresca, and other advanced constitutive models. This

need becomes even more critical for additively manufactured metals like LPBF 316L, whose microstructural heterogeneities, residual stresses, and anisotropy may cause deviations from the behavior of conventionally produced alloys. The scarcity of experimentally validated shear data in the literature thus represents a significant gap that limits the development of dependable design frameworks and material databases for LPBF components. By providing comprehensive shear measurements alongside tensile data, the present study aims to help close this gap and to support more accurate assessment of LPBF 316L under realistic loading conditions.

2. Materials and Methods

In this study, three specimens were prepared for each test type, i.e., tensile and Iosipescu shear tests, in order to determine the corresponding tensile and shear mechanical properties of the LPBF-fabricated material. In addition, strain analyses were performed using the DIC technique to obtain full-field deformation measurements.

DIC was employed to capture full-field deformation and strain data during tensile and Iosipescu shear tests. DIC analyses were carried out in GOM Correlate with subset sizes of 15–25 pixels and step sizes of 10–19 pixels depending on speckle quality and image resolution. Bicubic interpolation and a second-order shape function were used, and correlation was performed with the Zero-Normalized Cross-Correlation criterion. The measurements were carried out with an AVE2 video extensometer attached to the tensile testing machine, equipped with a 16 mm focal length lens. Prior to testing, the specimens (tension and Iosipescu) were prepared with a random speckle pattern by first applying a white base layer and then spraying fine black dots using matte spray paint, as shown in the Figs. 3–5.

2.1. Materials

316L stainless steel powder served as the feedstock material for additive manufacturing via the LPBF method. The particle diameter distribution was determined to be approximately 10–45 μm. Microscopic inspection confirmed that the powder possessed a nearly spherical morphology without agglomeration (see Fig. 1).

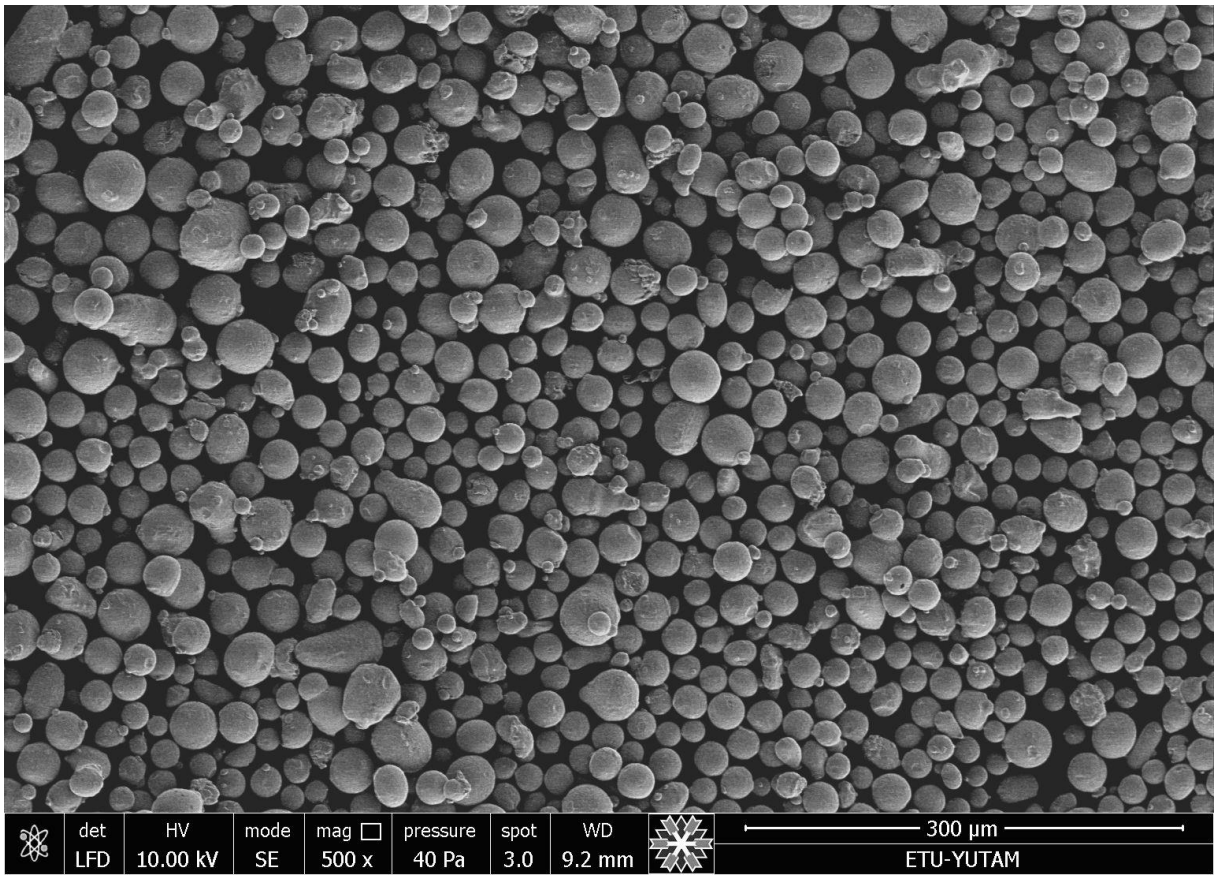

Fig. 1. SEM image of 316L stainless steel powder.

2.2. Laser powder bed fusion technique

Tensile and Iosipescu shear specimens were produced from 316L stainless steel powder using the LPBF technique to evaluate shear behavior. Manufacturing was carried out on a Concept Laser M Lab R system under a nitrogen-protected environment, with oxygen concentration maintained below 1%. The applied process parameters were a laser power of 90 W and a scan speed of 1500 mm/s. The CAD models of the specimens were converted into STL format using AutoFab software. The images of the fabricated specimens are displayed in Fig. 2.

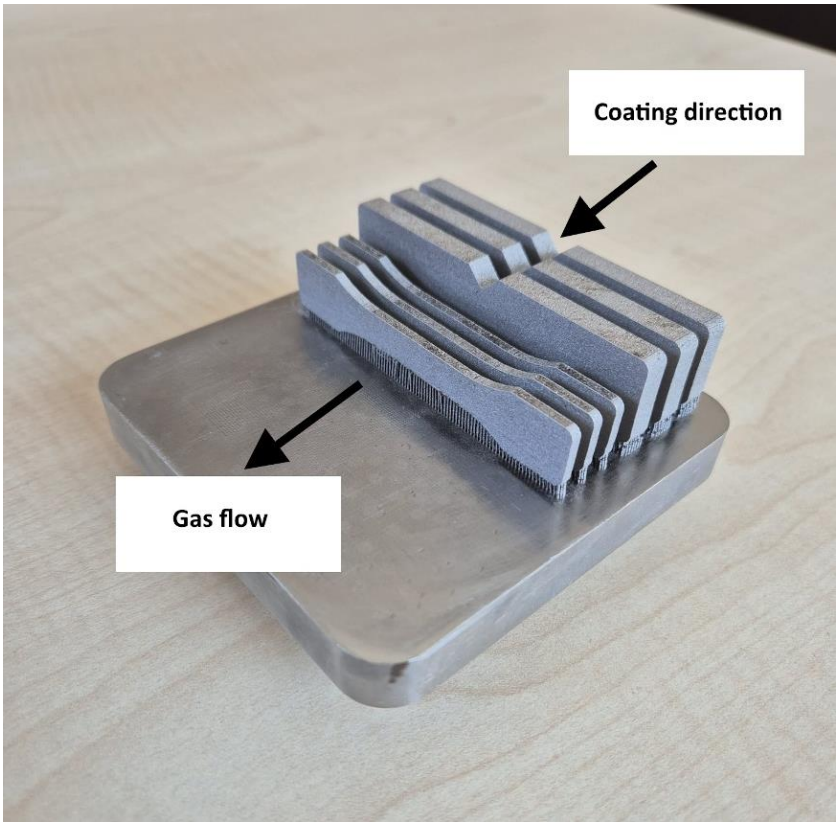

Fig. 2. Tensile and Iosipescu test samples on the LPBF platform.

All specimens were tested in the as-built condition without the application of any thermal post-processing such as stress-relief annealing or hot isostatic pressing (HIP). This choice was made to preserve the intrinsic LPBF microstructure and residual stress state, allowing the shear and tensile behavior to be evaluated directly in the as-fabricated condition.

The production orientation of the test specimens, forces applied during the test and Iosipescu test specimens are given in Fig. 3.

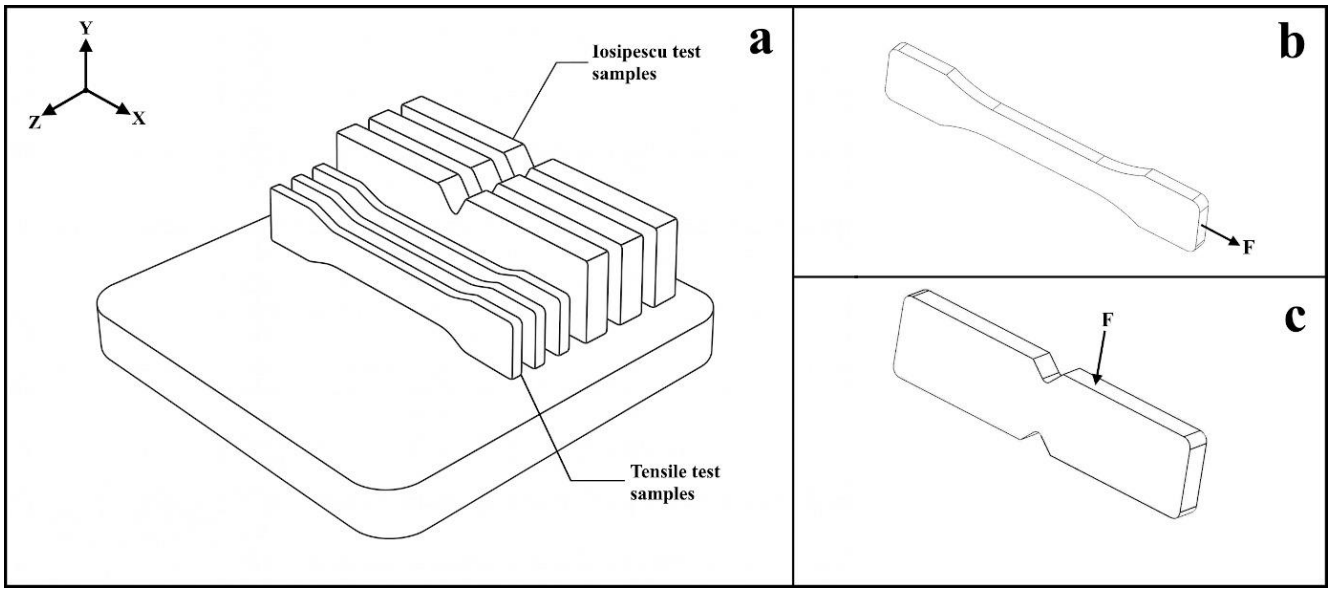

Fig. 3. Schematic representation of the build orientation and specimen alignment for tensile and Iosipescu tests.

2.3. Tensile test

Uniaxial tensile tests were carried out on three specimens using an Instron 5982 static testing machine, as shown in Fig. 4. The specimens were prepared in accordance with standardized geometry (ASTM D638 / ISO 527 type IV dimensions), with an overall length of 75 mm and a thickness of 2 mm. The crosshead displacement rate was set to 1 mm/min throughout the experiments.

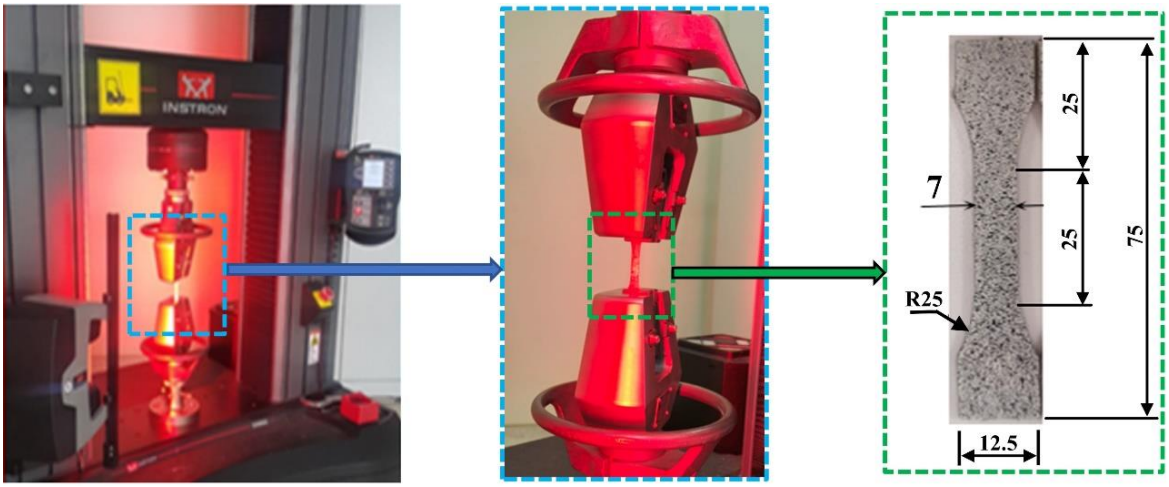

Fig. 4. Experimental setup of the tensile test and geometry of the tensile specimen (dimensions are mm).

The full-field deformation measurements were obtained using the DIC technique, where virtual extensometers (see Fig. 5) were defined along the gauge section to evaluate both axial and lateral strain components. The load–displacement curves were then generated by combining the load data from the load cell with the displacement values measured via DIC. From these curves, the elastic constants (elastic modulus and Poisson's ratio) and the overall stress–strain behavior were determined using the following equations:

$$\sigma_i = P_i/A \tag{1}$$

$$\varepsilon_i = \delta_i/L \tag{2}$$

$$E = \Delta\sigma/\Delta\varepsilon \tag{3}$$

$$\nu = -\Delta\varepsilon_t/\Delta\varepsilon_l \tag{4}$$

where P_i: load value at point i (N), σ_i: normal stress value at point i (MPa), δ_i: displacement value at point i (mm), ε_i: strain value at point i (mm/mm), E: elastic modulus (MPa), ν: Poisson's ratio, L: gauge length (mm), A: cross-sectional area (mm^2) of the specimen.

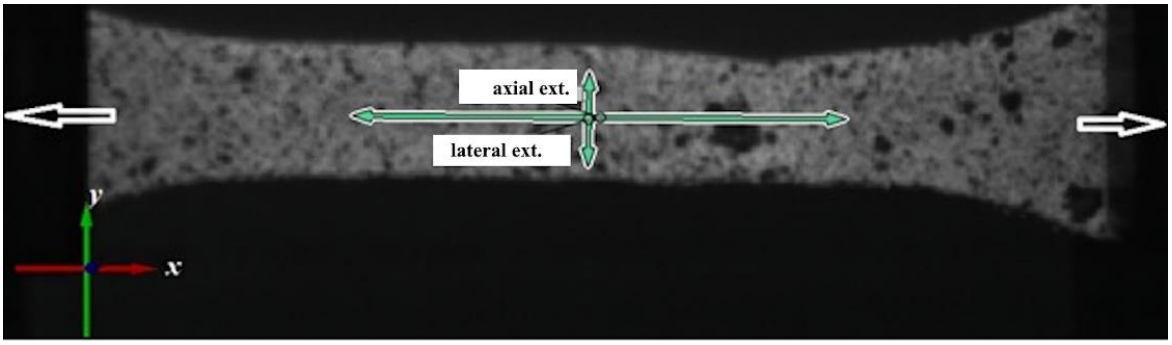

Fig. 5. Representation of the virtual extensometers and coordinate system used in the DIC analysis.

2.4. Iosipescu shear test

The shear properties of the LPBF-fabricated metallic specimens were determined using the Iosipescu shear test in accordance with ASTM D5379/D5379M (V-notched beam method). The experiments were conducted on an Instron 5982 static testing machine at a crosshead displacement rate of 1 mm/min. DIC analysis was employed to determine the shear strain, where virtual extensometers were positioned at ±45° angles within the gauge section. This approach enabled an accurate evaluation of the shear stress–strain response, the in-plane elastic shear modulus, and the shear-related mechanical properties of the material. The specimen geometry and test configuration are presented in Fig. 6.

The shear stress–strain relationship for the Iosipescu specimens was evaluated using the following standard formulations, which enable the determination of shear stress, total shear strain, and shear modulus:

$$\gamma = |\varepsilon_1| + |\varepsilon_2| \tag{5}$$

$$\tau = \frac{F}{tw} \tag{6}$$

$$G = \frac{\tau}{\gamma} \tag{7}$$

In these equations, ε_1 and ε_2: the shear strain components, F: applied force (N), t: specimen thickness (mm), w: specimen width (mm), τ: shear stress (MPa) and γ: total shear strain. The shear modulus is calculated as the ratio of shear stress to shear strain.

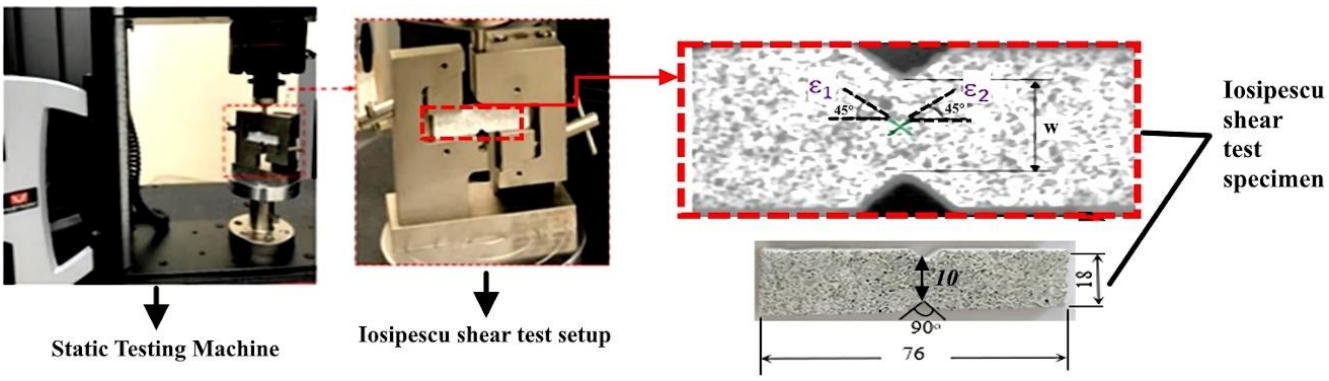

Fig. 6. Specimen geometry and test configuration (dimensions are mm, thickness 5 mm).

3. Results and Discussion

3.1. Tensile test results

The mechanical properties of the three specimens, including true stress, strain, Poisson's ratio, and elastic modulus, are summarized in Table 1 (E: Modulus of elasticity; ν: Poisson's ratio; σ_u: Ultimate strength; ε_{f_a}: Maximum axial strain; ε_{f_l}: Maximum lateral strain). In addition, the Fig. 7 presents the engineering stress-strain curves obtained for each tested specimen.

Table 1. Tensile test results.

Properties	Mean value (±SD)
E (GPa)	197.1 ± 32.1
ν	0.326 ± 0.096
σ_u (MPa)	649.6 ± 7.4
ε_{f_a}	0.243 ± 0.096
ε_{f_l}	−0.085 ± 0.038

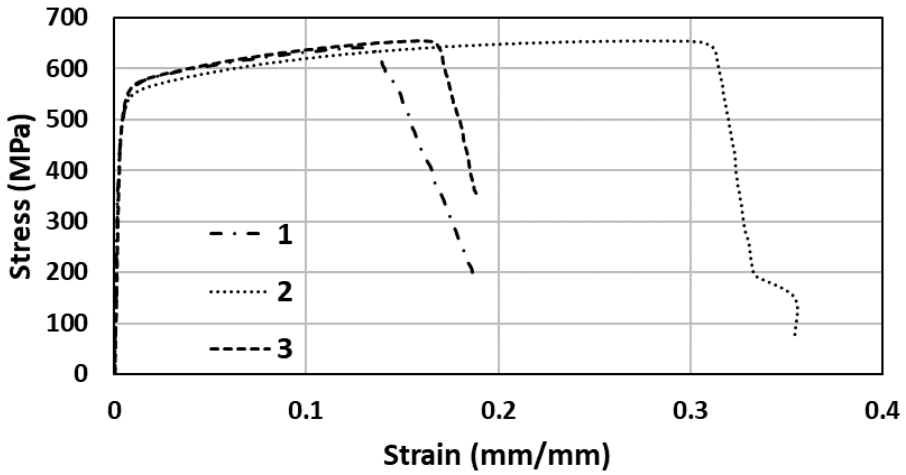

Fig. 7. The engineering stress-strain curves for tensile test specimens.

The tensile test results revealed that the LPBF-fabricated metallic specimens exhibited a highly consistent tensile strength, with an average ultimate stress of 649.6 ± 7.4 MPa. In contrast, noticeable variations were observed in the elastic modulus (197.1 ± 32.1 GPa) and strain values, indicating heterogeneity in stiffness and ductility among the specimens. The stress–strain curves (Fig. 7) confirmed these findings, showing similar maximum stress levels but different slopes in the elastic region and varying strain-to-failure values. These differences are likely related to microstructural heterogeneities or process-induced defects inherent to the additive manufacturing process. Overall, the results suggest that while tensile strength is reproducible and reliable, further optimization of the LPBF process parameters is required to achieve more uniform stiffness and ductility.

The evolution of the damage process during tensile loading was captured by the DIC strain maps presented along with the stress–strain curve (see Fig. 8). Here, (a) represents the initial state without load and no elongation, (b) corresponds to $\varepsilon \approx 0.09$, (c) to $\varepsilon \approx 0.23$, and (d) to $\varepsilon \approx 0.33$, showing the normal strain distributions along the loading direction. At the initial stage, the axial strain distribution was relatively homogeneous throughout the gauge section, indicating uniform elastic and early plastic deformation. As the applied strain increased, strain gradients became more pronounced and the onset of localized deformation could be observed, reflecting the initiation of necking in the specimen. At the later stage, strain localization intensified significantly, with the highest strain values concentrated within a narrow band that corresponded to the eventual fracture site. This evo-

lution demonstrates a transition from diffuse plastic deformation to localized necking, followed by fracture, which is consistent with the post-peak softening observed in the stress–strain response. Such results highlight the capability of DIC to provide full-field insights into the deformation and failure mechanisms of additively manufactured metallic materials under tensile loading.

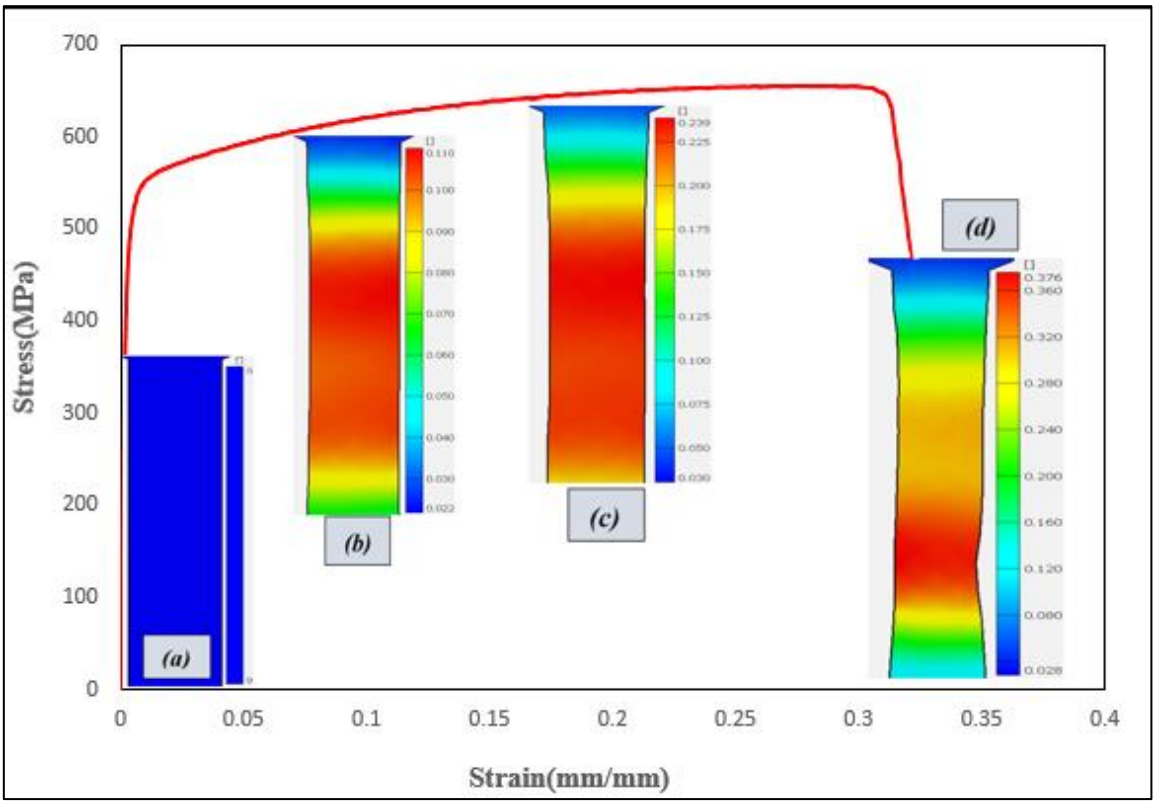

Fig. 8. Engineering stress–strain curve of the tensile specimen with corresponding DIC normal strain maps at different loading stages.

3.2. Iosipescu shear test results

Three Iosipescu specimens were tested under shear loading, and the experimental results are presented in Table 2 (G: Shear modulus; τ_f: Maximum shear stress; γ_f: Maximum shear strain), and the shear stress-strain curves are given in Fig 9.

Table 2. Iosipescu shear test results.

Properties	Mean value (±SD)
G (GPa)	72.0 ± 2.6
τ_f (MPa)	621.2 ± 21.1
γ_f	0.577 ± 0.045

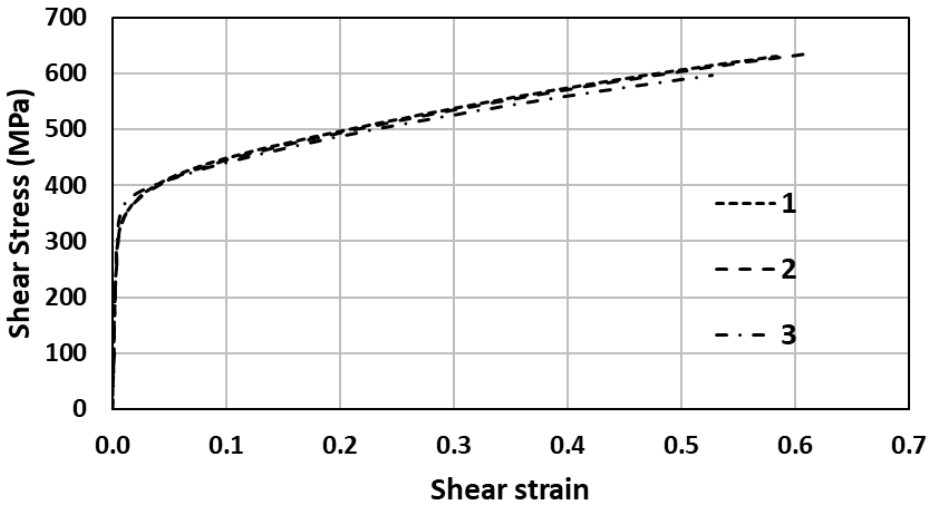

Fig. 9. The engineering shear stress-strain curves for Iosipescu test specimens.

The Iosipescu shear test results of the LPBF-fabricated specimens demonstrated highly consistent behavior among the three samples. The average shear modulus was calculated as 72.0 ± 2.6 GPa, indicating good agreement of stiffness values across the specimens. Similarly, the maximum shear stress (621.2 ± 21.1 MPa) showed a very narrow scatter, confirming the reliability and repeatability of the shear strength. The maximum shear strain was determined as 0.577 ± 0.045, suggesting that the ductility of the material also followed a consistent trend. The shear stress–strain curves nearly overlapped, further verifying the uniformity of the experimental results. In particular, the elastic region slopes were well aligned with the calculated shear modulus values, while the peak stresses and strain-to-failure levels revealed no significant deviation among the specimens. Overall, these results emphasize that the shear response of additively manufactured metallic materials is not only reproducible but also homogeneous in terms of stiffness, strength, and ductility, which underlines the reliability of the applied methodology.

The maximum shear stress obtained from the Iosipescu tests (≈ 621 MPa) is in close agreement with the ultimate tensile strength (≈ 650 MPa). This correspondence is noteworthy in the context of multiaxial yield criteria. While von Mises and Tresca predict shear yield stresses of $\sigma_y/\sqrt{3}$ and $\sigma_y/2$, respectively, the experimental results suggest a shear resistance approaching the tensile strength. Such behavior highlights the unique microstructural response of LPBF 316L and provides a useful reference point for calibrating multiaxial constitutive models and failure criteria in additively manufactured metals.

Fig. 10 presents the shear strain distributions of the Iosipescu specimen at different loading stages. These strain maps clearly illustrate the evolution of deformation and the formation of a pure shear strain field in the central gauge section. Although there are only a limited number of studies addressing the shear properties of metallic materials using the Iosipescu test, the present results confirm the suitability of this method. The consistency observed among the specimens, together with the DIC-based strain maps, demonstrates that the expected shear strain field was successfully generated, which is essential for accurately determining shear mechanical properties. This gap underscores, DIC provided full-field strain data that cannot be captured through conventional deformation measurement techniques, thus validating both the accuracy of the Iosipescu test and the reliability of the experimental procedure. Overall, the combination of Iosipescu testing and DIC analysis offers a powerful approach for the comprehensive characterization of shear behavior in additively manufactured metallic materials.

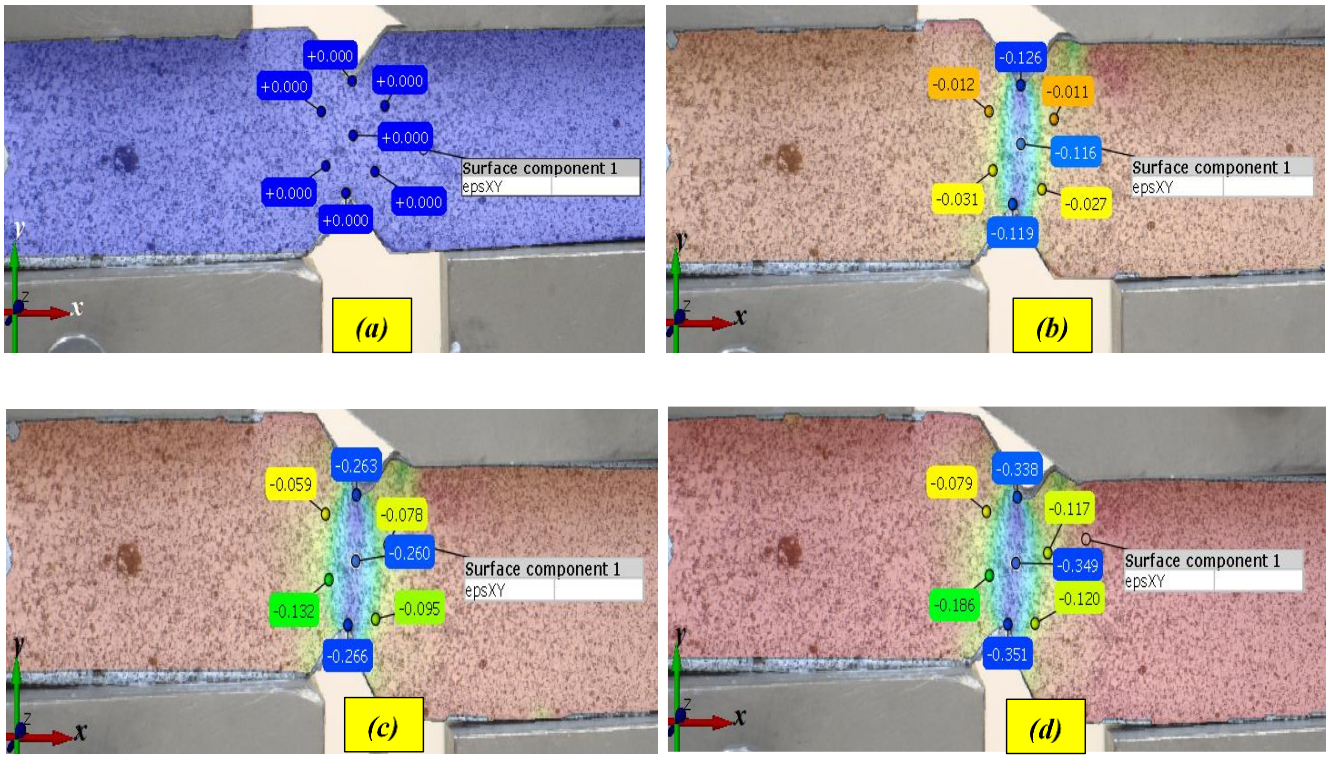

Fig. 10. Evolution of shear strain distribution in the Iosipescu specimen at different loading stages: (a) γ = 0; (b) γ = 0.189; (c) γ = 0.456; (d) γ = 0.604.

4. Conclusions

In this study, the tensile and shear properties of 316L stainless steel fabricated by laser powder bed fusion were systematically investigated using the digital image correlation technique. Particular emphasis was placed on characterizing the multiaxial mechanical response, with a focus on shear behavior, which has been scarcely reported for LPBF 316L alloys. The application of DIC enabled full-field strain and displacement measurements, thereby improving the accuracy and reliability of the extracted elastic modulus, shear modulus, and Poisson's ratio.

The experimental results revealed that the LPBF-fabricated specimens exhibited a consistent ultimate tensile strength of 649.6 ± 7.4 MPa, with an average elastic modulus of 197.1 ± 32.1 GPa. Under shear loading, the Iosipescu tests yielded an average shear modulus of 72.0 ± 2.6 GPa and a maximum shear stress of 621.2 ± 21.1 MPa, demonstrating excellent reproducibility and uniformity. The uniform strain distribution observed within the gauge section confirmed that the V-notched Iosipescu method, in combination with DIC, provides a robust and reliable approach for capturing the pure shear stress–strain response.

A key outcome of this work is the close alignment between the tensile and shear strengths, which provides valuable insight into the governing deformation mechanisms of LPBF 316L. This relationship also offers a practical advantage for calibrating multiaxial yield and failure criteria such as von Mises and Tresca, both of which require accurate shear and tensile limits for reliable predictions. The results demonstrate that LPBF 316L exhibits a more uniform strength response under different loading modes than is often assumed, emphasizing the importance of incorporating shear data when evaluating the structural integrity of additively manufactured components.

The combined tensile and shear data obtained in this study offer direct input for engineering design frameworks, particularly those requiring reliable multiaxial material parameters for LPBF 316L. The close correspondence between tensile and shear strengths, together with the experimentally validated shear modulus, enables more accurate calibration of commonly used design criteria such as von Mises and Tresca, as well as improved selection of safety factors for components subjected to complex loading. These experimentally derived properties can also serve as dependable entries for material databases used in design and simulation workflows, thereby supporting more robust structural integrity assessments for LPBF-fabricated 316L components.

The results obtained in this study also have practical implications for the structural design of LPBF 316L components. Since most load-bearing parts operate under multiaxial stress states, the experimentally determined tensile and shear properties — particularly the close values of tensile and shear strength and the validated shear modulus — can serve as reliable input for calibrating multiaxial yield and failure criteria. These data provide a more robust basis for material selection, safety-factor determination, and the development of design databases for additively manufactured 316L structures.

Overall, this work contributes to filling a significant gap in the literature by establishing reliable shear property data for as-built LPBF 316L stainless steel. The outcomes not only enhance the understanding of the material's multiaxial mechanical behavior under complex loading conditions but also provide critical input for the reliable design and structural application of LPBF-fabricated components. In addition to conclusion of this study, a post-treatment study may contribute to the improvement of microstructure of as-built LPBF samples for further tensile and shear properties.

Acknowledgements

The authors would like to thank High Technology Research Center (ETÜ-YÜTAM), Erzurum Technical University because of their support in the experimental stages.

Funding

The authors received no financial support for the research, authorship, and/or publication of this manuscript.

Conflict of Interest

The authors declare no potential conflicts of interest with respect to the research, authorship, and/or publication of this manuscript.

Data Availability

The datasets generated and/or analyzed during the current study are not publicly available but are available from the corresponding author upon reasonable request.

AI Assistance

No AI-based tools were used in the preparation of this manuscript.

Author Contributions

All authors made substantial contributions to the conception and design of the study, acquisition of data, analysis and interpretation of data; drafted or critically revised the manuscript for important intellectual content; and approved the final version to be published.

REFERENCES

Adams DF (1990). The Iosipescu shear test method as used for testing polymers and composite materials. *Polymer Composites*, 11(5), 286–290.

Allott NR, Czabaj MW (2021). Characterization of the interlaminar shear strength of IM7/8552 using small-scale short beam shear tests. *Composites Part A: Applied Science and Manufacturing*, 142, 106200.

Arzomand K, Rustell M, Kalganova T (2024). From ruins to reconstruction: Harnessing text-to-image AI for restoring historical architectures. *Challenge Journal of Structural Mechanics*, 10(2), 69-85.

Bănică CF, Sover A, Anghel DC (2024). Printing the future layer by layer: A comprehensive exploration of additive manufacturing in the era of Industry 4.0. *Applied Sciences*, 14(21), 9919.

Drissi-Daoudi R, Masinelli G, de Formanoir C, Wasmer K, Jhabvala J, Logé RE (2023). Acoustic emission for the prediction of processing regimes in laser powder bed fusion, and the generation of processing maps. *Additive Manufacturing*, 67, 103484.

Fidan I, Huseynov O, Ali MA, Alkunte S, Rajeshirke M, Gupta A, Hasanov S, Tantawi K, Yasa E, Yilmaz O, Loy J, Popov V, Sharma A (2023). Recent inventions in additive manufacturing: Holistic review. *Inventions*, 8(4), 103.

Gao Q, Zhao X, Sun Q (2025). Evaluation of the off-axis and on-axis tensile creep behavior of glass-fiber reinforced polymer unidirectional lamina. *Polymer Composites*, 46(4), 3054–3069.

Gençoğlu U, Kaya G, Ergüder TO, Hacısalihoğlu İ, Yıldız F (2022). Investigation of the structural and tribological properties of 316L stainless steel manufactured using variable production parameters by selective laser melting. *Journal of Materials Engineering and Performance*, 31(5), 3688–3703.

Ismail L, Mohamed OF, Farrah T, George P, Schiffer A (2025). Influence of process parameters on microstructure and interfacial mechanical properties of Al6061/AlSi10Mg multi-material components fabricated via laser powder bed fusion. *Materials Science and Engineering: A*, 928, 148061.

Jerabek M, Major Z, Lang RW (2010). Strain determination of polymeric materials using digital image correlation. *Polymer Testing*, 29(3), 407–416.

Karthik GM, Kim ES, Sathiyamoorthi P, Zargaran A, Jeong SG, Xiong R, Kang SH, Cho JW, Kim HS (2021). Delayed deformation-induced martensite transformation and enhanced cryogenic tensile properties in laser additive manufactured 316L austenitic stainless steel. *Additive Manufacturing*, 47, 102314.

Kavdir EÇ, Aydin MD (2019). The investigation of mechanical properties of a structural adhesive via digital image correlation (DIC) technic. *Composites Part B: Engineering*, 173, 106995.

Liu Z, Wang J, Sun W, Liu X, Gao Z, Li J, Zhan X (2025). Unveiling the dependence of mechanical properties and corrosion resistance on microstructural heterogeneity in additively manufactured 316L stainless steel. *Journal of Materials Research and Technology*, 37, 4688–4707.

May M, Kilchert S (2022). The effect of loading rate on the in-plane shear strength of tri-axial braided composites. *Journal of Composite Materials*, 56(3), 421–426.

More S, Kambekar A (2025). Performance evaluation of compressive strength of concrete using different machine learning algorithms. *Challenge Journal of Concrete Research Letters*, 16(2), 60-68.

Narwade R, Jadhav R (2025). Concrete strength monitoring and damage detection using piezoelectric-based wireless sensor. *Challenge Journal of Concrete Research Letters*, 16(1), 40-50.

Ramezani Dana H, El Mansori M, Contreras Echevarria A, Muñoz Basagoiti MX, Pisarski M, Cucuzzella F, Sansone C (2024). Determination of shear strength of additively manufactured poly lactic acid/flax fibre bio-composite via the iosipescu test. *Composites Communications*, 47, 101858.

Ramos A, Angel VG, Siqueiros M, Sahagun T, Gonzalez L, Ballesteros R (2025). Reviewing additive manufacturing techniques: Material trends and weight optimization possibilities through innovative printing patterns. *Materials*, 18(6), 1377.

Rottler J, Tetzlaff TK, Lion A, Paetzold-Byhain K, Johlitz M (2025a). Temperature history in laser powder bed fusion: Analyzing the effect of heat accumulation on the microstructural state of Ti-6Al-4V. In: Altenbach, H., Hitzler, L., Johlitz, M., Merkel, M., Öchsner, A. (eds) *Lectures Notes on Advanced Structured Materials 3*. Advanced Structured Materials, vol 226. Springer, Cham.

Rottler J, Tetzlaff TK, Wohninsland A, Lion A, Johlitz M (2025b). Thermophysical and microstructural characterization of Ti-6Al-4V in powder and laser powder bed fusion-processed state within the global temperature field range. *Materials and Design*, 253, 113823.

Spencer R, Hassen AA, Baba J, Lindahl J, Love L, Kunc V, Babu S, Vaidya U (2021). An innovative digital image correlation technique for in-situ process monitoring of composite structures in large scale additive manufacturing. *Composite Structures*, 276, 114545.

Stojcevski F, Hilditch T, Henderson LC (2018). A modern account of Iosipescu testing. *Composites Part A: Applied Science and Manufacturing*, 107, 545–554.

Sun C, Wang Y, McMurtrey MD, Jerred ND, Liou F, Li J (2021). Additive manufacturing for energy: A review. *Applied Energy*, 282, 116041.

Tang L, Magdysyuk OV, Jiang F, Wang Y, Evans A, Kabra S, Cai B (2022). Mechanical performance and deformation mechanisms at cryogenic temperatures of 316L stainless steel processed by laser powder bed fusion: In situ neutron diffraction. *Scripta Materialia*, 218, 114806.

Wang Q, Jia J, Zhao Y, Wu A (2023). In situ measurement of full-field deformation for arc-based directed energy deposition via digital image correlation technology. *Additive Manufacturing*, 72, 103635.

Wang X, Sanchez-Mata O, Atabay SE, Muñiz-Lerma JA, Attarian Shandiz M, Brochu M (2021). Crystallographic orientation dependence of Charpy impact behaviours in stainless steel 316L fabricated by laser powder bed fusion. *Additive Manufacturing*, 46, 102104.

Challenge Journal of STRUCTURAL MECHANICS

Research Article

Optimal metaheuristic design of CFRP wrapping for enhancing the shear capacity of reinforced concrete columns

Ammar Khalbous [a], Gebrail Bekdaş [a], Sinan Melih Nigdeli [a,*], Aylin Ece Kayabekir [b]

[a] *Department of Civil Engineering, İstanbul University-Cerrahpaşa, 34320 İstanbul, Türkiye*
[b] *Department of Civil Engineering, İstanbul Gelişim University, 34310 İstanbul, Türkiye*

ABSTRACT

Reinforced concrete (RC) columns are prone to brittle shear failure under lateral loads like earthquakes, especially in older structures. Carbon fiber reinforced polymer (CFRP) wrapping effectively enhances shear capacity, ductility, and energy dissipation. This study optimizes CFRP jacket design to increase shear strength while minimizing material volume per meter of column. The objective function includes the number of layers (n), strip width (W_f), spacing (S_f), and thickness (t_f), following ACI 440.2R-2017 and ACI 318-05 constraints on strain, shear contribution, and capacity. Three metaheuristic algorithms—JAYA, Teaching-Learning-Based Optimization (TLBO), and Flower Pollination Algorithm (FPA)—were used to solve the nonlinear problem in MATLAB with randomized populations, 100–500 iterations, and 30 independent runs. Analyses for 100–500 kN shear demands (20%–100% increases) yield valid designs. Low shear demands typically require minimal CFRP, often a single layer with moderate strip width and large spacing. Higher demands required more intensive reinforcement through increased layer count and reduced spacing, with width adjustments as needed to satisfy code constraints. FPA achieved the lowest CFRP volumes due to its Lévy-flight global search, TLBO produced the most stable results with low variability, and JAYA offered the fastest computation. Increasing iteration count and population size improved convergence in all algorithms, yielding solutions closer to the optimum. Results confirm that metaheuristics enable economical, reliable CFRP retrofitting, promoting sustainability. Future work could include multi-objective optimization for cost and constructability.

ARTICLE INFO

Article history:
Received – November 17, 2025
Revision requested – January 22, 2026
Revision received – January 29, 2026
Accepted – February 9, 2026

Keywords:
CFRP strengthening
Shear capacity
Metaheuristic optimization
JAYA algorithm
Teaching-learning-based optimization
Flower pollination algorithm

Citation: Khalbous A, Bekdaş G, Nigdeli SM, Kayabekir AE (2026). Optimal metaheuristic design of CFRP wrapping for enhancing the shear capacity of reinforced concrete columns. *Challenge Journal of Structural Mechanics*, 12(1), 55–64.

1. Introduction

Shear reinforcement, typically in the form of stirrups, plays a critical role in reinforced concrete (RC) structures. It resists shear forces to ensure structural safety and durability. However, in cases involving increased seismic demands, retrofitting requirements, changes in building function, or structural extensions, an enhancement of the shear capacity beyond the original design may become necessary (Xie et al. 2005). Traditionally, this improvement has been achieved through sheathing, where the structural member is encased to increase its load-bearing capacity. Although effective, this technique adds significant weight and stiffness, often requiring a comprehensive redesign to accommodate the redistribution of internal forces. To overcome these drawbacks, modern strengthening methods employ carbon fiber reinforced polymer (CFRP) strips, offering a lightweight and flexible alternative that enhances shear strength without altering the section's mass or stiffness, thereby maintaining the original structural performance while simplifying application (Gkournelos et al. 2021).

* *Corresponding author*. E-mail address: melihnig@iuc.edu.tr (S. M. Nigdeli)
ISSN: 2149-8024 / DOI: https://doi.org/10.20528/cjsmec.2026.01.005

Despite the proven structural efficiency of CFRP, the high material cost remains a primary constraint for its widespread application, particularly in large-scale retrofitting projects. Traditional manual design methods often lead to conservative, 'over-designed' solutions that utilize excessive amounts of expensive composite material. Consequently, determining the precise minimum volume of CFRP required to meet safety standards is not merely a technical challenge but an economic necessity. This creates a critical need for automated approaches that can rigorously minimize material usage while strictly adhering to design codes.

Optimization is the systematic process of determining design variables that achieve the best possible outcome under defined constraints. In structural engineering, it is widely applied to obtain cost-effective and high-performance designs. While conventional mathematical methods, such as linear or nonlinear programming, are efficient for simple problems, they often fail to converge for the nonlinear, discontinuous, or multi-modal objective functions typically encountered in RC design. To overcome these challenges, metaheuristic algorithms have emerged as robust tools capable of exploring large and complex search spaces without requiring gradient information (Ulusoy et al. 2020; Tomar et al. 2023). Beyond single objective cost minimization, recent structural design studies increasingly adopt multi objective or multi criteria frameworks that simultaneously enforce code based strength and serviceability requirements while minimizing direct material usage and project cost. Within these formulations, weighting coefficients or penalty terms are commonly used to balance competing design targets (e.g., minimum CFRP quantity versus safety margins) and to prioritize constructible solutions through discrete design choices. Accordingly, the metaheuristic search and data driven surrogate modelling logic used to reduce repetitive search runs in cost driven optimization can be extended to CFRP shear strengthening by learning the mapping between discrete design variables and key performance indices including code compliance, cost, and constructability (Çoşut et al. 2023).

Consistent with this direction, hybrid workflows that first generate optimization datasets via metaheuristic search and then train machine learning surrogate models have gained attention, because they enable rapid estimation of near optimal design variables and objective values under combined constraints, thereby reducing the need to re run computationally expensive search procedures (Aydın et al. 2024). Accordingly, in the present study, design alternatives generated by JAYA, TLBO, and FPA are used to train surrogate models that map discrete CFRP strengthening variables (e.g., strip width, spacing, and number of layers) to code compliant shear capacity and cost metrics, enabling fast screening of constructible and economically efficient retrofitting solutions without repeated full optimization runs.

In recent years, the application of metaheuristic optimization in the design of CFRP-strengthened RC members has gained significant traction. The primary objective of these studies is to determine the optimal configuration of parameters—such as FRP area, strip width, spacing, and number of layers—to maximize structural performance while minimizing material costs. Early contributions focused heavily on traditional algorithms. For instance, Dugguh (2015) utilized Genetic Algorithms (GA) to perform multi-objective optimization of circular hollow sections strengthened with CFRP. Similarly, Rahman et al. (2012) employed GA to minimize the cost of both CFRP plates and epoxy adhesives for externally strengthened beams, ensuring compliance with serviceability limits. More recently, research has shifted towards modern algorithms. Kayabekir et al. (2018) applied the Jaya algorithm to optimize the strip width and spacing of CFRP for the shear strengthening of RC beams, highlighting the algorithm's implementation simplicity. In another study, Kayabekir (2018) investigated the use of Teaching-Learning-Based Optimization (TLBO) and Flower Pollination Algorithm (FPA) to enhance the shear capacity of T-beams, proposing optimal wrapping thicknesses and layouts. Comparative studies have also been conducted; for example, Yücel (2025) compared FPA and Particle Swarm Optimization (PSO) for CFRP plate placement on RC beams, demonstrating that FPA outperformed PSO in terms of objective function accuracy and structural weight minimization. Furthermore, hybrid approaches such as the GA-PSO-TLBO method proposed by Yun et al. (2023) have shown that combining algorithms can offer robust strategies for complex engineering problems.

However, a critical review of the literature reveals specific gaps. While previous studies have successfully applied algorithms like GA and PSO, these methods often require the tuning of complex control parameters (e.g., mutation rates, inertia weights), which can be a barrier for practical engineering applications. Moreover, the majority of existing optimization works treat design variables (e.g., strip spacing) as continuous values, yielding theoretical solutions that are difficult to implement onsite (e.g., a spacing of 137.5 mm). The present research addresses these limitations by specifically introducing parameter-free and parameter-light metaheuristics—JAYA (Rao 2016), Teaching–Learning-Based Optimization (TLBO) (Rao et al. 2011), and Flower Pollination Algorithm (FPA) (Yang 2012)—to the domain of CFRP shear strengthening.

Unlike previous works that focused on beam flexure or utilized complex algorithms requiring extensive parameter tuning, this study targets RC columns and strictly enforces discrete design variables (rounded to 10 mm increments) to ensure constructability. By comparing these modern algorithms against strict ACI 440.2R-17 safety constraints, this paper aims to provide a robust, engineer-friendly framework that balances mathematical optimality with practical execution. The central hypothesis is that these parameter-light metaheuristic algorithms can converge to globally optimal solutions more efficiently than traditional methods, effectively establishing a streamlined, automated framework for sustainable and economical CFRP retrofitting.

2. Methodology

The algorithms used in this research to optimize the design of CFRP in columns against shear forces are Jaya, TLBO and FPA.

2.1. Jaya Algorithm

The Jaya algorithm is a population-based metaheuristic optimization method proposed by Rao. The word "Jaya" means "victory" in Sanskrit, and the algorithm's goal is to move away from the worst solution while approaching the best solution. In this respect, the Jaya algorithm combines the "survival of the fittest" principle of evolutionary algorithms with the global optimality search of swarm intelligence. The Jaya algorithm is single-phase and has no algorithm-specific control parameters. The user only specifies the population size and stopping criteria, making its implementation simple and user-friendly (Rao 2016).

Metaheuristic algorithms focus on optimizing the objective functions of engineering problems by modeling processes and behaviors in nature. Jaya also adopts the concept of victory and defeat in nature: in each iteration, existing solutions are labeled as best (optimal) and worst (pessimum) solutions; then, all candidate solutions are randomly adjusted by two coefficients to get closer to the best solution and further away from the worst solution. Thus, Jaya attempts to achieve a balance between exploration and exploitation in a parameter-free manner (Niğdeli et al. 2023).

In each iteration, all design variables of each individual (candidate solution) are calculated as shown in Eq. (1):

$$X_{i,j}^{t+1} = X_{i,j}^{t} + r1\left(X_i^{*} - \left|X_{i,j}^{t}\right|\right) - r2\left(X_i^{w} - \left|X_{i,j}^{t}\right|\right)$$
$$i = 1,2,..,n; j = 1,2,..,p; t = 1,2,..,t_{\max} \quad (1)$$

Here, $X^{t}_{i,j}$ represents the value of the i-th design variable of the j-th solution at the t-th iteration. X^{*}_{i} and X^{w}_{i} are the i-th variable values of the current best and worst individual, respectively. $r1$ and $r2$ are two randomly chosen numbers in the range [0,1], providing the stochastic property of the algorithm.

The main steps of the algorithm can be summarized as follows:

1. Initial Population: P random candidate solutions (individuals) are generated within the design range. Each individual is a vector of n design variables. Initial solutions are typically selected as shown in Eq. (2).

$$X_i^{j} = X_{i\min} + \text{rand}\,(1)(X_{i\text{mix}} - X_{i\min})$$
$$i = 1,2,\ldots.,n; j = 1,2,\ldots p \quad (2)$$

2. Objective Function Calculation: The objective function value for each individual is calculated. Any restrictions are disciplined using a penalty method. The smallest (cost-minimizing) or largest (performance-optimizing) individuals are identified.
3. Best and Worst Solutions: The best (closest to the global optimum) and worst (worst performing) solutions among all individuals in the population are determined.
4. Individual Updating: Each individual's design variable is updated using the equation above. This way, individuals are drawn toward the best solution and away from the worst. If variables in the updated solution fall outside the bounds, they are included in the range by horizontalization or boundary correction.
5. Creating a New Population: A new population is created with updated solutions. If necessary, the costs of new and old individuals are compared, and better solutions are carried over to the next iteration.
6. Stopping Criterion: Steps 2-5 are repeated until the desired number of iterations or the convergence criterion is reached. The best solution is then recorded.

These steps constitute the core of the Jaya algorithm. In each iteration, only the current best and worst solutions are considered; since there are no additional control parameters, the algorithm is structurally simple and parameter-free (da Silva et al. 2022; Duysak et al., 2024; Niğdeli et al., 2023).

2.2. Teaching-Learning Based Optimization Algorithm (TLBO)

Teaching-Learning-Based Optimization (TLBO) is a metaheuristic optimization algorithm proposed by Rao et al. (2011). Similar to other algorithms inspired by natural processes (such as GA, PSO, and FPA), TLBO performs the search by simulating the teaching–learning process within a classroom. The knowledge of students (solutions) is enhanced by the teacher (the best solution) and further updated through interactions (knowledge sharing) among students. The algorithm employs a classroom population, where each individual represents a student, and the total performance obtained from the student's "subjects" (design variables) is associated with that student's grade (fitness, cost, etc.).

Solution generation occurs in two consecutive stages: In the Teacher Stage, the "teacher" (the best solution in the population) improves the population mean towards the optimum; in the Student Stage, the "students" (the solution vectors) improve their performance through pairwise interactions. Both stages iteratively improve the population until the stopping criterion is met. In the Teacher Stage of the TLBO algorithm, new solution vectors are generated by the following equation (see Eq. (3)):

$$X_{\text{new}} = X_{\text{old}} + \text{rand}(1) \times (X_{\text{teacher}} - TF \times X_{\text{mean}}) \quad (3)$$

Here:
X_{new}: Newly generated solution vector,
X_{old}: Current solution vector,
rand(1): Uniform random number in the range [0,1],
X_{teacher}: Best solution vector in the population,
X_{mean}: Arithmetic mean of all current solution vectors,
TF: Teaching Factor determines the teacher's influence on the classroom.

The teaching factor TF can take a randomly chosen value of 1 or 2 using the following relationship (see Eq. (4)):

$$TF = \text{round}(1 + \text{rand}) \rightarrow \{1,2\} \quad (4)$$

This mechanism allows the teacher to try to raise the average knowledge level of the class relative to his or her own performance, thereby guiding the population towards better solutions.

In the Student Phase, new vectors are created based on two different solutions, X_i and X_j, randomly selected from the population. In this phase, new solution vectors

are generated using Eq. (5) by examining the objective functions ($f(X_i)$ and $f(X_j)$) of the existing solutions.

$$X_{\text{new}} = \begin{cases} X_{\text{current}} + \text{rand}(0,1) \times (X_i - X_j) \text{ if } f(X_i) > f(X_j) \\ X_{\text{current}} + \text{rand}(0,1) \times (X_j - X_i) \text{ if } f(X_i) < f(X_j) \end{cases} \quad (5)$$

A number of new solution vectors (pn) reflecting the initial population size are generated. Each candidate vector is recorded in the new solution matrix, and its objective function value is calculated. Each vector in this matrix is then compared with its counterpart in the existing solution matrix; if the new vector provides a superior objective function value, it replaces the existing vector. This generate–evaluate–replace cycle is repeated until a predefined stopping criterion is met (Dede and Ayvaz 2013; Camp and Farshchin 2014).

2.3. Flower Pollination Algorithm (FPA)

The Flower Pollination Algorithm (FPA), developed by Yang (2012), is a powerful optimization method inspired by the pollination processes that occur in plants. The algorithm mathematically models biotic (by living organisms) and abiotic (by environmental factors such as wind and water) pollination mechanisms and adapts these biological processes to optimize problem solving.

The algorithm's search mechanism is based on two main components: global pollination and local pollination. At each iteration, candidate solutions in the population are updated according to these two pollination strategies. Global pollination represents long-distance, random search capacity, while local pollination simulates the search for detailed solutions in a narrower search space. Thanks to this hybrid structure based on biological principles, FPA demonstrates balanced performance in both rapid convergence and preserving solution diversity.

FPA models the flower pollination process based on four fundamental rules (Abdel-Basset and Shawky 2019; Saber and Elhenawy 2021; Yang 2012):

1. Biotic and cross-pollination represent global pollination, and pollen is transported by Lévy flights.
2. Abiotic and self-pollination represent local pollination.
3. Floral constancy simulates the affinity of pollinators for specific flower types.
4. Global and local pollination are controlled by a crossover probability $p \in [0,1]$.

Based on these rules, global pollination is mathematically formulated as shown in Eq. (6):

$$X_{i,\text{new}} = X_{i,j} + L \times (X_{i,g\ \text{best}} - X_{i,j}) \quad (6)$$

Here:
$X_{i,\text{new}}$: The new value of the design variable (solution vector).
$X_{i,j}$: The initial matrix value of the j-th flower of the i-th design variable.
$X_{i,g\ \text{best}}$: The best solution in the population.
L: Represents the random step size generated from the Lévy distribution and is calculated as shown in Eq. (7):

$$L = \left(\frac{1}{2\pi}\right) \times (\text{rand}()^{-1.5}) \times e^{\left(\frac{1}{2\times\text{rand}}\right)} \quad (7)$$

Lévy flight allows the search space to be scanned in large steps, thus preventing the algorithm from getting stuck in local optima.

Subsequently, local pollination is expressed in Eq. (8) as:

$$X_{i,\text{new}} = X_{i,j} + \text{rand}() \times (X_{i,m} - X_{i,k}) \quad (8)$$

Here:
$X_{i,m}$, $X_{i,k}$: Different solutions from the same population.
rand: A random number between [0,1].

This mechanism allows exploring the local search space and improving existing solutions (Pavlyukevich 2007).

The choice between global and local pollination is controlled by the transition probability sp. This transition probability, defined in Rule 4, ensures a dynamic transition between the two stages.

3. Numerical Example

In this study, the optimal design of CFRP wrapping was carried out to enhance the shear capacity of reinforced concrete (RC) columns. The optimization procedure was conducted in compliance with ACI 440.2R-2017 and ACI 318-05 provisions. The objective function was defined as the minimization of CFRP volume required for a 1 m-long column segment.

The configuration of the CFRP system—characterized by the strip width W_f (mm), strip spacing S_f (mm), and total wrap thickness ($t_f \times n$) (mm)—is illustrated schematically in Fig. 1. These parameters constitute the principal design variables in the optimization process.

The optimization was performed using three metaheuristic algorithms: JAYA, Teaching–Learning-Based Optimization (TLBO), and Flower Pollination Algorithm (FPA). The analysis was repeated for various additional shear demand levels of 100 kN, 200 kN, 300 kN, 400 kN, and 500 kN, representing 20%, 40%, 60%, 80%, and 100% increases in the column's shear capacity, respectively.

The optimization problem targets the minimization of material consumption, quantified as the total volume of CFRP applied over a unit length (L = 1000 mm) of the column. The objective function, $F(X)$, is strictly defined by the column's geometric perimeter and the four optimization variables contained in the design vector $X = \{n, W_f, S_f, t_f\}$. These variables correspond to the number of layers, strip width, center-to-center spacing, and ply thickness, respectively. Accordingly, the objective function is explicitly formulated in Eq. (9):

$$F(X) = V_{\text{CFRP}} = \frac{n \times W_f \times t_f \times 2000 \times (b+h)}{s_f} \quad (9)$$

where b and h denote the cross-sectional dimensions of the RC column in mm. This formulation calculates the total volume of the transverse CFRP strips wrapping around the column perimeter within a one-meter height. By minimizing V_{CFRP}, the algorithm identifies the most cost-effective geometric configuration that strictly satisfies all strength and strain requirements specified in ACI 440.2R-17.

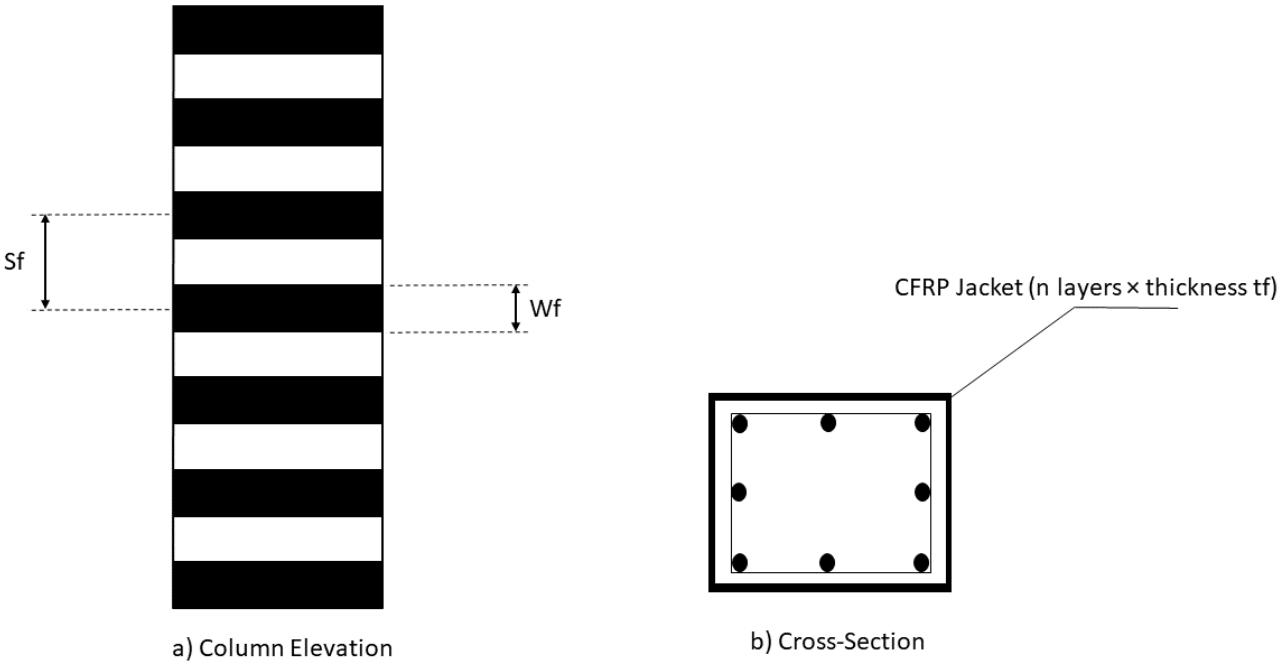

Fig. 1. Schematic definition of the optimization design variables.

All design variables are constrained within practical limits to ensure feasible CFRP configurations, as defined by Eqs. (10–13).

$$1 \leq n \leq 3 \tag{10}$$

$$0.2 \leq t_f \leq 2 \tag{11}$$

$$50 \leq W_f \leq 150 \tag{12}$$

$$10 \leq S_f \leq fix\left(\frac{\frac{df}{4}}{10}\right) \times 10 = 130 \tag{13}$$

To ensure practical constructability and address the discrete nature of the design parameters, specific handling mechanisms were implemented in the algorithms. The number of layers (n) is treated strictly as an integer; thus, continuous values generated during optimization are rounded to the nearest integer within the range [1,3]. Similarly, the strip width (W_f) and spacing (S_f) are constrained to be multiples of 10 mm to facilitate on-site application. Consequently, the algorithm rounds these variables to the nearest multiple of 10 within their respective bounds before evaluating the objective function.

The constraints of the optimization problem are as follows: Eqs. (14–16):

$$g_1: 0.75 \times \varepsilon_{fu} - 0.004 \geq 0 \tag{14}$$

$$g_2 = \frac{2 \times t_f \times n \times W_f \times E_f \times \varepsilon_{fe} \times d_f}{S_f} - V_{\text{freq}} > 0 \tag{15}$$

$$g_3 = \frac{2 \times t_f \times n \times W_f \times F_{fe} \times d_f}{S_f} + V_s - (2 \times (1 + 72.5 \times \frac{N_u}{A_g}) \times \sqrt{F_c} \times b \times d_f) < 0 \tag{16}$$

These constraints strictly enforce the safety provisions of ACI 440.2R-17:

- Strain Limitation (g_1): Eq. (14) ensures that the effective strain in the CFRP laminate does not exceed the maximum allowable limit of 0.004 (or 0.75 × ε_{fu}), preventing premature debonding failure before the concrete reaches its useful compressive strain.
- Shear Capacity Requirement (g_2): Eq. (15) guarantees that the shear contribution provided by the optimized CFRP configuration (V_f), when added to the existing steel and concrete resistance, is sufficient to meet the target shear demand (V_{freq}).
- Maximum Strengthening Limit (g_3): Eq. (16) serves as a brittle failure prevention check. It limits the total shear reinforcement (V_s + V_f) to prevent the concrete struts from crushing before the reinforcement yields, ensuring a ductile failure mode.

The key design parameters and their numerical values used in the optimization are listed in Table 1.

The overall flow of the optimization process, illustrating the sequence of algorithmic steps from initialization to final design selection, is presented in Fig. 2.

4. Results and Discussion

The optimization algorithms were implemented in MATLAB to evaluate their performance in determining the most efficient CFRP strengthening configurations. For each algorithm, a randomly initialized population was generated, followed by an iterative optimization process. To strictly enforce the safety limits defined in ACI 440.2R-17 (Eqs. 14–16), a static penalty method was employed to handle constraints. Unlike methods that add a soft penalty term, this approach assigns a prohibitively high constant value to any infeasible solution. The penalized objective function $F(X)$ is defined by Eq. (17):

$$F(X) = \begin{cases} V_{\text{CFRP}}(X) & \text{if } g_i(X) \text{ is satisfied; } i = 1,2,3 \\ 10^6 & \text{otherwise} \end{cases} \quad (17)$$

where $V_{\text{CFRP}}(X)$ is the calculated volume. By assigning a high value (10^6) to designs violating constraints, the algorithms are forced to discard non-compliant solutions and converge effectively toward the feasible region.

Table 1. Design constants.

Parameters	Description	Values
$b \times h$	Column dimensions (mm)	600×600
F_c	Concrete compressive strength (MPa)	20
d_f	Effective depth (mm)	540
E_f	CFRP modulus of elasticity (MPa)	170000
φ	Strength reduction factor (ACI 318-05)	0.85
C_E	Environmental reduction factor (indoor)	0.95
Ψ_f	Full confinement reduction factor	0.95
ε_{fu}'	CFRP rupture strain (mm/mm)	0.018
ε_{fu}	CFRP design strain (mm/mm)	$C_E \times \varepsilon_{fu}' = 0.0171$
ε_{fe}	Effective CFRP strain (mm/mm)	$\min(0.004; 0.75 \times \varepsilon_{fu}) \approx 0.004$
F_{fe}	Effective CFRP tensile strength (MPa)	$\varepsilon_{fe} \times E_f = 680$
V_s	Stirrup shear capacity (kN)	500
V_{ek}	Additional shear demand (kN)	100, 200, 300, 400, 500
V_{freq}	Required CFRP shear contribution (kN)	$V_{ek} / (\varphi \times \Psi_f)$
N_u	Normal force (kN)	200
A_g	Gross concrete cross-sectional area (mm^2)	2920

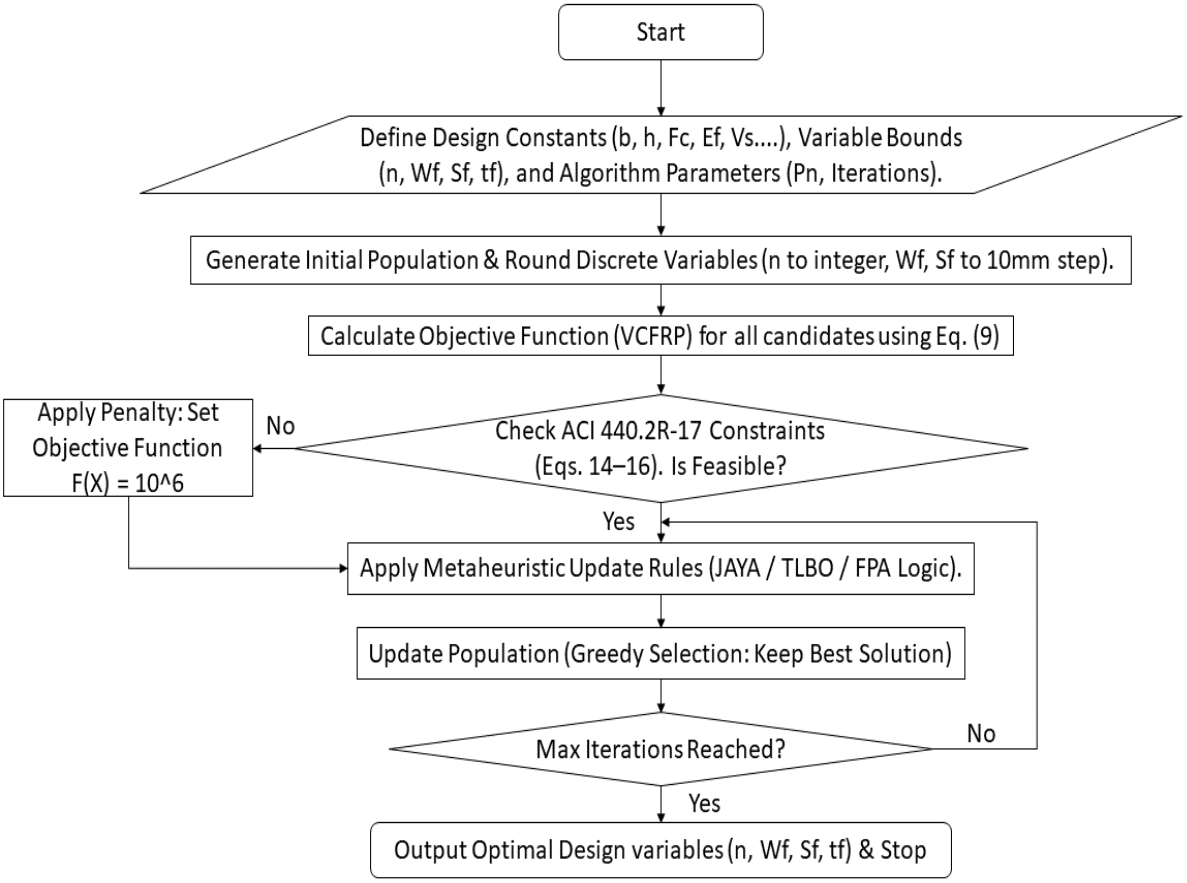

Fig. 2. Flowchart of the optimization framework and constraint handling.

To ensure statistical consistency, each algorithm was executed independently 30 times. The computational parameters were defined as follows: the population size varied between 20 and 25, and the number of iterations ranged from 100 to 500. These values were determined through a preliminary sensitivity analysis, which indicated that they provide an optimal balance between solution stability (minimizing standard deviation) and computational efficiency. For the FPA algorithm, the switching probability was set to sp=0.5.

In each scenario, the best CFRP volume (V_{best}), mean volume (V_{mean}), standard deviation, population size, number of iterations, and average iteration time were recorded to enable a comparative assessment of algorithmic performance. The top three distinct optimal configurations (yielding the lowest CFRP volumes) were extracted for each algorithm and shear demand level from the 30 independent runs to demonstrate design flexibility. The results are presented in Tables 2–6.

Table 2. CFRP strengthening optimization under 100 kN additional shear force (20% increase): Comparison of JAYA–TLBO–FPA.

Algorithm	Solutions (n, W_f, Sf, t_f)	V_{best} (mm^3/m)	V_{mean} (mm^3/m)	Standard deviation	Number of iterations	Population size	Iteration time (second)
JAYA	(1; 110; 130; 0.20) (1; 50; 120; 0.41) (1; 60; 130; 0.37)	404,729.64	405,685.62	1,239.07	100	20	0.014
TLBO	(2; 50; 120; 0.20) (1; 100; 120; 0.20) (1; 50; 60; 0.20)	404,705.20	404,835.98	298.08	100	20	0.109
FPA	(1; 60; 70; 0.20) (1; 100; 130; 0.22) (1; 110; 130; 0.20)	404,702.65	405,231.45	1,283.05	100	20	0.065

Table 3. CFRP strengthening optimization under 200 kN additional shear force (40% increase): Comparison of JAYA–TLBO–FPA.

Algorithm	Solutions (n, W_f, Sf, t_f)	V_{best} (mm^3/m)	V_{mean} (mm^3/m)	Standard deviation	Number of iterations	Population size	Iteration time (second)
JAYA	(2, 80, 100, 0.21) (2, 110, 130, 0.20) (1, 70, 70, 0.34)	809,408.38	810,061.75	952.92	100	25	0.014
TLBO	(1, 50, 110, 0.74) (1, 60, 70, 0.39) (1, 50, 120, 0.81)	809,412.23	809,515.50	130.41	100	25	0.127
FPA	(1, 80, 130, 0.55) (1, 50, 50, 0.34) (3, 50, 130, 0.29)	809,405.29	809,510.37	529.61	100	25	0.066

Table 4. CFRP strengthening optimization under 300 kN additional shear force (60% increase): Comparison of JAYA–TLBO–FPA.

Algorithm	Solutions (n, W_f, Sf, t_f)	V_{best} (mm^3/m)	V_{mean} (mm^3/m)	Standard deviation	Number of iterations	Population size	Iteration time (second)
JAYA	(1, 140, 100, 0.36) (2, 50, 80, 0.40) (1, 100, 40, 0.20)	1,214,120.70	1,214,881.24	1156.67	150	20	0.016
TLBO	(1, 50, 30, 0.30) (1, 60, 100, 0.84) (2, 50, 110, 0.56)	1,214,110.46	1,214,214.94	162.72	150	20	0.311
FPA	(3, 70, 110, 0.26) (2, 60, 100, 0.42) (3, 50, 130, 0.44)	1,214,107.93	1,214,108.91	2.92	150	20	0.068

Table 5. CFRP strengthening optimization under 400 kN additional shear force (80% increase): Comparison of JAYA–TLBO–FPA.

Algorithm	Solutions (n, W_f, Sf, t_f)	V_{best} (mm^3/m)	V_{mean} (mm^3/m)	Standard deviation	Number of iterations	Population size	Iteration time (second)
JAYA	(3, 90, 80, 0.20) (1, 50, 90, 1.21) (1, 130, 130, 0.67)	1,618,814.38	1,619,075.19	390.05	250	20	0.020
TLBO	(1, 50, 110, 1.48) (3, 50, 130, 0.58) (1, 130, 70, 0.36)	1,618,810.62	1,618,906.45	122.31	250	20	0.158
FPA	(3, 60, 130, 0.49) (2, 140, 120, 0.29) (1, 50, 130, 1.75)	1,618,810.58	1,618,875.45	251.55	250	20	0.079

Table 6. CFRP strengthening optimization under 500 kN additional shear force (100% increase): Comparison of JAYA–TLBO–FPA.

Algorithm	Solutions (n, W_f, Sf, t_f)	V_{best} (mm^3/m)	V_{mean} (mm^3/m)	Standard deviation	Number of iterations	Population size	Iteration time (second)
JAYA	(1, 60, 120, 1.69) (1, 120, 50, 0.35) (1, 90, 110, 1.03)	2,023,513.26	2,023,697.19	223.61	500	25	0.029
TLBO	(1, 60, 60, 0.84) (1, 50, 80, 1.35) (2, 90, 120, 0.56)	2,023,513.29	2,023,545.47	46.63	500	25	0.301
FPA	(1, 50, 110, 1.85) (1, 90, 90, 0.84) (2, 70, 80, 0.48)	2,023,513.22	2,023,513.24	0.08	500	25	0.102

The reliability of the optimization results was verified by performing a check on the optimal solution obtained for the first load case (100 kN additional shear). The configuration yielded by the FPA algorithm was subjected to rigorous manual verification, strictly adhering to the design procedures and illustrative examples provided in ACI 440.2R-17. This manual check confirmed that the calculated shear contribution (V_f) is identical to the algorithm's output. Furthermore, it verified that the proposed configuration fully satisfies all relevant code constraints, including strain limits, CFRP shear contribution restrictions, and total shear capacity limits. This validation confirms the accuracy of the implemented computational framework.

The results presented in Tables 2–6 reveal distinct behavioral characteristics of the applied metaheuristics. Although all three algorithms successfully satisfied the ACI 440.2R-17 constraints, FPA consistently achieved the marginally lowest CFRP volumes. This superior convergence capability can be attributed to its Lévy flight mechanism, which allows the algorithm to perform long-distance jumps across the search space. This feature is particularly effective in avoiding local minima in the non-linear landscape of shear design, enabling FPA to locate the global optimum more frequently than JAYA or TLBO.

On the other hand, TLBO demonstrated the highest stability, evidenced by the lowest standard deviation across the 30 independent runs. This robustness is likely due to its 'Teacher Phase,' which consistently pulls the population mean towards the best solution, reducing the variance of the final outputs. Conversely, JAYA proved to be the most computationally efficient algorithm, achieving the shortest average iteration time. This speed advantage stems from its algorithmic simplicity; unlike TLBO, which requires two phases per iteration, JAYA utilizes a straightforward single-phase update mechanism without complex specific control parameters, making it highly suitable for rapid design iterations.

Regarding the magnitude of savings, while the numerical differences in CFRP volume between the algorithms may appear negligible for a single meter of column, their practical significance scales substantially. In large-scale retrofitting projects involving hundreds of structural members, these cumulative material savings translate into meaningful cost reductions and lower environmental impact, justifying the computational effort to find the absolute global minimum.

Beyond the numerical efficiency, these results carry significant practical engineering implications. First, the minimization of CFRP volume directly translates to cost reduction, making the strengthening projects more economically viable. Second, by constraining the design variables (strip width and spacing) to discrete 10 mm increments, the proposed solutions are standardized and 'site-ready,' reducing the risk of labor errors during in-

stallation. Ultimately, the presentation of multiple distinct solution sets for each load case provides engineers with crucial construction flexibility, allowing them to adapt to material inventory shortages without delaying the construction schedule.

5. Conclusions

This study presented a robust computational framework for the optimal design of Carbon Fiber Reinforced Polymer (CFRP) wrapping to enhance the shear capacity of RC columns. By employing three distinct metaheuristic algorithms—Jaya, Teaching–Learning-Based Optimization (TLBO), and Flower Pollination Algorithm (FPA)—the research successfully minimized material consumption while strictly adhering to the safety provisions of ACI 440.2R-17 and ACI 318-05. The investigation covered a wide range of shear demands (100–500 kN), demonstrating that automated optimization can yield feasible, code-compliant solutions that are significantly more economical than traditional manual designs.

A comparative performance analysis revealed distinct advantages for each algorithm. The FPA consistently achieved the absolute minimum CFRP volumes, attributed to its Lévy-flight mechanism, which effectively avoids local minima. Meanwhile, TLBO demonstrated superior stability with the lowest standard deviation across independent runs, and JAYA proved to be the most computationally efficient, offering the fastest convergence speeds due to its parameter-free structure. Crucially, the reliability of these computational results was validated through a rigorous manual verification of the optimal solution for the initial load case, confirming exact alignment with standard code procedures.

Beyond numerical efficiency, this study bridges the gap between theoretical optimization and on-site application. Unlike previous works that relied on continuous variables, this research enforced discrete design variables (e.g., rounding strip widths and spacing to 10 mm increments). This approach ensures that the proposed configurations are "site-ready," reducing the likelihood of installation errors and enhancing constructability. Consequently, the proposed framework offers engineers a practical tool to reduce material costs and environmental impact in large-scale retrofitting projects. Future research should expand this methodology to include multi-objective optimization, considering factors such as total application time and labor costs, as well as applying these algorithms to other structural elements like T-beams or circular columns.

Acknowledgements

None declared.

Funding

The authors received no financial support for the research, authorship, and/or publication of this manuscript.

Conflict of Interest

The authors declare no potential conflicts of interest with respect to the research, authorship, and/or publication of this manuscript.

Data Availability

The datasets generated and/or analyzed during the current study are not publicly available but are available from the corresponding author upon reasonable request.

AI Assistance

No AI-based tools were used in the preparation of this manuscript.

Author Contributions

All authors made substantial contributions to the conception and design of the study, acquisition of data, analysis and interpretation of data; drafted or critically revised the manuscript for important intellectual content; and approved the final version to be published.

REFERENCES

Abdel-Basset M, Shawky LA (2019). Flower pollination algorithm: a comprehensive review. *Artificial Intelligence Review*, 52(4), 2533-2557.

ACI 318-05 (2005). Building Code Requirements for Structural Concrete (ACI 318-05) and Commentary (ACI 318R-05). American Concrete Institute, Farmington Hills, MI, USA.

ACI 440.2R-17 (2017). Guide for the Design and Construction of Externally Bonded FRP Systems for Strengthening Concrete Structures. American Concrete Institute, Farmington Hills, MI, USA.

Aydın Y, Ahadian F, Bekdaş G, Nigdeli S (2024). Prediction of optimum design of welded beam design via machine learning. *Challenge Journal of Structural Mechanics*, 10(3), 86-94.

Camp CV, Farshchin M (2014). Design of space trusses using modified teaching–learning based optimization. *Engineering Structures*, 62–63, 87-97.

Çoşut M, Bekdaş G, Nigdeli S (2023). Optimization of reinforced concrete frame structures and matrix displacement method. *Challenge Journal of Concrete Research Letters*, 14(1), 10-17.

da Silva LS, Lúcio YL, Coelho LD, Mariani VC, Rao RV (2022). A comprehensive review on Jaya optimization algorithm. *Artificial Intelligence Review*, 56, 4329-4361.

Dede T, Ayvaz Y (2013). Structural optimization with teaching-learning-based optimization algorithm. *Structural Engineering and Mechanics*, 47(4), 495-511.

Dugguh LN (2015). Multi-objective optimization of carbon fibre reinforced plastic (CFRP) circular hollow section using genetic algorithm for engineering structures. *International Refereed Journal of Engineering and Science*, 4(12), 24–28.

Duysak Y, Nigdeli SM, Bekdaş G (2024). Optimum design of reinforced concrete beam sections with JAYA algorithm. *Challenge Journal of Concrete Research Letters*, 15(4), 134-141.

Gkournelos PD, Triantafillou TC, Bournas DA (2021). Seismic upgrading of existing reinforced concrete buildings: A state-of-the-art review. *Engineering Structures*, 240, 112273.

Kayabekir AE, Sayın B, Nigdeli SM, Bekdaş G (2018). Jaya algorithm based optimum carbon fiber reinforced polymer design for reinforced concrete beams. *AIP Conference Proceedings*, 1978(1), 260006.

Kayabekir AE (2018). Yapı Mühendisliğinde Metasezgisel Algoritmalar ile Optimizasyon Uygulamaları [Optimization Applications with Metaheuristic Algorithms in Structural Engineering]. *M.Sc. thesis*, İstanbul University-Cerrahpaşa, İstanbul, Türkiye. (in Turkish)

Nigdeli SM, Bekdaş G, Kayabekir AE (2023). Metasezgisel yöntemlerle betonarme yapı elemanlarının optimizasyonu [Optimization of reinforced concrete structural elements with metaheuristic methods]. *İstanbul University-Cerrahpaşa Yayınları*, İstanbul, Türkiye. (in Turkish)

Pavlyukevich I (2007). Lévy flights, non-local search and simulated annealing. *Journal of Computational Physics*, 227(1), 183-190.

Rahman MM, Jumaat MZ, Hosen MA (2012). Genetic algorithm for material cost minimization of external strengthening system with fiber

reinforced polymer. *Advanced Materials Research*, 468–471, 1817–1822.

Rao RV, Savsani VJ, Vakharia DP (2011). Teaching–learning-based optimization: a novel method for constrained mechanical design optimization problems. *Computer-Aided Design*, 43(3), 303-315.

Rao RV (2016). Jaya: A simple and new optimization algorithm for solving constrained and unconstrained optimization problems. *International Journal of Industrial Engineering: Theory, Applications and Practice*, 7, 19-34.

Saber S, Elhenawy I (2021). A survey on flower pollination algorithm. *Journal of Intelligent Systems and Internet of Things*, 2(1), 5–11.

Tomar V, Bansal M, Singh P (2023). Metaheuristic algorithms for optimization: A brief review. *Engineering Proceedings*, 59(1), 238.

Ulusoy S, Kayabekir AE, Bekdaş G, Nigdeli SM (2020). Metaheuristic algorithms in optimum design of reinforced concrete beam by investigating strength of concrete. *Challenge Journal of Concrete Research Letters*, 11(2), 26-30.

Xie J, Liu XM, Zhao T (2005). Shear capacity of reinforced concrete columns strengthened with CFRP sheet. *Journal of Zhejiang University - Science A: Applied Physics & Engineering*, 6(8), 853-858.

Yang XS (2012). Flower pollination algorithm for global optimization. In: Durand-Lose J, Jonoska N, editors. Unconventional computation and natural computation. *Lecture Notes in Computer Science*, 7445. Springer, London, UK, 240-249.

Yun Y, Gen M, Erdene TN (2023). Applying GA-PSO-TLBO approach to engineering optimization problems. *Mathematical Biosciences and Engineering*, 20(1), 552–571.

Yücel M (2025). Comparison of flower pollination algorithm and particle swarm optimization for structural weight minimization of RC beams with carbon fiber reinforced polymer (CFRP). *Afyon Kocatepe University Journal of Sciences and Engineering*, 25(2), 381–387.